The $ZZ \to 4\ell$ process and anomalous triple gauge couplings with ATLAS at the LHC

Jonatan Hans Niclas Rostén

January 9, 2018

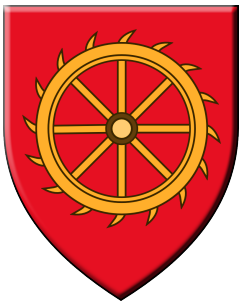

ST CATHARINE'S COLLEGE
UNIVERSITY OF CAMBRIDGE

This dissertation is submitted for the degree of Doctor of Philosophy

The $ZZ \to 4\ell$ process and anomalous triple gauge couplings with ATLAS at the LHC

Jonatan Hans Niclas Rostén

Abstract

This thesis is a presentation of an analysis of the $ZZ \to 4\ell$ ($\ell = e, \mu$) process in proton-proton collisions with centre-of-mass energy $\sqrt{s} = 13\,\text{TeV}$ at the LHC during 2015 and 2016 (a total integrated luminosity of 36.1 fb^{-1}), using the ATLAS detector. Candidate $ZZ \to 4\ell$ events are selected in the three decay channels, $4e$, $2e2\mu$ and 4μ. The cross section of the $ZZ \to 4\ell$ process is measured in four fiducial regions closely matching the detector acceptance: one for each decay channel ($4e$, $2e2\mu$ and 4μ) and one for the combination of all decay channels. The total cross section of $pp \to ZZ$ is measured in a phase-space in which both Z bosons have a mass m_Z in the range $66\,\text{GeV} < m_Z < 116\,\text{GeV}$ to be 16.5 $\pm$0.5 (stat.) $\pm$0.4 (syst.) $\pm$0.5 (lumi.) pb which is consistent with a next-to-next-to-leading-order prediction of $16.9^{+0.6}_{-0.5}$ pb. Observed event yields in four bins of transverse momentum are used to set 95 % CL_s limits on four neutral triple gauge couplings (f_i^V, $V = Z, \gamma$, $i = 4, 5$) which parameterise an effective ZZV vertex (assuming both Z bosons are on shell). The obtained limits are of the order of $|f_i^V| < 0.0017$.

Declaration

This dissertation is the result of my own work, except as specified in the text. It is not substantially the same as any that I have submitted, or, is being concurrently submitted for a degree or diploma or other qualification at the University of Cambridge or any other University or similar institution. I further state that no substantial part of my dissertation has already been submitted, or, is being concurrently submitted for any such degree, diploma or other qualification at the University of Cambridge or any other University or similar institution.
It does not exceed the prescribed word limit for the Physics and Chemistry Degree Committee of Cambridge University.

This thesis is dedicated to my father Hans Bertil Franzén, 1931-2015.

Acknowledgements

The submission of this thesis is one of the final steps in the works towards a Ph.D. and I would like to take this opportunity to acknowledge and thank those who have helped me through these years.

First, I would like to thank the Science and Technology Facilities Council for the three and a half years of financial support that has made this thesis and the work within it possible, including nine months spent at CERN in Geneva, Switzerland. I also thank Val Gibson, Andy Parker and the Cambridge High Energy Physics department as well as the ATLAS experiment for the opportunity to pursue a Ph.D. in such wonderful places as Cambridge and CERN.

I would also like to thank my supervisor Richard Batley and second supervisor Pat Ward for all the help and supervision, not least for rereading this thesis many times and coming with invaluable comments.

For the work on ZZ analyses, I would also like to thank Stefan Richter, Maurice Becker, Will Buttinger and Steven Kaneti for the help and guidance I needed to complete this thesis and the work in it.

These acknowledgements would be incomplete without mentioning my office mates throughout the years in Cambridge, in particular Thibaut Mueller, Thomas Gillam, T.J. Khoo and Benjamin Brunt for their respective combinations of helpful and distracting conversation, in as well as outwith the office.

The time in Cambridge has also been enhanced by extracurricular activities which I thank if nothing else my sustained sanity for. In particular, I would mention the Cambridge University Gilbert and Sullivan Society, the Impronauts and St. Catharine's college.

Finally, I want to thank my mother, Viveca Rostén, for the love and support I have enjoyed. She has been instrumental in every step of the road leading to where I am today.

Contents

List of Tables

List of Figures

Chapter 1

Introduction

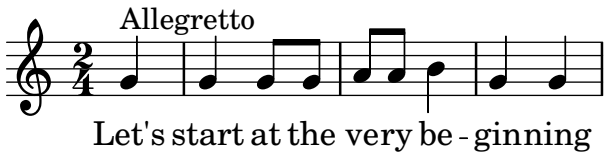

— Rodgers & Hammerstein, *1959*

This thesis details an analysis performed in 2016 and 2017 of the $pp \to ZZ \to 4\ell$ process with the ATLAS detector [1] at the Large Hadron Collider [2] in Geneva, Switzerland. The cross section for ZZ production is measured and limits are set on anomalous triple gauge couplings.

The Standard Model of particle physics (SM) [3, 4] is a mathematical description of our current understanding of the known fundamental forces (except gravity) and elementary particles. It has been very successful in describing the results of a large number of measurements and experiments, including the discovery of the Higgs boson in 2012 [5,6]. The SM describes three fundamental forces, the strong, weak and electromagnetic forces, as well as the combination of the weak and electromagnetic forces into one electroweak force. The SM includes twelve matter particles, which are fermions (and their anti-particles) and 13 force carrying particles, all of which can be seen in table 2.1.

Despite the success of the SM, certain fundamental questions have remained unanswered. These include the question of how gravity fits into the SM and why the fermion masses are distributed as they are. The SM also fails to convincingly explain a number of observations, like the masses of neutrinos [7] and dark matter (which is inferred from unexpected rotation curves of galaxies [8]).

There are specific problems with the electroweak region of the SM. One unknown aspect is why the weak force is stronger than gravity. In particular, this manifests in the Higgs boson mass (125 GeV [9]) being much smaller than the planck scale. This situation seems inconsistent with the idea of naturalness, which allows parameters to be very small only under certain conditions (when it the parameter being 0 would increase the symmetry of the system) [10].

Given these problems and others, one is forced to conclude that the SM does not explain everything. Other theories have been proposed to resolve such issues, ranging from models of extra space-time dimensions [11], quantum gravity [12] and supersymmetric theories [13]. However, none of these theories have achieved the experimental verification required to surpass the SM as the best available model of particle physics.

The Large Hadron Collider (LHC) is a particle collider, accelerating protons and colliding them at a centre-of-mass energy $\sqrt{s} = 13\,\text{TeV}$, producing, among other things, ZZ events. The Z bosons can decay into, among other things, two electrons or two muons, which can be detected by the ATLAS detector: a toroidal, multipurpose detector situated on the LHC. This gives rise to three channels, $e^-e^+e^-e^+$, $e^-e^+\mu^-\mu^+$ and $\mu^-\mu^+\mu^-\mu^+$, known hereafter as $4e$, $2e2\mu$ and 4μ, respectively.

Analysing these events can test the SM, both by measuring the cross section of the ZZ process (in four fiducial regions, closely matching the acceptance of the ATLAS detector, and one total phase space) and by looking for neutral triple gauge couplings (i.e. the coupling between neutral gauge bosons, Z bosons and photons). Neutral triple gauge couplings are not allowed in the SM, so observing them would be an observation of physics beyond the SM and open up an opportunity to improve or reject the SM. Four neutral triple gauge couplings, f_4^γ,f_5^γ,f_4^Z and f_5^Z are considered. All measurements of the coupling strengths to date have been consistent with the SM value of 0. Limits on these couplings have been set at around 10^{-3}.

Electron and muon identification and reconstruction efficiencies are high in ATLAS. The limiting factor in this analysis is the amount of collisions delivered by the LHC and recorded by the ATLAS detector.

The work presented in this thesis was performed during 2015 through 2017 as a part of the ATLAS SM ZZ analysis, including two papers [14, 15], the latter of which has been submitted to Physical Review D but has not yet been accepted at the time of writing. The author of this thesis contributed cross section extraction for those papers, as well as parts of the background estimates and analysis of the anomalous triple gauge couplings (and some minor work on the other parts of the analysis).

Chapter 2

The Standard Model and anomalous triple gauge couplings

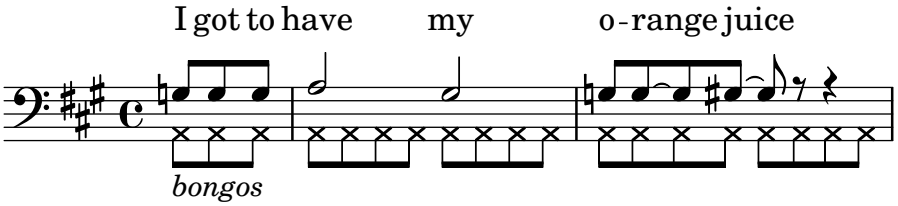

— Richard Feynman, *Orange juice*

The Standard Model is a quantum field theory which describes all known fundamental particles and forces (except gravity). This chapter describes the role of gauge bosons like the Z boson in the SM, including the Higgs mechanism which gives gauge bosons their mass.

2.1 The Standard Model

The SM is a quantum gauge field theory which describes all known fundamental particles and their interactions (except gravity). It has an $SU(3) \times SU(2)_L \times U(1)$ gauge group and 24 fermion fields. Of those, 18 are quarks (6 flavours, down, up, strange, charm, bottom and top, times three colours, red, green and blue) and six are leptons (three charged, electrons, muons and tauons, and three corresponding neutrinos).

Each fermion corresponds to a 4-component spin-$\frac{1}{2}$ field ψ which follows the Dirac equation given by the Lagrangian density [3, 4]

$$\mathcal{L}_D = \bar{\psi}(i\partial\!\!\!/ - m)\psi. \tag{2.1}$$

In order to maintain gauge invariance (which is required by the SM), twelve gauge fields are introduced by modification of the covariant derivative as follows

$$\partial^\mu \to D^\mu = \partial^\mu + ig_1 Y B^\mu + ig_2 \mathbf{T} \cdot \mathbf{W}^\mu + ig_3 \mathbf{X} \cdot \mathbf{G}^\mu \tag{2.2}$$

where Y is the *weak hypercharge* of the fermion involved, B is the gauge field of the $U(1)$ symmetry, $\mathbf{W}$ and $\mathbf{G}$ are the fields of the $SU(2)$ and $SU(3)$ symmetries, respectively (three for $SU(2)$, eight for $SU(3)$), $\mathbf{T}$ and $\mathbf{X}$ are the $SU(2)$ and $SU(3)$ group generators (commonly taken to be $\frac{1}{2}$ times the Pauli and Gell-Mann matrices, respectively [4]) and g_1, g_2 and g_3 are the coupling constants.

The gauge fields of $SU(3)$ correspond to the eight gluons. The electroweak gauge bosons (γ, Z and $W^\pm$) arise due to a mixing of $U(1)$ and $SU(2)$, and their respective fields are given by

$$A_\mu = \quad B_\mu \cos\theta_W + W^3_\mu \ \sin\theta_W \tag{2.3}$$

$$Z_\mu = -B_\mu \sin\theta_W + W^3_\mu \ \cos\theta_W \tag{2.4}$$

$$W^\pm_\mu = \quad \frac{1}{\sqrt{2}}(W^1_\mu \mp W^2_\mu) \tag{2.5}$$

(A being the photon field) where θ_W is the Weinberg angle, related to the g_i couplings as

$$\cos\theta_W = \frac{g_2}{\sqrt{g_1^2 + g_2^2}}, \quad \sin\theta_W = \frac{g_1}{\sqrt{g_1^2 + g_2^2}}. \tag{2.6}$$

The fundamental particles associated with these fields and some of their properties can

Particle type	Name (symbol)	Q/e	m
Quarks (×3 colours)	up (u)	$^2/_3$	$2.2^{+0.6}_{-0.4}$ MeV
	down (d)	$-^1/_3$	$4.7^{+0.5}_{-0.4}$ MeV
	charm (c)	$^2/_3$	1.27 ± 0.03 GeV
	strange (s)	$-^1/_3$	96^{+8}_{-4} MeV
	top (t)	$^2/_3$	173.2 ± 0.9 GeV
	bottom (b)	$-^1/_3$	$4.18^{+0.04}_{-0.03}$ GeV
Leptons	electron (e)	-1	0.51 MeV
	muon (μ)	-1	106 MeV
	tauon (τ)	-1	1.78 GeV
	e neutrino (ν_e)	0	< 2 eV
	μ neutrino (ν_μ)	0	< 0.19 MeV
	τ neutrino (ν_τ)	0	< 18.2 MeV
Bosons	photon (γ)	0	0
	Z boson (Z)	0	91.1876 ± 0.0023 GeV
	W boson ($W^\pm$)	± 1	80.385 ± 0.015 GeV
	gluon (g) × 8	0	0
	Higgs boson (H^0)	0	125.09 ± 0.24 GeV

Table 2.1: Fundamental particles of the SM with their charges Q (in units of the electron charge e) and masses m [9]. The uncertainties on the masses of the charged leptons have been omitted due to their being many orders of magnitude smaller than the precision in the table.

be seen in table 2.1.

The field W_i (where W_i is the ith gauge field of the group) transforms under the gauge operator U as

$$W_{i\mu} \to W'_{i\mu} = UW_{i\mu}U^\dagger + \frac{i}{g}(\partial_\mu U)U^\dagger. \tag{2.7}$$

In the SM Lagrangian, bosons of mass m_{Wi} are represented by a spin-one Proca equation:

$$\mathcal{L}_P = -\frac{F_i^{\mu\nu}F_{i\mu\nu}}{4} + \frac{m_{Wi}^2 W_{i\mu}W_i^\mu}{2} \tag{2.8}$$

where m_{Wi} is the mass of the particle associated with W_i and

$$F_i^{\mu\nu} = \partial^\mu W_i^\nu - \partial^\nu W_i^\mu - g\epsilon_{ijk}W_j^\mu W_k^\nu. \tag{2.9}$$

However, the SM demands gauge invariance of the Lagrangian under the transformation in eq. (2.7). The last term of eq. (2.8) is not gauge invariant (unless $m_{Wi} = 0$). This

means massive gauge bosons like W and Z can only be included in the SM via the inclusion of the *Higgs mechanism*.

2.1.1 Higgs mechanism

To include gauge boson and fermion masses in the SM, an additional $SU(2)$ doublet of complex scalar fields

$$\phi = \begin{pmatrix} \phi_1 \\ \phi_2 \end{pmatrix} \tag{2.10}$$

is introduced to the SM Lagrangian density, using the gauge invariant expression

$$\mathcal{L}_H = (D_\mu \phi)^\dagger (D^\mu \phi) + \mu^2 \phi^\dagger \phi - \lambda (\phi^\dagger \phi)^2. \tag{2.11}$$

The Lagrangian has a degenerate set of minima at which $\phi^\dagger \phi = \mu^2/2\lambda$. Without loss of generality, the case

$$\phi_{min} = \begin{pmatrix} 0 \\ v/\sqrt{2} \end{pmatrix} \tag{2.12}$$

can be arbitrarily chosen, where v is the vacuum expectation value, $v = \sqrt{\mu^2/\lambda}$ and then expanded around that point as follows

$$\phi(x) = \begin{pmatrix} 0 \\ \frac{v+h(x)}{\sqrt{2}} \end{pmatrix}. \tag{2.13}$$

When this expansion is used in eq. (2.11), the $\phi^\dagger \phi$ terms give rise to non-zero mass terms of the form seen in eq. (2.8). Choosing the weak hypercharge of the field ϕ to be $1/2$, the photon remains massless while the Z and W boson masses become $m_Z = v g_2 / 2\cos(\theta_W)$ and $m_W = v g_2/2$, respectively. The quantum of the scalar field $h(x)$ introduced in the expansion is the Higgs boson, which gains a mass $m_H = \sqrt{2\lambda v^2}$.

2.2 ZZ production and decay in the Large Hadron Collider

The Large Hadron Collider (LHC) (described in more detail in chapter 3) collides protons with a centre-of-mass energy of 13 TeV. One of the possible products of such collisions is ZZ events. Measuring the production of ZZ events in the LHC provides

a test of the SM. There are also many other analyses within the ATLAS collaboration that rely on final states with many leptons and to which ZZ production is a background process. The analysis in this thesis provides a ZZ production cross section that can be used to estimate backgrounds in such analyses.

The cross section extraction in chapter 7 considers as *signal* all processes in which exactly two Z bosons are produced in a pp collision and decay directly into electrons or muons. The Feynman diagrams for signal ZZ production at the LHC that are most important for this thesis can be seen in fig. 2.1. The Higgs contribution ($gg \to H^{0*} \to ZZ$) is also included in the signal. Previous measurements of the signal processes can be found in section 2.5 and theoretical predictions can be found in section 2.4. The signal does not include Double Parton Interactions (DPI, two Z bosons, each from a different parton parton interaction), which were found to be negligible [15].

In these processes, both off- and on-shell Z bosons can be produced. The analysis in this thesis considers Z bosons in the mass window $66\,\text{GeV} < m < 116\,\text{GeV}$, roughly corresponding to the mass window $m = m_Z \pm 10\Gamma_Z$ where m_Z is the Z pole mass and Γ_Z is the Z width (see table 2.2).

Z bosons are known to decay directly to neutrinos, charged leptons and quarks. The branching ratio of Z to hadrons is around 69.9 %, to invisible particles (neutrinos) is 20 % and the branching ratio to charged leptons is approximately 3.4 % per lepton flavour (including τ) [9]. The branching ratio to each of the lepton flavours are approximately the same, due to lepton universality [16]. The branching ratios and some other properties of the Z boson can be seen in table 2.2.

The different branching ratios mean that there will be more ZZ events where one or both Z bosons decay to hadrons or neutrinos than events where both Z bosons decay to leptons. Similarly, τ leptons decay to final states including neutrinos and sometimes hadrons. However, in the pp collisions at the LHC (see chapter 3) there are many background processes which are hard to differentiate from $Z \to$ hadrons decays and $Z \to \nu\nu$ decays are not visible in the detector, so this thesis will focus on the channel where each Z boson decays to an opposite charge pair of electrons or muons.

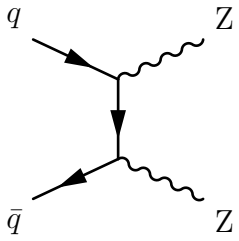

(a) t-channel

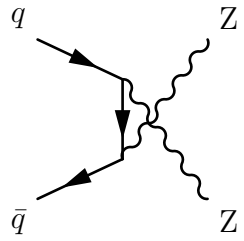

(b) u-channel

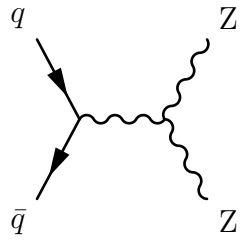

(c) s-channel

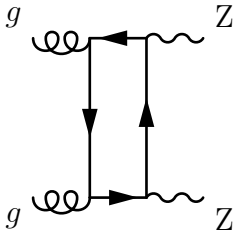

(d) t-channel gg production.

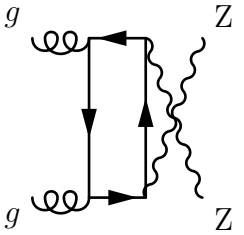

(e) u-channel gg production

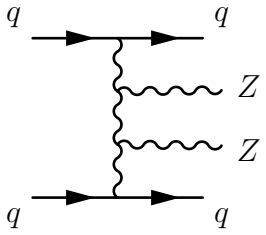

(f) Vector boson scattering production by exchange of a W boson. This is the dominant Feynman diagram of the $ZZ \to 4\ell qq$ sample.

Figure 2.1: The leading order Feynman diagrams for ZZ production through the $q\bar{q}$ and gg initial states at the LHC. Diagram (c) includes the Z^*ZZ or γ^*ZZ neutral gauge couplings which are not allowed at tree level in the SM (see section 2.3). The contributions (d) and (e) from gluon processes are suppressed by α_s compared to the processes in (a) and (b).

	Z boson
Spin	1
Charge	0
Mass	$m_Z = 91.1876 \pm 0.0023$ GeV
Width	$\Gamma_Z = 2.4952 \pm 0.0023$ GeV
Branching ratios	$BR(Z \to e^- e^+) = 3.363 \pm 0.004\%$
	$BR(Z \to \mu^- \mu^+) = 3.366 \pm 0.007\%$
	$BR(Z \to \tau^- \tau^+) = 3.370 \pm 0.008\%$
	$BR(Z \to \text{invisible}) = 20.0 \pm 0.06\%$
	$BR(Z \to \text{hadrons}) = 69.9 \pm 0.06\%$

Table 2.2: Properties of the Z boson [9].

2.3 Triple gauge couplings

The interacting term of the gauge field component of the SM electroweak Lagrangian density can be written as

$$\mathcal{L}_I = \frac{g_2}{2}\epsilon_{ijk}(\partial^\mu W_i^\nu - \partial^\nu W_i^\mu)W_{j\mu}W_{k\nu} - \frac{g_2^2}{4}\epsilon_{ijk}\epsilon_{ilm}W_j^\mu W_k^\nu W_{l\mu}W_{m\nu}. \tag{2.14}$$

The two terms correspond to triple and quadruple couplings, respectively. In the former can be seen the ϵ_{ijk} that forbids the coupling ZZV at tree level in the SM (where V is Z or γ), which arises due to the non-Abelian nature of the $SU(2)$ symmetry. A Feynman diagram involving the forbidden s-channel process can be seen in fig. 2.1c.

2.3.1 Anomalous triple gauge couplings (aTGCs)

Beyond the SM, the triple gauge couplings can be non-zero (then referred to as anomalous triple gauge couplings, aTGCs). For on-shell outgoing Z bosons the vertex function for ZZV (V is Z or γ) can be written as [17]

$$g_{ZZV}\Gamma_{ZZV}^{\alpha\beta\mu} = e\frac{P^2 - M_V^2}{M_Z^2}\left(if_4^V\left(P^\alpha g^{\mu\beta} + P^\beta g^{\mu\alpha}\right) + if_5^V\epsilon^{\mu\alpha\beta\rho}\left(q_1 - q_2\right)_\rho\right), \tag{2.15}$$

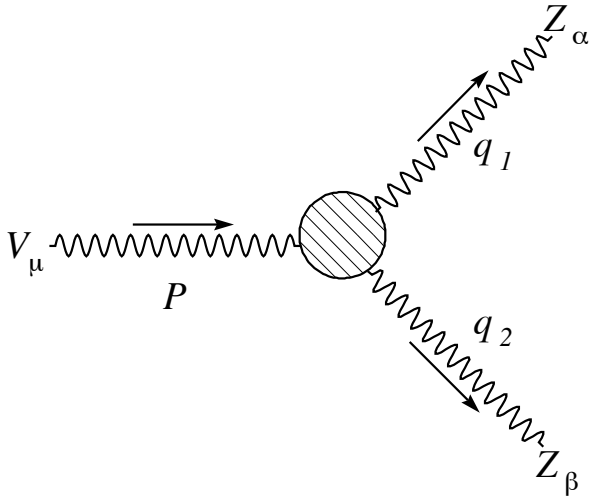

Figure 2.2: Feynman diagram of a triple gauge coupling [17].

where $g_{ZZV}\Gamma^{\alpha\beta\mu}_{ZZV}$ is the ZZV vertex function, e is the electric charge of the proton, M_V is the mass of the boson V, P is the four-momentum of the incoming Z/γ, q_1 and q_2 are the four-momenta of the outgoing Z bosons (as seen in fig. 2.2), the factor $P^2 - M_V^2$ is a consequence of Bose symmetry and f_i^V $(i = 4, 5)$ are four dimensionless, complex coupling constants f_4^γ, f_4^Z, f_5^γ and f_5^Z. The f_4^V coupling constants violate CP-invariance and the f_5^V coupling constants violate parity conservation.

The cross section of the ZZ process with given aTGCs is proportional to the square of the matrix elements, which include a vertex factor as described in eq. (2.15). Since the matrix element is linear in the couplings f_i^V, any differential cross section of the ZZ process with aTGCs present can be written as

$$\begin{aligned} d\sigma(f_4^\gamma, f_5^\gamma, f_4^Z, f_5^Z) = & F_{00} + f_4^\gamma \; F_{01} + f_5^\gamma \; F_{02} + f_4^Z \; F_{03} + f_5^Z \; F_{04} \\ & + (f_4^\gamma)^2 F_{11} + f_5^\gamma f_4^\gamma F_{12} + f_4^Z f_4^\gamma F_{13} + f_5^Z f_4^\gamma \; F_{14} \\ & + (f_5^\gamma)^2 \; F_{22} + f_4^Z f_5^\gamma F_{23} + f_5^Z f_5^\gamma \; F_{24} \\ & + (f_4^Z)^2 F_{33} + f_5^Z f_4^Z \; F_{34} \\ & + (f_5^Z)^2 \; F_{44}, \end{aligned} \tag{2.16}$$

where $d\sigma(f_4^\gamma, f_5^\gamma, f_4^Z, f_5^Z)$ is any differential cross section and F_{jk} is the contribution to the differential cross section from a certain combination of couplings. The contribution F_{00} is independent of f_i^V and so by definition, it is the SM contribution. The terms

where $j \neq k$ are interference terms and tend to be small compared to other terms (except when the terms in eq. (2.15) are allowed to cancel, corresponding to F_{12} and F_{34}).

The kinematic properties of the triple gauge coupling Feynman diagrams are different to those of the other diagrams and this fact can be used to set a limit on the aTGCs, as described in chapter 8. This thesis uses the p_{T} of the leading Z boson candidate (the p_{T} being the momentum, projected onto the transverse plane, which is the plane orthogonal to the beam of the collider, and the leading Z boson candidate being the one with the highest p_{T}) as observable of interest, a histogram of which can be seen in fig. 2.3. This variable was found to be more sensitive than the invariant mass of the ZZ system and the p_{T} of the leading lepton (which are variables that have been used in other analyses [15, 18, 19]).

2.3.2 Unitarity and form factor

If the neutral triple gauge couplings are included, their contribution grows unbounded with energy until the sum of the probabilities of all final states exceeds unity (i.e. unitarity is violated). Thus, if there are non-zero neutral triple gauge couplings, there must be some energy scale at which another effect cancels the aTGCs, or the effective vertex factor in some other way becomes invalid. Some previous analyses consider a *form factor* that suppresses the aTGCs at some arbitrary energy scale [18]. The analysis in this thesis does not use such a form factor since it was found to have a negligible impact.

2.4 Monte Carlo simulation

For comparison to theory and estimation of reconstruction efficiencies as well as code testing, simulated data were generated using Monte Carlo (MC) generators which can simulate events of physics processes (*hard interaction*) as well as calculate their matrix elements. Simulations and calculations can be done at Leading Order (LO), Next to Leading order (NLO) or Next to Next to Leading Order (NNLO) of QCD matrix-element calculations.

The generators used for this thesis also include *initial* and *final state radiation* (additional particles radiated from the incoming or outgoing particles). After the hard interaction has been generated, QCD parton showering and non-perturbative hadroni-

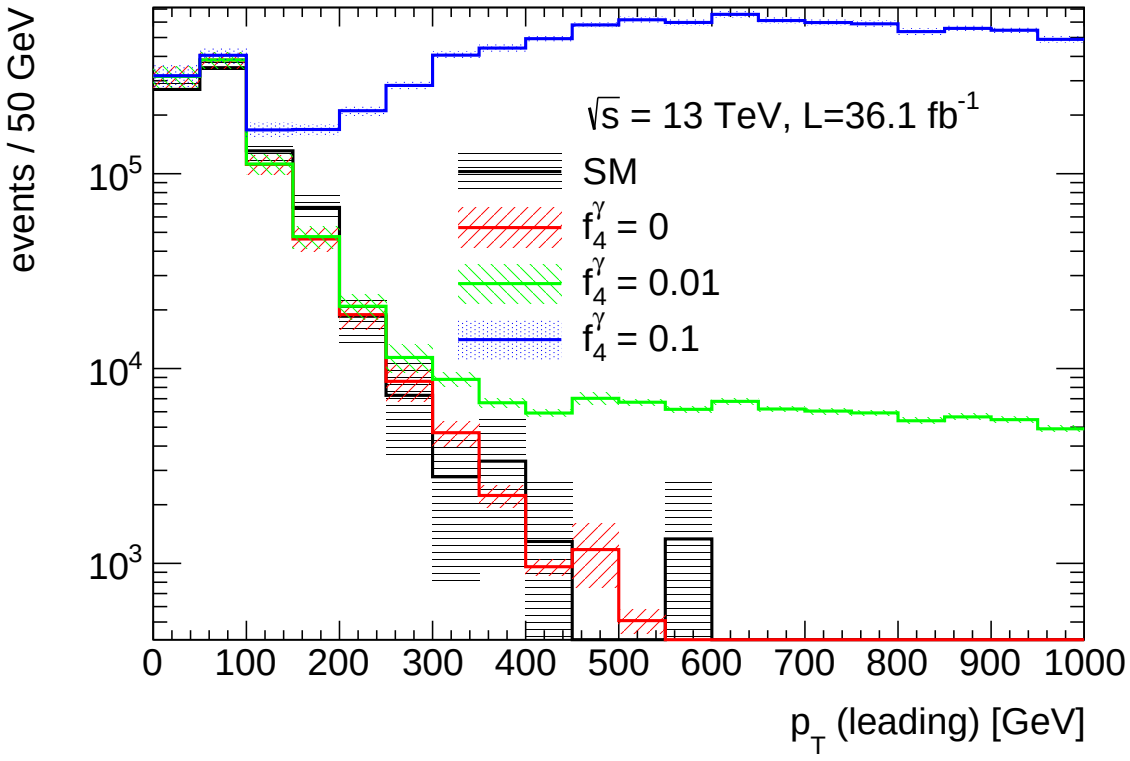

Figure 2.3: The distribution of p_{T} (momentum projected onto the transverse plane, see section 3.2.1) of the Z boson with the highest p_{T} with different neutral gauge coupling strengths in signal events (generated at $\sqrt{s} = 13\,\mathrm{TeV}$, normalised to a luminosity of 36.1 fb^{-1}, estimated with SHERPA, see section 2.4) that pass the truth fiducial selection (see section 4.1). The SM line is generated without anomalous triple gauge couplings. The other lines have f_4^γ turned on to different values (the other couplings turned off) as described in section 8.1 (the SM and $f_4^\gamma = 0$ lines are independent samples describing the same thing). The error bands represent the statistical uncertainty.

sation are modelled by the generators (although it is possible to generate events using one generator and model the parton showering and hadronisation using another). The generators also include simulations of the *underlying event*, i.e. the partons that did not take part in the hard scatter, and particles not coming from the pp scattering (such as thermal neutrons from the cavern and cosmic rays) are overlaid.

The generators output the four momenta of the particles resulting from the pp interaction in each simulated event, which is known as the *truth* information.

2.4.1 Parton distribution functions and perturbative calculations

The calculation for the cross section contribution from each event requires *parton distribution functions* (PDFs) that describe the distribution of partons inside hadrons. Each PDF $f(x, \mu_F)$ is the probability density for a strongly interacting particle (up, down, anti-up, strange, gluon etc.), carrying the fraction x of the momentum of the proton, to be the initial state of a hard interaction. The quantity μ_F is the *factorisation scale*, a scale which characterises the factorization of the total cross section calculation into the interaction described by the hard perturbative partonic interaction, and the non-perturbative long range interactions defining the structure of the proton. It is usually chosen to be approximately equal to the momentum transfer of the hard scatter.

When a process has coupling strengths much smaller than unity, higher order terms of that process can be calculated with perturbative calculations. This involves absorbing loop corrections into the coupling strengths, a process known as *renormalisation*. The three couplings g_1, g_2 and g_3 can be expressed in terms of the strong coupling constant α_s, the fine structure constant α and the Weinberg angle θ_W as

$$g_1 = \frac{\sqrt{4\pi\alpha}}{\cos\theta_W}, \quad g_2 = \frac{\sqrt{4\pi\alpha}}{\sin\theta_W}, \quad g_3 = \sqrt{4\pi\alpha_s}. \tag{2.17}$$

When loop corrections are absorbed into these couplings, they are no longer constant with respect to energy so a *renormalisation energy scale* μ_R is introduced, at which the coupling strengths are determined. The effective α and α_s, determined at the Z mass energy scale, are 1/128 and 0.118, respectively [20].

The cross section of an interaction between two protons $pp \to X$ is given by

$$\sigma_{pp\to X} = \int dx_1 dx_2 f_a(x_1, \mu_F) f_b(x_2, \mu_F) \hat{\sigma}_{ab\to X}(x_1, x_2, \mu_R), \tag{2.18}$$

where x_1 and x_2 are the fraction of the protons' momenta carried by each interacting parton, a and b are their respective flavour (f_a and f_b are the corresponding PDFs), $\hat{\sigma}_{ab\to X}$ is the perturbatively calculated partonic cross section for the process $ab \to X$ and μ_R is the renormalisation scale.

The PDFs are provided by several independent analysis groups, fitting models to a large body of experimental data.

2.4.2 Monte Carlo samples

The MC signal samples used in this thesis can be seen in table 2.3 along with the generators and PDFs used to generate them, as well as the order to which they were generated.

The gg sample is generated at LO, but total cross section calculations exist at NLO. The cross sections at LO and NLO are $2.8^{+0.7}_{-0.6}$ fb and 4.7 ± 0.4 fb, respectively ($\sqrt{s} = 13$ TeV, Z boson mass window 60-120 GeV, uncertainties from factorisation and renormalisation scales) [23]. The ratio of those cross sections, 1.67 ± 0.25, is applied to the cross section of the $gg \to ZZ$ LO sample to correct for this difference (known as a k-factor). The cross sections used for normalisation (as seen in table 2.3) are generated in a phase space without the mass constraint, which is why it is not equal to 2.8 fb.

For the study of aTGCs, Sherpa is used to produce a sample with the four f_i^V coupling strenths set to 0.1. This sample can be reweighted to any other set of couplings, as described in chapter 8.

For further use of the Monte Carlo samples, the events are simulated to take place in the ATLAS detector. This is discussed further in section 3.3.

2.5 Predictions and previous measurements

Predicted $pp \to ZZ \to 4\ell$ NNLO cross sections are provided by Matrix [24]. It uses the PDFs NNPDF 3.0 NNLO [25] and includes electroweak corrections [26,27] as well as the k-factor of 1.67 on the gg contribution. The cross section for the $pp \to ZZ \to 4\ell qq$ sample discussed in section 2.4.2 is added to each cross section prediction as well.

Four fiducial cross sections, closely matching the ATLAS detector acceptance (fully defined in section 4.1), are considered, as well as one total phase space corresponding to all ZZ events with both Z bosons in the $66\,\text{GeV} < m_Z < 116\,\text{GeV}$ mass range (regardless of decay channel). The total predictions can be seen in table 2.4. Previous

measurements of the cross section can be seen in table 2.5. Analyses labelled 2016 uses data from 2015 and 2016.

The SM predicts all neutral triple gauge couplings to be zero.

Cross sections of $pp \to ZZ \to 4\ell$ production have been measured in the past (sometimes combined with $pp \to ZZ \to 2\ell 2\nu$). CMS is another multipurpose detector situated on the LHC [28], which has performed measurements at $\sqrt{s} = 13\,\text{TeV}$ as well as 7 and 8 TeV, like ATLAS (analyses labelled 2016 uses data from 2015 and 2016).

The total cross section results can be seen in table 2.5. The most important results are also compared to the results from this thesis in chapter 7. These measurements are all consistent with the SM. The cross sections are expected and observed to increase with $\sqrt{s}$. Since the dominant uncertainty is statistical, the uncertainty of the measurements improve with growing luminosity. Some measurements are made using a combination of the 4ℓ channel and $2\ell 2\nu$ channel, which improves the statistics greatly, but which introduces other large uncertainties associated with the neutrinos.

Limits on anomalous triple gauge couplings (f_4^γ,f_5^γ,f_4^Z,f_5^Z) have also been set previously. Those limits can be seen in table 2.6. Limits improve (become tighter) with higher $\sqrt{s}$ and luminosity. Limits tend to be symmetrical (since the main contribution is quadratic in f_i^V) and for a given experiment, the limits of the different coupling strengths are similar (within 40 %). Before the LHC was built, the same tunnels were occupied by the *Large Electron-Postitron* collider (LEP). Experiments at LEP (ALEPH, DELPHI, L3, OPAL) have also provided limits on the anomalous triple gauge couplings, which can also be seen in table 2.6 [33].

2.6 Conclusions

The Standard Model is a model which describes most known particles and forces, including the Z boson. The Higgs mechanism gives mass to the gauge bosons. The aTGC additions to the SM are also discussed in this chapter.

Process	Generator	PDFs	Order	Cross section	Events
$qq \to 4\ell$	Sherpa 2.2.1 [21]	NNPDF3.0$_{\text{NNLO}}$	NLO (2,3j@LO)	1.2557 pb	17 999 300
$gg \to 4\ell$	Sherpa 2.1 [22]	CT10	LO (incl. H^{0*})	20.931 fb	492 000
$pp \to 4\ell qq$	Sherpa 2.1	CT10	LO	31.496 fb	60 000
$pp \to 4\ell$ (aTGC)	Sherpa 2.1	CT10	LO	8.7519 pb	100 000

Table 2.3: Signal processes and the generators and PDFs used to model them, as well as the cross section they are normalised to (the generated events and cross sections are generated in phase spaces that include off-shell Z bosons) and the number of events generated. The (2,3j@LO) means that two and three hadron contributions are calculated at LO rather than NLO. The gg sample also requires a k-factor of 1.67 (not included in this table). The aTGC sample is generated with all anomalous triple gauge couplings set to 0.1, which is why the cross section is larger than the sum of the samples without aTGCs.

	Predicted cross section	
Fiducial $4e$	$10.9^{+0.5}_{-0.4}$	fb
Fiducial $2e2\mu$	$21.2^{+0.9}_{-0.8}$	fb
Fiducial 4μ	$10.9^{+0.5}_{-0.4}$	fb
Fiducial combined	$42.9^{+1.9}_{-1.5}$	fb
Total	$16.9^{+0.6}_{-0.5}$	pb

Table 2.4: Theoretical predictions of fiducial and total cross sections at $\sqrt{s} = 13\,\text{TeV}$ as calculated by MATRIX for $qq \to ZZ \to 4\ell$ and $gg \to ZZ \to 4\ell$ (with a k-factor of 1.67 ± 0.25 on the gg contribution) and $pp \to ZZ \to 4\ell qq$. The uncertainties shown are the QCD uncertainties, obtained by varying the factorisation and renormalisation scales by a factor two.

Experiment	$\sqrt{s}$	Luminosity	Total cross section	ref.	
CMS 2016	13 TeV	35.9 fb^{-1}	$17.8\ ^{+1.1}_{-1.1}$ pb	[29]	
ATLAS 2015	13 TeV	3.2 fb^{-1}	$16.7\ ^{+2.6}_{-2.2}$ pb	[14]	
CMS 2015	13 TeV	2.6 fb^{-1}	$14.6\ ^{+2.0}_{-1.9}$ pb	[30]	
ATLAS 2012	8 TeV	20.3 fb^{-1}	$7.3\ \pm 0.5$ pb	[18]	includes $2\ell 2\nu$
CMS 2012	8 TeV	19.6 fb^{-1}	$7.7\ \pm 0.8$ pb	[19]	
ATLAS 2011	7 TeV	4.6 fb^{-1}	$6.7\ ^{+0.9}_{-0.8}$ pb	[31]	includes $2\ell 2\nu$
CMS 2011	7 TeV	5.0 fb^{-1}	$6.4\ ^{+1.0}_{-0.9}$ pb	[32]	

Table 2.5: Previous measurements of $pp \to ZZ \to 4\ell$ cross sections. The CMS collaboration mass window is $60\,\text{GeV} < m_Z < 120\,\text{GeV}$ whereas the ATLAS collaboration uses $66\,\text{GeV} < m_Z < 116\,\text{GeV}$.
The cross sections grow with $\sqrt{s}$. The uncertainties shrink with growing luminosity, due to the uncertainties being dominated by statistics. Most of the work in this thesis is done as a part of the ATLAS 2016 analysis.

Experiment	$\sqrt{s}$ Luminosity	Limits $[10^{-3}]$		ref.
CMS 2016	13 TeV	$-1.33 < f_4^\gamma < 1.32$	$-1.17 < f_4^Z < 1.10$	[29]
	35.9 fb^{-1}	$-1.23 < f_5^\gamma < 1.30$	$-1.00 < f_5^Z < 1.25$	
ATLAS 2012	8 TeV	$-3.8 < f_4^\gamma < 3.8$	$-3.3 < f_4^Z < 3.2$	[18]
	20.3 fb^{-1}	$-3.8 < f_5^\gamma < 3.8$	$-3.3 < f_5^Z < 3.3$	
CMS 2012	8 TeV	$-5 < f_4^\gamma < 5$	$-4 < f_4^Z < 4$	[19]
	19.6 fb^{-1}	$-5 < f_5^\gamma < 5$	$-4 < f_5^Z < 4$	
ATLAS 2011	7 TeV	$-15 < f_4^\gamma < 15$	$-13 < f_4^Z < 13$	[31]
	4.6 fb^{-1}	$-16 < f_5^\gamma < 15$	$-13 < f_5^Z < 13$	
CMS 2011	7 TeV	$-13 < f_4^\gamma < 15$	$-11 < f_4^Z < 12$	[32]
	5.0 fb^{-1}	$-14 < f_5^\gamma < 14$	$-12 < f_5^Z < 12$	
LEP combined		$-170 < f_4^\gamma < 190$	$-300 < f_4^Z < 290$	[33]
		$-340 < f_5^\gamma < 380$	$-380 < f_5^Z < 360$	

Table 2.6: Previous measurements of aTGCs CL_s limits.

Chapter 3

LHC and the ATLAS detector

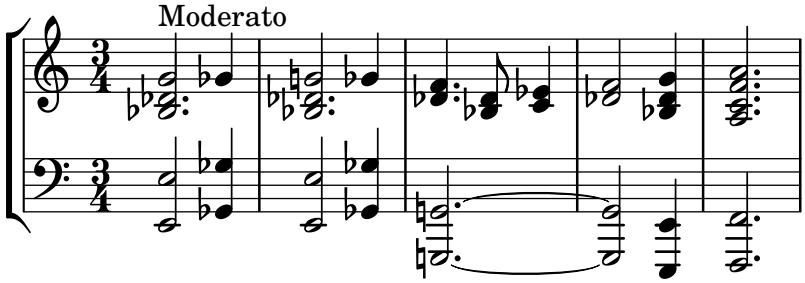

— Richard Wagner, *Der Ring des Nibelungen, 1878*

The Large Hadron Collider is a synchrotron in Geneva, Switzerland which collides protons at a centre-of-mass energy of $\sqrt{s} = 13\,\text{TeV}$. On the LHC is located the ATLAS detector, a multipurpose detector containing an Inner Detector, Calorimeters and a Muon system, as well as magnets and a trigger system. This thesis uses collisions delivered by the LHC and recorded by the ATLAS detector. This chapter provides details on the LHC and the ATLAS detector.

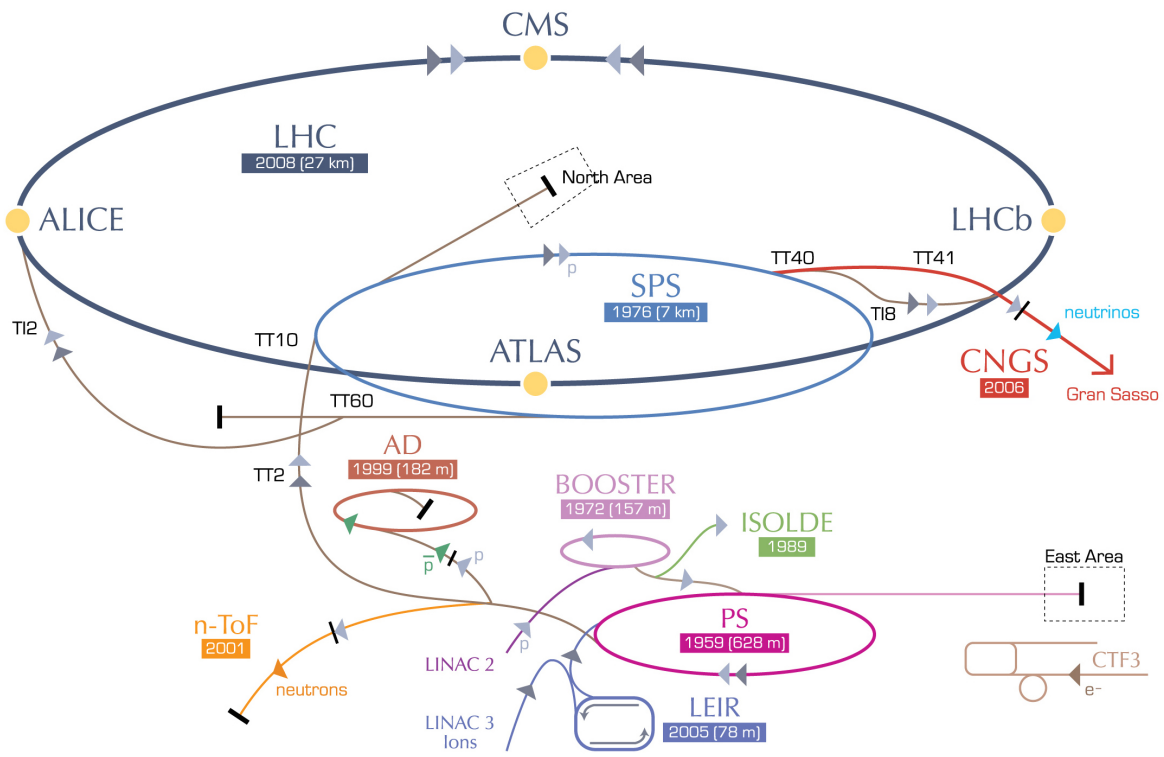

Figure 3.1: The acceleration complex at CERN. Protons for proton-proton collisions go through LINAC2, PSB (BOOSTER), PS and SPS before reaching the LHC. [35]

3.1 Large Hadron Collider

The Large Hadron Collider (LHC) [2] is a particle accelerator and collider, installed at CERN in Geneva, Switzerland. It is a synchrotron with a total circumference of 26.7 km, located 45 to 170 m underground, which can accelerate protons as well as heavy ions (typically lead nuclei).

Protons are injected into the LHC through an injector chain consisting of a Linear Accelerator (LINAC2, protons accelerated to 50 MeV), the Proton Synchrotron Booster (PSB, 1.4 GeV), the Proton Synchrotron (PS, 25 GeV), the Super Proton Synchrotron (SPS, 450 GeV) before the protons finally reach the LHC. The protons are divided into two beams which go around the LHC in different directions, each reaching a maximum energy of 6.5 TeV [2, 34]. The accelerator chain can be seen in figure 3.1.

The LHC consists of eight straight sections, connected by eight arc sections and contains a 400 MHz superconducting cavity system used to accelerate the particles. The LHC also contains 1380 superconducting magnets, used to bend the accelerated

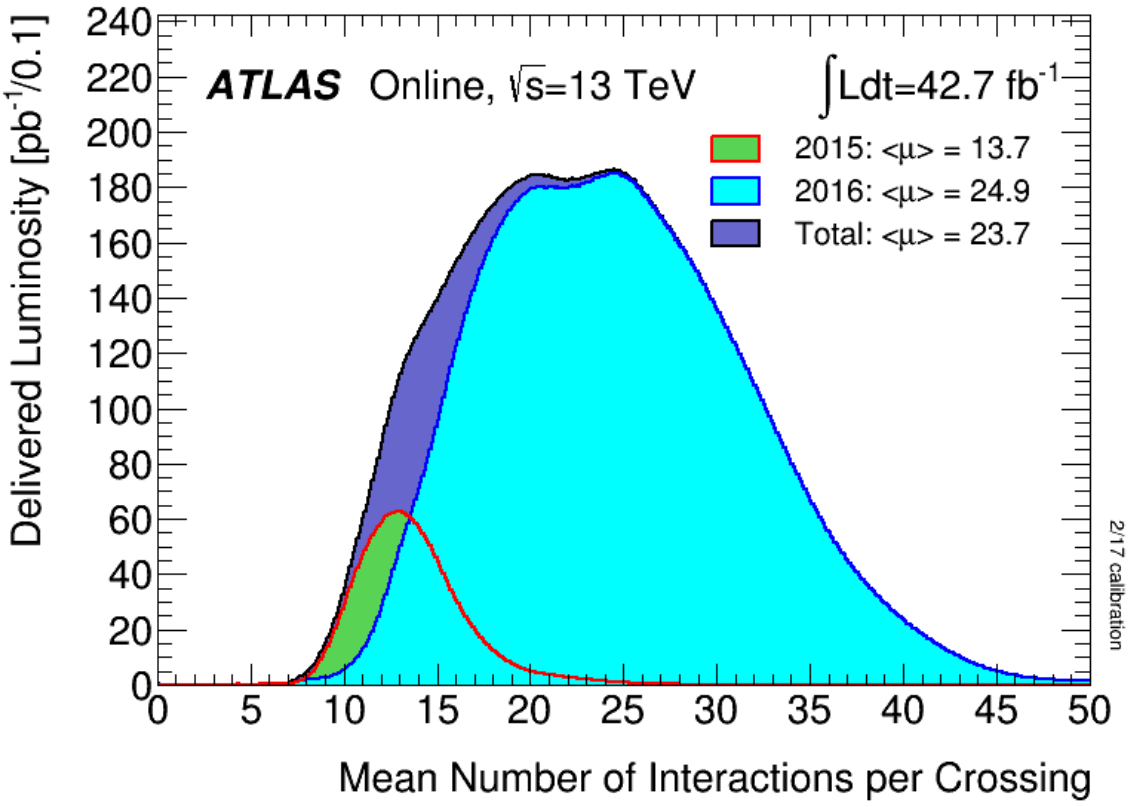

Figure 3.2: The luminosity-weighted distribution of the mean number of interactions per crossing, $\langle\mu\rangle$, for the pp collision data recorded in 2015 and 2016 at 13 TeV centre-of-mass energy [38].

particles around the LHC as well as to focus the particle beams. In four of the straight sections there are beam crossings where protons collide with a maximum centre-of-mass energy ($\sqrt{s}$) of 13 TeV. At each of the four beam crossing points, there is a major detector, ALICE [36], LHCb [37], CMS [28] and ATLAS [1].

Each accelerated beam consists of up to 2808 bunches with each bunch containing up to 1.1×10^{11} protons. The bunches are spaced 25 ns apart, which corresponds to a bunch crossing rate of 40 MHz. It is possible for multiple proton interactions to be recorded as one event. This is known as pile-up [39]. Pile-up is usually quantified in terms of the average number of interactions per bunch crossing, μ, the distribution of which can be seen in fig. 3.2.

The details of the data used in the analysis in this thesis can be seen in table 3.1.

The collisions produce a large number of physics processes, including the processes

	2015	2016	Total
Center of mass energy $\sqrt{s}$			13 TeV
Integrated luminosity $\int \mathcal{L}dt$	3.2 fb^{-1}	32.9 fb^{-1}	36.1 fb^{-1}
Bunch spacing			25 ns
Bunch crossing rate			40 MHz

Table 3.1: Details of data gathered during 2015 and 2016. Blank fields indicate that the value under "Total" is true for the entire data taking.

shown in fig. 2.1. A hadron collider such as the LHC also gives rise to a large number of QCD physics processes with hadronic final states. One of the reasons for chosing the 4ℓ channel for this thesis is the difficulty in telling the QCD events apart from events containing Z bosons decaying to hadrons.

The LHC started delivering physics beams in 2008. Since then, upgrades have been made and data taking is ongoing at the time of writing. Data taking is planned to continue until 2022, and is planned to continue after upgrades, in particular an upgrade called the High Luminosity LHC, planned to be ready for data taking in 2025 [40].

3.2 The ATLAS detector

At Point 1 of the LHC sits the ATLAS (A Toroidal LHC ApparatuS) detector, which is associated with the ATLAS experiment. It is a cylindrical multi-purpose detector, with a diameter of 25 m, a length of 44 m and a mass of ca 7000 tonnes, containing an Inner Detector (ID), a Calorimeter System and a Muon System (MS), which are designed for detecting and measuring different types of particles [1]. The detector can be seen in fig. 3.3.

In addition to the subdetectors that are discussed later in this chapter, the detector has a system of magnets, consisting of one solenoid located just outside the Inner Detector (providing a 2 T magnetic field inside the Inner Detector), a barrel toroid system in the outer detector (providing a 0.5 T magnetic field in the Muon Systems) and two endcap toroids. When charged particles pass through the magnetic field, their paths bend and the curvature of the path can be used to determine the momentum of the particles.

ATLAS starts recording events when a new beam is delivered by the LHC. Under normal conditions, data taking continues until the beams are dumped. The beam

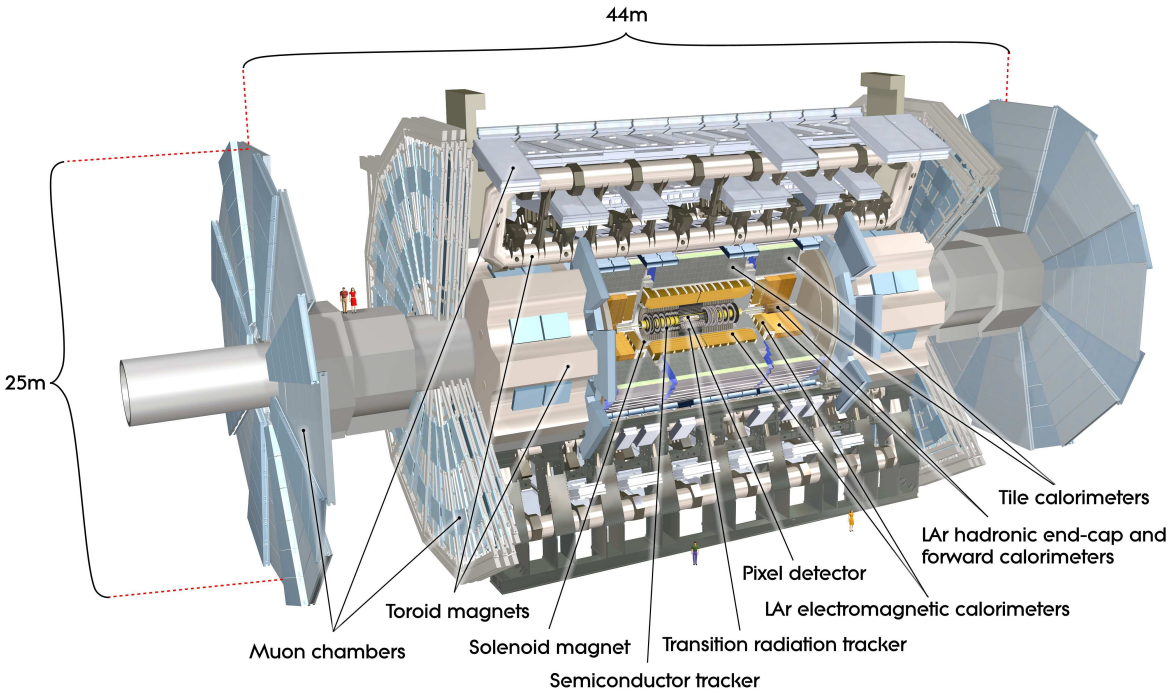

Figure 3.3: Cut-away view of the ATLAS detector with its major subsystems labelled. [1]

intensity falls with time and the beams are typically dumped when the instantaneous luminosity drops to half its initial value (this takes circa 12 h). The instantaneous luminosity and the detector status are saved in time blocks called luminosity blocks (typically around 60 s).

3.2.1 Coordinate system

The coordinate system used to describe the ATLAS detector and the processes in it is defined as a right-handed coordinate system with the nominal interaction point as its origin. The x, y and z axes are directed towards the centre of the LHC, vertically up, and along the beam direction respectively. The azimuthal angle ϕ is measured around the beam axis and the angle θ is defined as the polar angle from the beam axis. The *pseudorapidity* is defined as

$$\eta = -\ln\left(\tan\left(\frac{\theta}{2}\right)\right). \tag{3.1}$$

The x-y plane is referred to as the transverse plane, and the component of the momentum of an object in this plane is the transverse momentum, p_{T}.

The separation between two objects a and b is defined as follows:

$$\Delta R(a,b) = \sqrt{(\Delta\eta_{a,b})^2 + (\Delta\phi_{a,b})^2} \tag{3.2}$$

where $\Delta\eta_{a,b}$ is the difference in η between object a and b, and $\Delta\phi_{a,b}$ is the angle between objects a and b in the transverse plane. This should not be confused with R which is used to denote the transverse distance from the beam axis ($R = \sqrt{x^2 + y^2}$).

3.2.2 Inner detector

The Inner Detector (ID) is the collective name of the three innermost subdetectors of ATLAS. The active material of the ID reaches from a transverse distance of R =31 mm from the beam to 1.15 m. Closest to the beam is the pixel detector, then comes a semiconductor tracker and finally a transition radiation tracker [41]. The structure of the inner detector can be seen in fig. 3.4.

1. Pixel detector (PIX)

   The pixel detector is the innermost subdetector of ATLAS. It consists of silicon pixels with sizes 50 µm × 400 µm (the innermost layer is called the Insertable B-Layer, IBL [42], and its pixels are 50 µm × 250 µm). These are arranged around

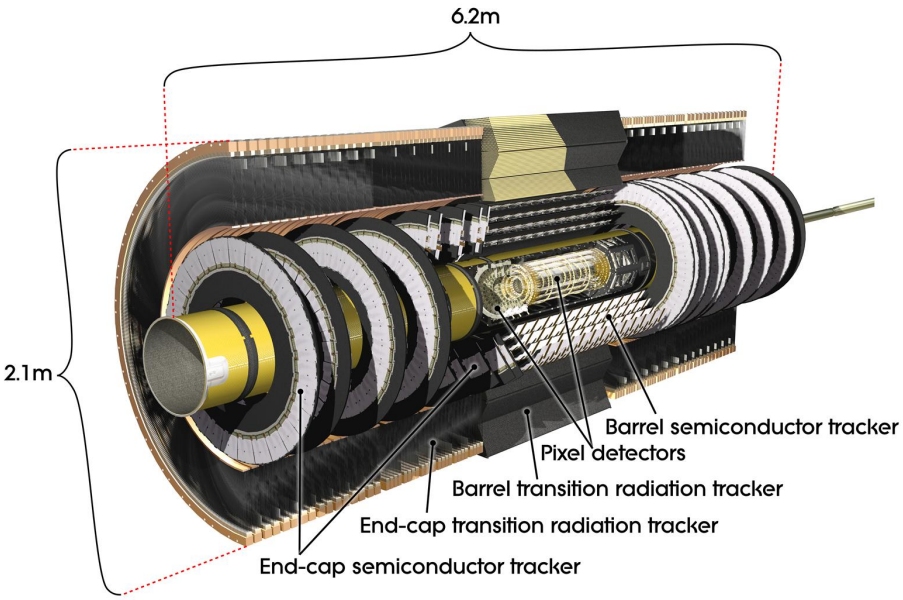

Figure 3.4: The inner detector of ATLAS. The IBL is not represented in this picture. [1]

the beam in four concentric barrel layers with radii 3 (IBL), 5, 9 and 12 cm as well as three end cap layers on each side (covering $|\eta| < 2.7$), all arranged so that a track from the interaction point typically produces four hits [42, 43]. The resulting resolution is 11 µm × 69 µm in $\Delta R\phi \times \Delta z$ (in the barrel, slightly looser in the end caps).

2. SemiConductor Tracker (SCT)

   The SemiConductor Tracker consists of silicon microstrip detectors with a pitch of 80 µm and length 13 cm (placed along the z-axis in the barrel region). Each detector layer consists of two layers of microstrips, placed at a stereo angle of 40 mrad (so that a resolution in the dimension parallel to the strips can be obtained), giving a resolution of 16 µm × 580 µm (in $R\Delta\phi \times \Delta z$). There are four concentric barrels (at 30, 37, 44 and 51 cm from the beam) and nine end cap layers on each side, covering a total η range of $|\eta| < 2.5$ [44].

3. Transition Radiation Tracker (TRT)

   The TRT is the outer part of the Inner Detector. It consists of gas straws (4 mm in diameter) containing a mixture of xenon, carbon dioxide and oxygen. The xenon is ionised by passing charged particles. The TRT has a resolution of 170 µm in

$R\Delta\phi$.

A track typically gives 36 hits in the TRT. The straws are arranged in a barrel region, ranging from 56 to 107 cm from the beam, and end caps, covering a total η range of $|\eta| < 2.5$. The TRT also uses transition radiation photons to aid electron identification [45].

3.2.3 Calorimeters

The ATLAS detector has a system of calorimeters, which is used to measure the energy of particles. The calorimeters reach from 1.4 m to 4.3 m from the beam, plus two end caps [46, 47].

1. Liquid Argon Calorimeter (LAr)

   Liquid Argon calorimeters with lead absorbers are used in the barrel region of the detector (EMB) as well as the end caps (EMEC) for measurement of electromagnetic showering. The barrel has three layers and the calorimeter cell sizes in the different layers are 0.003×0.1, 0.025×0.025 and 0.05×0.025, respectively, given in $\Delta\eta \times \Delta\phi$ (slightly coarser in regions with $|\eta| > 1.4$). In the end caps, there are also liquid argon calorimeters with copper absorbers for measurement of hadronic showering (HEC). On the inside of the detector barrel is a presampler layer (liquid argon without absorber), used to estimate how much energy an object has lost before reaching the calorimeter.

   In the forward region, there is also a forward LAr calorimeter (FCal) which completes the LAr total range of $|\eta| < 4.9$ [46]. The LAr electron energy resolution is approximately 3 % for an electron with p_{T} of 20 GeV and improves to approximately 1 % at high p_{T} [48, 49].

2. Tile Calorimeter (Tile)

   The Tile calorimeter is located outside the barrel LAr calorimeter and is intended to measure the energy of hadronic showers. It consists of plastic scintillators and low-carbon steel absorbers and spans the region $|\eta| < 1.7$. The tile calorimeter has three sampling layers, with $\Delta\eta \times \Delta\phi$ tile sizes of 0.1×0.1, 0.1×0.1 and 0.2×0.1, respectively. The resulting energy resolution is around 1 % [50].

Between the extended barrel and endcap calorimeters, in the range $1.37 < |\eta| < 1.52$, is a region known as the *crack region*. This region contains many wires and power cables

for the Inner Detector and Calorimeters, and consequentially has lower efficiencies.

3.2.4 Muon detectors

The outermost system of ATLAS is the Muon System (MS), which provides precise measurements of muons. The MS consists of Monitored Drift Tube Chambers (MDT), Cathode-Strip Chambers (CSC), Resistive Plate Chambers (RPC) and Thin Gap Chambers (TGC). The MS spans $|\eta| < 2.7$ and starts 4.6 m and ends 10.2 m from the beam [1].

1. Monitored Drift Tubes (MDT)

   The monitored drift tubes consist of pressurised, 30 mm diameter tubes, filled with a mixture of argon and carbon dioxide that ionises when a charged particle travels through it. Each chamber has an average resolution of 35 µm in its bending plane. The MDT is structured as three layers around the barrel and three end cap wheels on each side, each with three to eight sheets of drift tubes. The MDTs cover a range of $|\eta| < 2.7$ (except in the innermost layer, which is replaced by the CSC in the range $2.0 < |\eta| < 2.7$).

2. Cathode-Strip Chambers (CSC)

   The cathode-strip chambers are multi-wire proportional chambers with segmented cathode readout. The CSC has a spatial resolution of 60 µm per plane and about 5 mm in the non-bending direction. The CSC replace the MDT in the end caps, in the range $2.0 < |\eta| < 2.7$, since the MDTs are unsuitable for the high rates and radiation close to the beam.

3. Resistive Plate Chambers (RPC) and Thin Gap Chambers (TGC)

   The resistive plate and thin gap chambers are thin layers of muon detectors that are located between the layers of the MDT and the CSC. They provide quick muon identification as a part of the ATLAS trigger system (see section 3.2.6)

Together, these systems provide information for the muon reconstruction. Muons are reconstructed stand-alone (using only the MS) or combined with the ID or calorimeters. The combined MS momentum resolution is approximately 2 % [51].

3.2.5 Luminosity

The luminosity is a measure of the rate of collisions in a collider such as the LHC. The amount of data taken is quoted as luminosity integrated over time (*integrated luminosity*) and the uncertainty associated with the luminosity is one of the leading uncertainties in the analysis presented in this paper. The luminosity value used in this analysis is a combination of several measurements, the most important of which are track counting in the ID and measurements by two subdetectors called BCM and LUCID [52].

BCM consists of four 8×8 mm diamond sensors located around the beam, 1.8 m from the interaction point in each direction, which records hits when one of the sensors produces a signal over a preset threshhold. LUCID is a Cherenkov detector, consisting of aluminium tubes of C_4F_{10} and photomultiplier tubes, located around the beam, 17 m from the interaction point in each direction, recording Cherenkov radiation detected by the photomultiplier tubes.

The luminosity measuring methods are calibrated using a van der Meer scan, which is a scan of the beam separation between two beams (with tailored beam conditions). The uncertainty on the beam conditions of the van der Meer scan are the leading source of uncertainty for the luminosity. The integrated luminosity used in this thesis was measured to be $36.1 \pm 1.1\,\text{fb}^{-1}$(3.1 % uncertainty) [53].

3.2.6 ATLAS trigger system

The ATLAS detector gathers in full around 1.6 Mb of information per bunch crossing, which is unfeasible to record and store at the rate of bunch crossings (40 MHz). A trigger system is designed to reject events that are unlikely to be of interest for physics analysis [54, 55]. ATLAS has a two-level system of triggers for data gathered in 2015 and 2016, consisting of a hardware-based first level of triggers (L1) and a software-based second level (*Higher Level Trigger*, HLT).

The L1 trigger system uses custom electronics and coarse granularity information from the Calorimeters and Muon Systems to determine regions of interest. These regions of interest are used to select events that include certain predefined features (for the analysis detailed in this thesis, muons and deposits in the electromagnetic calorimeter). The L1 trigger system has a decision time of approximately 2.5 µs and reduces the rate of events from 40 MHz to 100 kHz.

An event that is accepted by the L1 trigger is then sent to the HLT, which uses

more sophisticated software algorithms. The HLT uses a more complete reconstruction of information from the whole detector to reduce the rate of events to approximately 1 kHz. Like for the L1 triggers, the analysis detailed in this thesis uses triggers which require muons and electrons (full list in table 4.2).

3.2.7 Lepton reconstruction

The reconstruction algorithms of the ATLAS experiment are designed to identify signatures of particles such as electrons and muons as well as measure their momenta.

Track and vertex reconstruction

The inner detector is immersed in a 2 T magnetic field, which bends the paths of charged particles. The ID is used to reconstruct tracks of charged particles and using this information, the particles' p_{T} are measured. ID tracks are reconstructed by fitting tracks from all ID subdetectors using a global χ^2 fit [56].

Since there can be more than one interaction in each bunch crossing, a vertex reconstruction is used to determine which tracks come from the same vertex. An adaptive vertex fitter [56, 57] is used to find vertices one by one until all tracks are associated with at least one vertex (with a fake vertex rate of less than 1 % under most pileup conditions). The sum of p_{T}^2 of all tracks belonging to each vertex is summed up, and the vertex that has the highest $\sum p_{\mathrm{T}}^2$ is considered the hard primary vertex.

The variables z_0 and d_0 are the longitudinal and transverse impact parameters of a track, respectively. The d_0 parameter is calculated with respect to the LHC beam line and z_0 with respect to the hard primary vertex of the interaction [58].

Electrons

Electron reconstruction happens in three reconstruction steps, followed by an identification step [59], as detailed below.

The first step is cluster reconstruction. The electromagnetic calorimeter is divided into $\Delta\eta \times \Delta\phi$ regions of 0.025×0.025 and a sliding window technique using 3×5 of these regions is used to identify electron cluster candidates.

The second step is track cluster association, in which the tracks from the Inner Detector are extrapolated to the calorimeter and matched to a cluster if the η and ϕ

separation between the track and the centre of the cluster is less than 0.05 and 0.1, respectively.

Finally, in the electron candidate reconstruction, the energy of the electron is measured as a sum of

- the energy deposited in the electromagnetic calorimeter, measured in 3×7 and 5×5 calorimeter regions in the barrel and end cap, respectively (this contribution is corrected for energy deposited in the presampler),
- the estimated energy deposited in material before the particle reaches the calorimeter,
- the lateral leakage, which is an estimate of the amount of energy that falls outside of the 3×7 or 5×5 unit block,
- the longitudinal leakage, which is an estimate of how much energy escapes the calorimeter.

The main contributions to the electron p_{T} resolution are a noise term, a sampling term (both contributing mostly at low p_{T}) and a constant term (due to the inherent resolution of the detector) [60]. The relative uncertainty of the measured electron energy can be seen in fig. 3.5.

Once electron candidates have been reconstructed, a number of observables are used to estimate the likelihood of an object to be an electron. The baseline electrons in the analysis in this thesis use a `Loose` electron identification working point, fully described in Ref. [59]. It uses shower-shape variables and information from the hadronic calorimeter to reject electron candidates that are more likely to be the result of hadrons or photons than electrons. In particular, it requires the track of the electron to have at least seven hits in the Pixel and SCT detectors, at least one of which has to be in the Pixel detector. The `Loose` likelihood efficiency can be seen in fig. 3.6.

For the purposes of background estimation, a `very very Loose` electron identification was created. This identification uses only the Pixel and SCT requirements from the `Loose` selection (at least seven hits in Pixel and SCT, at least one in Pixel).

Electrons outside the $|\eta| < 2.47$ region are not used in this thesis but electrons in the crack region are.

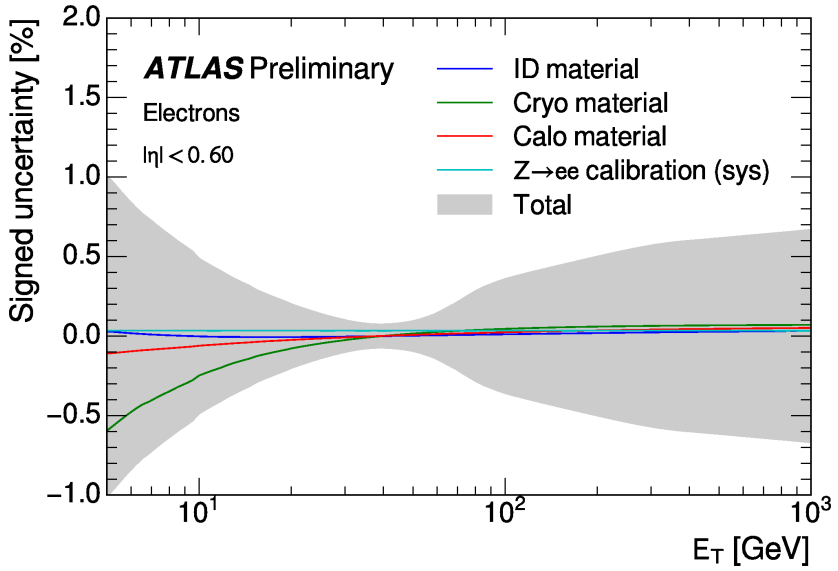

Figure 3.5: An error band representing the relative uncertainty on electron energy as a function of electron energy (for electrons with $|\eta| < 0.6$). Some contributions to the uncertainty are shown, in particular to the uncertainty from the material of various parts of the detector. Plot taken from [60].

Muons

In ATLAS, muons are reconstructed [61] using a number of methods detailed below.

Tracks through the MS are built, first in separate segments of the MDT or CSC (also using information from nearby RPC and TGC chambers), then by combining segment tracks from different layers of the MDT and finally using a χ^2 fit using all hits found associated with a track.

Four kinds of muons are reconstructed:

- Combined muons are reconstructed by extrapolating the MS track to the Inner Detector, matching it to an Inner Detector track and then repeating the fit, using hits from both the ID and MS tracks.

- Segment tagged muons are muons that have an ID track, but whose trajectory is only in one MDT segment. Typically, this is because the track is on the edge of the acceptance or its p_{T} is too low to reach outer MDT segments.

- Calorimeter-tagged (`CaloTagged`) muons are muons reconstructed from an Inner Detector track and a calorimeter deposit consistent with a muon. The reconstruc-

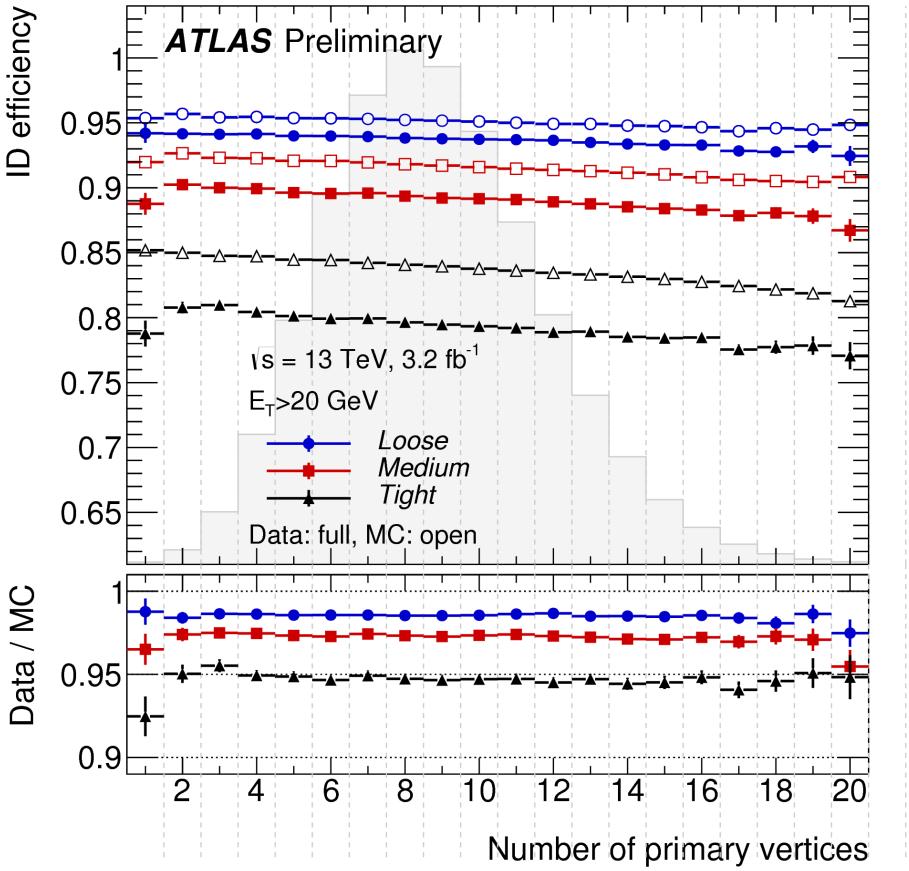

Figure 3.6: Electron ID efficiency for different working points (`Loose` being used in this thesis) as a function of the number of reconstructed vertices, estimated in $Z \to ee$ events in data and MC ($\sqrt{s}$ =13 TeV). This plot only shows electrons with p_{T} greater than 20 GeV. The gray histogram is the distribution of $Z \to ee$ events over the number of reconstructed vertices (in $\sqrt{s}$ =13 TeV). Plot taken in its entirety from [59].

tion of these muons is optimised to the range $|\eta| < 0.1$, a region in which the MS is only partially instrumented, due to cabling and services to the ID.

- Stand Alone (`StandAlone`) muons are muons that are reconstructed solely from the MS tracks. They are particularly important in the range $|\eta| > 2.7$ where the Inner Detector does not provide a track.

A `Loose` muon identification is used to differentiate muons from backgrounds (mainly muonic hadron decays). It uses the following variables:

- q/p significance. q/p is the measured ratio of charge to momentum. The significance is the absolute difference of q/p, as measured in the ID and MS, respectively, divided by the uncertainty.
- $\frac{|p_{\mathrm{T}}^{ID} - p_{\mathrm{T}}^{MS}|}{p_{\mathrm{T}}^{combined}}$, where p_{T}^{ID} is the p_{T} of the ID track, p_{T}^{MS} is the p_{T} of the MS track and $p_{\mathrm{T}}^{combined}$ is the p_{T} of the resulting combined track; and
- the normalised χ^2 of the fit of the combined track.

A plot of the `Medium` working point efficiency can be seen in fig. 3.7. It is very similar to the `Loose` working point, except in the region $|\eta| < 0.1$ (the `Loose` efficiency is shown explicitly in that range) [61].

A correction to the muon tracks due to a misalignment of the ID is also applied [62].

The main contributions to the muon p_{T} resolution are energy loss in the traversed material, multiple scattering and a constant term due to the inherent resolution of the detector [61]. An indication of the muon p_{T} uncertainty can be seen in fig. 3.8.

Lepton isolation

Both electrons and muons must satisfy two isolation requirements, in order to reject fake leptons (such as hadronic showers reconstructed as electrons) as well as leptons coming from decays of hadrons.

For a reconstructed lepton ℓ, all tracks that have a $\Delta R(\mathrm{track}, \ell) < 10\,\mathrm{GeV}/p_{\mathrm{T}}^{\ell}$ or $\Delta R(\mathrm{track}, \ell) < 0.2$ (0.3) if ℓ is an electron (muon) and which are not already associated with ℓ, are chosen, and their p_{T} are scalar summed. If that sum is more than 15 % of the p_{T} of ℓ, that ℓ is not considered to be isolated.

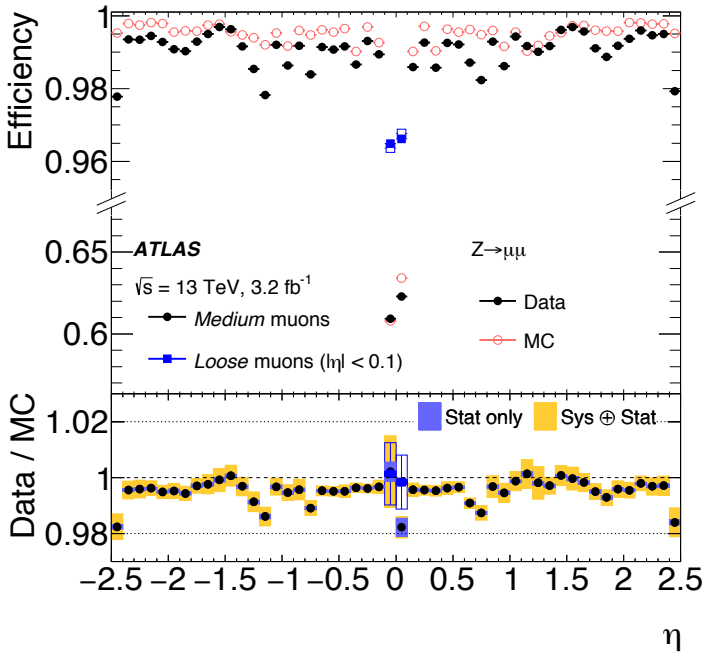

Figure 3.7: This plot shows the efficiency of the `Medium` muon identification working point in data and $Z \to \mu\mu$ MC (using a $Z \to \mu\mu$ selection and $\sqrt{s} = 13\,\text{TeV}$ data from 2015) as a function of η. The `Medium` working point is very similar to the `Loose` working point used in this thesis (so this plot can be taken to be the efficiency of the `Loose` working point), except in the region $|\eta| < 0.1$ (the `Loose` efficiency is shown explicitly in that range). The error bars on the efficiencies indicate the statistical uncertainty. The panel at the bottom shows the ratio of the measured to predicted efficiencies, with statistical and systematic uncertainties. The plot is taken from [61].

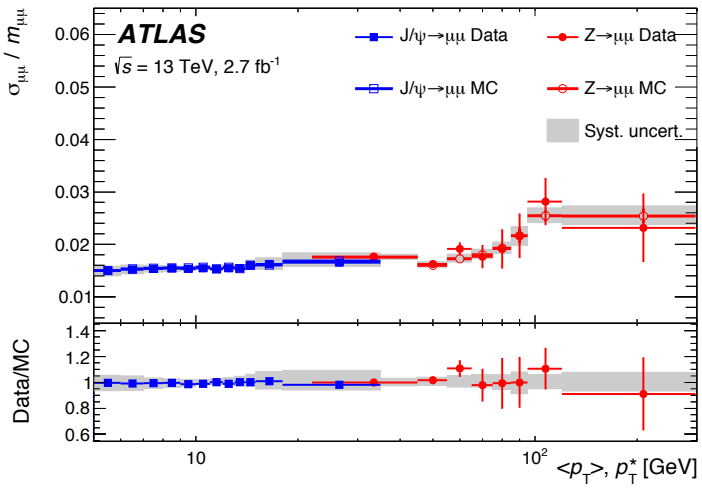

Figure 3.8: This plot shows the relative uncertainty of the invariant mass of Z and $J/\psi \to \mu\mu$ events in data and MC (using a Z and $J/\psi \to \mu\mu$ selection and $\sqrt{s} = 13\,\text{TeV}$ data from 2015) as a function of the average momentum of the muons (the $Z \to \mu\mu$ events use p^*, which is also an average, but calculated differently). The muons from each Z decay are required to be combined and fall in the same η bin (bin width of approximately $\Delta\eta = 1$). The relative uncertainty $\sigma_{\mu\mu}/m_{\mu\mu}$ is related to the muon momentum uncertainty by $\sqrt{2} * \sigma_{\mu\mu}/m_{\mu\mu} = \sigma(p_\mu)/p_\mu$. The error bars represent the statistical uncertainty while the bands show the systematic uncertainties and the plot at the bottom shows the ratio of data to prediction. The plot is taken from [61].

In addition, all energy clusters in the calorimeters (with a positive energy) with a $\Delta R(\text{cluster}, \ell) < 10\,\text{GeV}/p_{\text{T}}^{\ell}$ or $\Delta R(\text{cluster}, \ell) < 0.2$ and which are not already associated with ℓ, are chosen and their transverse energy is scalar added. If that sum is more than 20 or 30 % (for electrons and muons respectively) of the p_{T} of the lepton, that lepton is not considered to be isolated.

Together, these isolation requirements are called `FixedCutLoose`. Particle isolation is a requirement for signal electrons and muons (see chapter 4), but non-isolated leptons are used for the background estimate (see chapter 5).

3.3 Simulating the detector

After truth Monte Carlo samples have been generated (as detailed in section 2.4), the generated particles' passage through the detector (magnetic field, material interaction and particle decays) are simulated using GEANT4 [63]. Pile-up (both from the same and other bunch crossings) is simulated by overlaying randomly selected events generated by Pythia8 [64], and cavern background, beam gas interactions and beam halo can also be overlayed.

The detector response to the generated events is simulated and then passed through the ATLAS reconstruction software in the same way as data. By comparing the truth and reconstructed information in simulated data, reconstruction efficiencies can be estimated.

3.4 Chapter summary

The LHC is a particle accelerator and collider with a circumference of 26.7 km. The ATLAS detector sits on the LHC and records particle collisions. ATLAS consists of a tracking system, a calorimeter system and a muon system. Readout from the detector is limited by a trigger system which rejects events unlikely to be of interest for physics analysis.

Electrons and muons are reconstructed using tracks from the tracking and muon systems as well as calorimeter deposits. Identification and isolation criteria are also detailed.

The reconstruction process can be done on ATLAS data as well as Monte Carlo simulation, making it possible to compare data to theory predictions.

Chapter 4

Signal selection

In this chapter, the fiducial region and the selection of candidate signal events is discussed. The event selection is designed to select ZZ events in three channels: $4e$, $2e2\mu$ and 4μ. The event counts from this selection are used in chapter 7 and chapter 8 to measure the ZZ cross section and to constrain anomalous triple gauge couplings, respectively.

4.1 Fiducial region, total phase space and recorded luminosity

The cross section is measured in a fiducial region, which is a phase space chosen to closely match the detector acceptance (see chapter 3). The fiducial cross section is then extrapolated to a total cross section. The fiducial region of this analysis is defined as follows.

A ZZ event must have at least four leptons (electrons and muons), with $p_{\mathrm{T}} > 5.0\,\mathrm{GeV}$ and $|\eta| < 2.7$. Leptons coming from an interaction lose energy by emitting photons (known as *Bremsstrahlung*). To undo this effect, leptons are *dressed*, which means that when a photon (not originating from a hadron or a tau lepton) is close to a lepton, its momentum is added to its closest lepton (a photon γ is considered close to a lepton ℓ when $\Delta R(\ell, \gamma) < 0.1$).

Four of these leptons must form two separate same-flavour opposite-charge lepton pairs (Z candidates). $\sum \Delta m$ for a pair of Z candidates is defined as

$$\sum \Delta m = |m_{Z1} - m_Z| + |m_{Z2} - m_Z| \tag{4.1}$$

where m_{Z1} and m_{Z2} are the masses of the Z candidates and m_Z is the Z pole mass ($91.1876\,\mathrm{GeV}$ [9]). The pair of same-flavour, opposite-charge dileptons with the lowest $\sum \Delta m$ is called the main Z candidate pair. Both Z candidates in the main Z candidate pair must have $66\,\mathrm{GeV} < m_{Zc} < 116\,\mathrm{GeV}$ where m_{Zc} is the mass of the Z candidate.

No combination of electrons or muons can have an invariant mass of $< 5\,\mathrm{GeV}$, in order to exclude decay products of hadronic states. Every lepton ℓ in the Z candidate pair is required to have $\Delta R(\ell, \ell') > 0.1$ with every other lepton ℓ' in the Z candidate pair (this cut is introduced because leptons close to one another can have reconstruction problems).

The $4e$ and 4μ channels have cross sections similar to one another (due to lepton universality [16]) and the $2e2\mu$ (or mixed channel) has approximately twice the cross section of the unmixed channels due to combinatorics ($ZZ \to 2e2\mu$ and $ZZ \to 2\mu2e$ are both considered $2e2\mu$).

Since the Z candidates are formed with same-flavour, opposite-charge lepton pairs, $e^-e^+e^-e^+$ and $\mu^-\mu^+\mu^-\mu^+$ events have two possible ways to pair leptons for Z boson candidates, whereas $2e2\mu$ events only have one possibility (unless there are additional leptons). The interference between the two possible pairings means the fiducial cross

sections of the $4e$ and 4μ channels are greater than half the fiducial cross section of the $2e2\mu$ channel by 2.5 % (estimated in the $qq \to ZZ \to 4\ell$ and $gg \to ZZ \to 4\ell$ MC samples described in section 2.4).

The total phase space is the region of exactly two real Z bosons with masses between 66.0 GeV and 116.0 GeV, regardless of decay products or kinematic properties.

The definitions of the fiducial and total phase spaces can be seen in table 4.1.

	Fiducial	Total
Electron p_{T}	$> 5\,\mathrm{GeV}$	-
Muons p_{T}	$> 5\,\mathrm{GeV}$	-
Muons $\lvert\eta\rvert$	< 2.7	-
Electron $\lvert\eta\rvert$	< 2.7	-
Number of leptons	≥ 4	any
Same-flavour opposite-charge pairs	2	2
ZZ candidate	lowest $\sum \Delta m$	lowest $\sum \Delta m$
Lepton separation	$\Delta R(\ell, \ell') < 0.1$	-
Z mass	$66\,\mathrm{GeV} < m_Z < 116\,\mathrm{GeV}$	$66\,\mathrm{GeV} < m_Z < 116\,\mathrm{GeV}$

Table 4.1: Definition of fiducial and total region

In 2015 and 2016, the ATLAS detector has recorded a total integrated luminosity ($\int \mathcal{L}dt$) of 36.1 ± 1.1 fb^{-1} for physics-ready proton-proton collisions at 13 TeV [53]. The luminosity and uncertainty in the integrated luminosity is derived, following a methodology similar to that detailed in [39], from a preliminary calibration of the luminosity scale using x-y beam-separation scans performed in August 2015 and May 2016.

4.2 Selection overview

The signal selection is performed in four stages.

- A number of cuts are used to reject problematic events and events that are very dissimilar to the signal (initial event level cuts).
- The cuts in section 4.4.1 and section 4.4.2 are used to define the leptons in the event (object level cuts or object preselection).
- Z candidate pairs are constructed from the leptons, and a number of cuts are applied to these Z candidate pairs (known as quadruplet level cuts). The analysis

of an event continues as long as at least one Z candidate pair has passed all cuts in this stage.

- Lastly, one Z candidate pair is identified as the main Z candidate pair, and further cuts are applied to that Z candidate pair (final event level cuts). At this stage, if the main Z candidate pair fails a final event level cut, the event is rejected, even if other Z candidate pairs would have passed.

The full list of cuts can be seen in table 4.4.

The data used in this analysis is all physics-ready pp data delivered by the ATLAS detector in 2015 and 2016 with a collision centre-of-mass energy $\sqrt{s} = 13\,\text{TeV}$. The total integrated luminosity used is 36.1 fb^{-1}.

4.3 Initial event level cuts

The first cuts applied are designed to reject events that were recorded at times when the detector was not recording data properly, because of errors with ATLAS or the beam delivered by the LHC. Lists of luminosity blocks that are fit for analysis, known as Good Run Lists, are provided by ATLAS and are used to reject data taken when the beam is not suitable for physics. Cuts known as cleaning cuts are applied to reject individual events recorded when the SCT, LAr or Tile Calorimeter are not functioning normally.

Each event is required to have a primary vertex reconstructed.

4.3.1 Triggers

As described in section 3.2.6, events detected by the ATLAS detector are first sent to two layers of triggers. By using the trigger decisions, events that are very unlikely to be used in the analysis can be rejected at an early stage. The analysis described in this thesis uses 18 triggers, all unprescaled (which means every event that passes the trigger is recorded).

The full list of triggers used is found in table 4.2, chosen to maximise the efficiency. A selected event must pass at least one trigger (in a time period that they are active). Each trigger name starts with HLT, which stands for Higher Level Trigger (to differentiate it from Level 1 triggers). After that come the reconstructed particles that are required by the trigger, e for electron, mu for muon, followed by the minimum p_{T}

required (if several particles of this type are required, the number is displayed first, e.g. 2e12 means two electrons with a minimum p_{T} of 12 GeV). This is followed by any additional requirements or modifications. The words "lhvloose", "lhloose", "lhmedium" and "lhtight" describe the very loose, loose, medium and tight electron identification classification, respectively. The words "iloose" and "ivarloose" stand for loose isolation, "ivarmedium" stands for medium isolation and "nod0" means no d_0 requirement is applied. Words starting with L1 are seeded by specific L1 triggers (VH means a cut on deposits in the hadronic calorimeter applies and that the p_{T} cut is higher in some η ranges) and words including "noL1" means that object does not need to have been identified by the L1 triggers. The word "nomucomb" means that the trigger does not use combined muons (see section 3.2.7) and "nscan03" means that the muon is found within a $\Delta R < 0.3$ cone of another muon.

Combined trigger efficiencies are measured in SHERPA Monte Carlo samples to be 99.76 % for events that pass the entire signal selection.

4.4 Object selections

4.4.1 Electrons

Electrons are selected from the electrons reconstructed with the method described in section 3.2.7. Most of the cuts are applied as electron preselection, and the rest are applied as final selection, after the selection of a main Z candidate pair (this is because these cuts are inverted as a control region for the background selection, see chapter 5). Every electron in a main quadruplet of a signal selected event will pass both preselection and final selection cuts.

The electron selection criteria can be seen in table 4.3.

Electron preselection

Electrons are required to have a p_{T} of at least 7.0 GeV and $|\eta|$ of less than 2.47. They are also required to pass a very very loose electron identification, which means the SCT and Pixel requirements of the `Loose` electron described in Ref. [65].

A small number of electron clusters have readout affected by dead high voltage regions or other electronic issues. These electrons are given a bad cluster tag and removed.

Trigger	Type	Active time
HLT_e24_lhmedium_L1EM20VH	$1e$	2015
HLT_e60_lhmedium	$1e$	2015
HLT_e26_lhtight_nod0_ivarloose	$1e$	2016
HLT_e60_lhmedium_nod0	$1e$	2016
HLT_mu20_iloose	1μ	2015 + 2016 (until May 27$^{\text{th}}$)
HLT_mu24_ivarmedium	1μ	2016 (until June 21$^{\text{st}}$)
HLT_mu26_ivarmedium	1μ	2016
HLT_mu40	1μ	2015 + 2016 (until May 27$^{\text{th}}$)
HLT_mu50	1μ	2015 + 2016
HLT_2e12_lhloose_L12EM10VH	$2e$	2015
HLT_2e17_lhvloose_nod0	$2e$	2016
HLT_mu18_mu8noL1	2μ	2015
HLT_mu20_mu8noL1	2μ	2015 + 2016 (until June 21$^{\text{st}}$)
HLT_2mu10	2μ	2015 + 2016 (until May 27$^{\text{th}}$)
HLT_2mu14	2μ	2015 + 2016
HLT_mu22_mu8noL1	2μ	2015 + 2016
HLT_mu20_nomucomb_mu6noL1_nscan03	2μ	2016 (until June 21$^{\text{st}}$)
HLT_e17_lhloose_mu14	$e\mu$	2015
HLT_e17_lhloose_nod0_mu14	$e\mu$	2016
HLT_e17_lhloose_2e9_lhloose	$3e$	2015
HLT_e17_lhloose_nod0_2e9_lhloose_nod0	$3e$	2016 (until June 21$^{\text{st}}$)
HLT_3mu6	3μ	2015 + 2016

Table 4.2: List of triggers and the time during which they are active.

To reject electrons coming from pile-up or other sources, electrons are only selected if $|z_0 \sin(\theta)| < 0.5\,\text{mm}$.

If two electrons have a difference in η less than 0.075, a difference in ϕ less than 0.125 and fulfill the `Loose` criteria from [65], the electron with the lower p_{T} is rejected. Electrons that share a track with a preselected muon as described in section 4.4.2 (unless that muon is `CaloTagged`), are also removed. These two cuts are known as overlap removal.

Electrons that pass these cuts are classified as preselected.

Electron final selection

After lepton preselection is applied and a main Z candidate pair is selected, all electrons in that Z candidate pair are required to pass further cuts. These are part of the final selection cuts, which means that if the main Z candidate pair fails a cut, the event is rejected, even if there are other Z candidate pairs that could have passed.

The final selection requires electrons to pass the `Loose` selection from [65]. A cut $|d_0/\sigma_{d_0}| < 5.0$ is implicit in the `Loose` identification. In addition, electron isolation is also required, using the working point `FixedCutLoose`.

4.4.2 Muons

Muons are selected from the muons reconstructed with the method in section 3.2.7. Like in the electron selection, most cuts are applied on object level as preselection, but some (the final selection cuts) are applied only to the muons in the main Z candidate pair.

The muon selection can be seen in table 4.3.

Muon preselection

- Muons are required to have a p_{T} of at least 5.0 GeV (`CaloTagged` muons must have at least 15.0 GeV) and $|\eta|$ of less than 2.7.
- Muons have to pass a likelihood cut, using the muon quality working point `Loose` detailed in [61].
- Muons are required to have $|z_0 \sin(\theta)| < 0.5\,\mathrm{mm}$ (same as electrons), and also to have $|d_0| < 1.0\,\mathrm{mm}$ in order to reject muons from cosmic rays.
- Any `CaloTagged` muons that share a track with an electron are removed. This is known as overlap removal.

Muons that pass these cuts are classified as preselected.

Muon final selection

After the lepton preselection and main Z candidate pair selection, all muons in the main Z candidate pair have to pass an isolation cut, using the isolation working point `FixedCutLoose`, as well as a d_0 significance cut $|d_0/\sigma_{d_0}| < 3.0$.

	Preselection cuts	
	Electrons	**Muons**
Identification	very very Loose	`Loose`
p_T	$> 7.0\,\text{GeV}$	$> 5.0\,\text{GeV}$ ($> 15.0\,\text{GeV}$ for `CaloTagged` Muons)
$\lvert\eta\rvert$	< 2.47	< 2.7
Object quality	No bad cluster tag	–
$\lvert z_0 \sin(\theta)\rvert$	$< 0.5\,\text{mm}$	
$\lvert d_0\rvert$	–	$< 1\,\text{mm}$
	Overlap removal	
	Final selection cuts	
	Electrons	**Muons**
Identification	`Loose`	–
Isolation	`FixedCutLoose`	`FixedCutLoose`
$\lvert d_0/\sigma_{d_0}\rvert$	< 5.0	< 3.0

Table 4.3: Electron and muon definition cuts. The final selected cuts are applied in the final event seletion, so all leptons in signal selected events pass these cuts, even though the cuts do not happen until after the Z candidate pair selection part of the analysis.

4.4.3 Missing transverse momentum

While Z bosons decaying to neutrinos are not a part of the fiducial region of this analysis, their inferred presence is used for rejection of WZ events in the fake lepton background estimate. Therefore, the quantity used to infer their presence, the missing transverse momentum ($\mathbf{p}_T^{miss}$) is also detailed in this chapter [66].

Neutrinos only interact through the weak force and as such only very rarely interact with matter. The ATLAS detector cannot detect neutrinos directly but instead infers their presence from the topology of the event in which they are produced.

The momentum of the incoming protons in a pp interaction is well known. Protons consist of several partons (quarks and gluons) and it is not known which partons gives rise to any particular collision, nor what fraction of the proton's momentum along the z axis that parton carries. However, the partons' momentum in the x-y plane (the p_T) is known to be zero in the centre-of-mass frame. By conservation of momentum, the vector sum of the p_T of outgoing particles after a collision should also be zero. The

sum of the p_{T} can be measured, and if the detector fails to detect a particle, such as a neutrino, its momentum will not be used in the sum, which means the sum will deviate from 0. This is referred to as missing transverse momentum ($\mathbf{p}_T^{miss}$), measured as

$$\mathbf{p}_T^{miss} = -\sum \mathbf{p}_T^e - \sum \mathbf{p}_T^\mu - \sum \mathbf{p}_T^\tau - \sum \mathbf{p}_T^{jet} - \sum \mathbf{p}_T^\gamma - \sum \mathbf{p}_T^{soft} \tag{4.2}$$

i.e. the negative vector sum of the transverse momentum of all electrons, muons, taus, photons, jets (for the purposes of this analysis, AntiKt jets with a radius parameter of 0.4 were used [67]), and soft tracks, which includes any track that is not associated with a particular identified particle (typically a low p_{T} track). The exact definitions of the objects used to determine the $\mathbf{p}_T^{miss}$ are detailed in [66].

Thus it is possible to infer the presence of a neutrino or another particle not detected by the detector and its transverse momentum can be estimated to be the missing transverse momentum.

4.5 Event selection

Once electrons and muons have been preselected, events with fewer than 4 leptons are rejected. Z candidate pairs are formed by considering all possible pairs of dileptons and selecting those in which each Z candidate (dilepton) has a total charge of zero and contain leptons of the same flavour (same-flavour, opposite-charge pairs).

Z candidate pairs are rejected if they contain more than two non-`Loose` electrons (non-`Loose` electrons are only used for the fake background estimate, which only considers two fake electrons, details in chapter 5).

Three hierarchical p_{T} cuts are applied. A Z candidate pair is rejected if the highest, second highest or third highest lepton p_{T} in the Z candidate pair is less than 20 GeV, 15 GeV and 10 GeV, respectively.

Z candidate pairs with more than one `StandAlone` or `CaloTagged` muon are rejected.

Once these cuts have been made, one main Z candidate pair is selected from the Z candidate pairs that pass all cuts. To choose the Z candidate pair which is most likely to represent a ZZ event, for each Z candidate pair, the quantity $\sum \Delta m$ is calculated using eq. (4.1) and the Z candidate pair with the lowest $\sum \Delta m$ is selected as the main Z candidate pair.

Leptons that are close together risk poor reconstruction and therefore, events in which two leptons of the same flavour (both in the main Z candidate pair) have

$\Delta R(\ell\ell) < 0.1$ are rejected. Similarly, events where two leptons of different flavour (both in the main Z candidate pair) have $\Delta R(\ell\ell) < 0.2$ are rejected. This is referred to as lepton separation.

In order to reject contamination from hadronic decays (primarily $J/\psi \to \ell\ell$) a hadronic veto is introduced by rejecting events in which any two same-flavour opposite-charge leptons in the main Z candidate pair has an invariant mass of less than 5 GeV.

Then, each lepton in the main Z candidate pair is required to pass the final selection from sections 4.4.1 and 4.4.2.

Finally, a mass cut is applied. Both Z candidates in the main Z candidate pair are required to have a mass $66\,\text{GeV} < m_{Zc} < 116\,\text{GeV}$.

A summary of the signal selection can be seen in table 4.4.

Initial event level cuts	
Good Runs List	
Passes trigger	Triggers in table 4.2
Primary vertex	
Cleaning cuts	
Object preselection	See sections 4.4.1 and 4.4.2
Quadruplet level cuts	
Number of leptons in event ≥ 4	Implicit in Z candidate pair formation
Same-flavour, opposite-charge	Implicit in Z candidate pair formation
Number of vvLoose electrons	≤ 2
Hierarchical p_{T} cuts	20, 15 and 10 GeV
No more than 1 poor muon	Poor means `StandAlone` or `CaloTagged`
Select main Z candidate pair	
Final event level cuts	
Lepton separation	all $\Delta R > 0.2$ (0.1), $e\mu$ (ee, $\mu\mu$)
Hadronic veto	all $m_{\ell\ell} > 5\,\text{GeV}$
All electrons in selected Z candidate pair	`Loose`
All leptons in selected Z candidate pair	isolated
d_0 significance for all non-`StandAlone` muons	≤ 3.0
Z candidate masses	$66\,\text{GeV} < m_{Zc} < 116\,\text{GeV}$

Table 4.4: The event and Z candidate pair level cuts.

4.6 Event selection and weights in Monte Carlo

As described in section 2.4, Monte Carlo simulations of the signal events and relevant backgrounds are generated. The preselection and selection above is applied also to these events for comparison to data. The MC samples used contain $ZZ \to 4\ell$ events where ℓ is e, μ and τ. The fiducial region of this analysis considers only e and μ, and thus, events where one or both Z bosons decay to $\tau\tau$ are not counted as signal (approximately $5/9$ of the events in the sample). The MC samples contain a truth record that can be used to reject τ events (τ *cleaning*). Only events that contain at least four leptons, which are not the decay products of a τ, pass the tau cleaning and are treated as signal.

A number of weights and scale factors have to be applied to the MC samples in order for them to be comparable to data. Firstly, the MC generator gives a weight for each event. The generator weights are derived by each generator for each sample, by a function similar to eq. (2.18). As an example, the weights from the $q\bar{q} \to ZZ$ sample range from approximately -2 to 3, peaking at 1 (NLO corrections can give negative generator weights). Secondly, MC data are generated under pile-up conditions which are not consistent with data [68]. Events are reweighted so that MC reproduces the distribution of average bunch crossings in data (*pileup reweighting*). In fig. 4.1 can be seen the average number of interactions per bunch crossing in events passing the signal selection, compared to the SM prediction with and without pileup reweighting. The reweighted prediction is in better agreement with data than the unweighted prediction, most noticeably around high numbers of interactions per bunch crossing.

Lastly, differences between data and MC simulated data mean some cuts have different efficiencies in data and MC. The ATLAS Collaboration provides scale factors to correct for these differences. Each electron contributes a scale factor for reconstruction efficiency, identification and isolation [59,60,65], and each muon contributes a scale factor for reconstruction efficiency, isolation and track to vertex association [20, 61]. The scale factors from each lepton in the main Z candidate pair are multiplied together and used as a weight. The mean scale factor weight is 91 % and the standard deviation is 2.6 % (for selected events in the $q\bar{q} \to ZZ$ sample).

The weight of an event is the product of the generator weight, the pileup weight and the scale factors for all leptons in the selected quadruplet and the yield predictions are the sum of the weights of each selected event. The predictions are also normalised to the cross sections in table 2.3 and the integrated luminosity of 36.1 fb^{-1}. The predictions are subject to a number of uncertainties. The uncertainties and how they are estimated

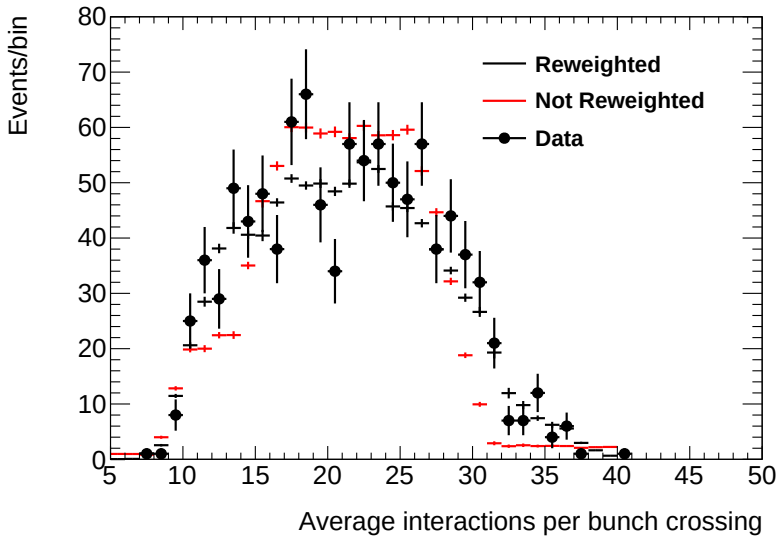

Figure 4.1: Distribution of selected events over average number of interactions per bunch crossing. The Reweighted and Not Reweighted plots are the SM prediction with and without pileup reweighting, respectively. All SM signal processes and backgrounds (see chapter 5) are included.

are explained here:

- e/γ **resolution** is the uncertainty due to the resolution of the electron momentum. The uncertainty is determined by varying the p_{T} of the electrons to their nominal value plus or minus their resolution uncertainty (as given in [60]). This has an impact on the electron scale factors (since they are a function of the kinematic properties of the electron) as well as the selection (for instance, an electron that is nominally in the fiducial region can appear outside the fiducial region when its p_{T} has been varied).

- e/γ **scale** is the uncertainty on the electron momentum scale. The electron momentum is scaled in order for distributions in data and MC to agree and the uncertainty due to this rescaling is estimated in the same way as the e/γ resolution.

- e **ID efficiency** is the uncertainty on the efficiency of the `Loose` electron identification [59,65]. The efficiency scale factor has 31 uncertainties and the corresponding uncertainties on the yields are estimated by setting the scale factors of each electron to their nominal values plus or minus their uncertainty and estimating

the yields. The deviations of the yield from its nominal value for each uncertainty are added in quadrature.

- e **Isolation efficiency** is the uncertainty on the isolation efficiency of the electrons. The isolation scale factor has 23 uncertainties and the corresponding uncertainties on the yields are estimated by setting the scale factors for each electron to their nominal value plus or minus their uncertainties. The deviations of the yields from its nominal value for the different uncertainties are added in quadrature.

- e **reconstruction efficiency** is the uncertainty on the efficiency of the electron reconstruction [59]. The reconstruction scale factor has 27 uncertainties and the corresponding uncertainties on the yields are estimated by setting the scale factors for each electron to their nominal value plus or minus their uncertainties. The deviations of the yields from its nominal value for the different uncertainties are added in quadrature.

- **Monte Carlo samples (stat.)** is the statistical uncertainty from the MC samples, determined as $\sqrt{\sum_i w_i^2}$, where w_i is the weight of each selected event.

- μ **efficiency** is the uncertainty on the efficiency of the muon reconstruction. The muon reconstruction scale factor has an uncertainty, and the corresponding uncertainty on the yields is estimated by setting the scale factors of each muon to their nominal values plus or minus their uncertainty and estimating the yields. This uncertainty is split into a statistical and a systematic part, as well as a separate class for muons with a p_{T} less than 10 GeV.

- μ **identification** is the uncertainty on the efficiency of the `Loose` muon identification. The uncertainty on the yields is estimated by setting the scale factors to their nominal values plus or minus their uncertainty and estimating the yields. The contributions to this uncertainty arising from the Inner Detector and Muon Systems are considered separately.

- μ **isolation** is the uncertainty on the efficiency of the muon isolation. The uncertainty on the yields is estimated by setting the scale factors to their nominal values plus or minus their uncertainty and estimating the yields. This uncertainty is split into a statistical and a systematic part.

- μ **sagitta residual bias** is the uncertainty due to a correction of a misalignment in the Inner Detector [62]. A residual bias uncertainty is estimated in MC. An uncertainty labelled ρ represents the uncertainty on the weight of the ID track with respect to the MS track resulting from the correction (the weight is used when reconstructing combined muons).

- μ **scale** is the uncertainty on the muon momentum scale. The uncertainty is determined by setting the p_{T} of the muons to their nominal value plus or minus its uncertainty (as given in [61]). This has an impact on the muon scale factors (since they are a function of the kinematic properties of the muons) as well as the selection (for instance, a muon that is nominally in the fiducial region can appear outside the fiducial region when its p_{T} has been varied).

- μ **vertex assoc.** is the uncertainty due to the efficiency of the muon vertex association. The uncertainty on the yields is estimated by setting the scale factors to their nominal values plus or minus their uncertainty and estimating the yields. This uncertainty is split into a statistical and a systematic part.

- **PDF** is the uncertainty due to the parton distribution functions. The PDF set provided includes 26 parton distribution functions corresponding to uncertainties on the nominal PDF. The yields are estimated using each of the PDFs in the PDF set, and the deviations from the nominal yields are added in quadrature (separately for up and down fluctuations).

- **Pileup reweighting** is the uncertainty due to the pilup reweighting. It is determined by varying the observed-to-MC ratio distribution within its uncertainties and taking the resulting yields.

- gg **cross section** is the uncertainty due to the gg cross section. It is estimated by varying the gg cross section by $\pm$ 15 % (the uncertainty on the gg k-factor). This uncertainty comes from QCD scale variations performed in [23].

- **Luminosity** is the uncertainty due to the integrated luminosity. It is taken from [53], where it is derived using a method similar to that of [39]. It is 3.1 % and is applied uniformly over all events.

The resulting uncertainties are added in quadrature and shown in table 4.5.

4.7 Results

The observed number of selected events in data can be found in table 4.5. The table also includes the number of expected selected events, estimated in the SHERPA samples described in section 2.4. Since backgrounds are not included, the expected signal events are not expected to add up to the observed number of events. This information, together with background information is repeated in chapter 6, along with distributions over some observables.

	$4e$	$2e2\mu$	4μ	total
Data	249	465	303	1017
$q\bar{q} \to ZZ$	$173.0 \pm 1.6\ ^{+6.6}_{-6.5}$	$402.4 \pm 2.3\ ^{+20.3}_{-20.2}$	$238.7 \pm 1.8\ ^{+20.5}_{-20.0}$	$814.1 \pm 5.7\ ^{+43.8}_{-43.2}$
$gg \to ZZ$	$21.2 \pm 0.3\ ^{+0.8}_{-0.8}$	$49.8 \pm 0.4\ ^{+2.6}_{-2.6}$	$30.1 \pm 0.3\ ^{+2.7}_{-2.7}$	$101.1 \pm 0.9\ ^{+5.7}_{-5.6}$
$pp \to ZZqq$	$1.7 \pm 0.1\ ^{+0.1}_{-0.1}$	$3.9 \pm 0.2\ ^{+0.2}_{-0.2}$	$2.5 \pm 0.1\ ^{+0.3}_{-0.3}$	$8.1 \pm 0.5\ ^{+0.5}_{-0.5}$
Total signal	$195.9 \pm 1.6\ ^{+6.6}_{-6.5}$	$456.1 \pm 2.3\ ^{+20.5}_{-20.4}$	$271.3 \pm 1.8\ ^{+20.7}_{-20.2}$	$923.3 \pm 5.8\ ^{+44.2}_{-43.6}$

Table 4.5: Number of selected events in the different channels as observed in data and estimated in MC. Since backgrounds are not included in this table, the MC signal yields are not expected to add up to the observed signal yields. Statistical and total systematic uncertainties are shown (total systematic signal uncertainties are the individual systematic uncertainties added in quadrature).

Chapter 5

Backgrounds

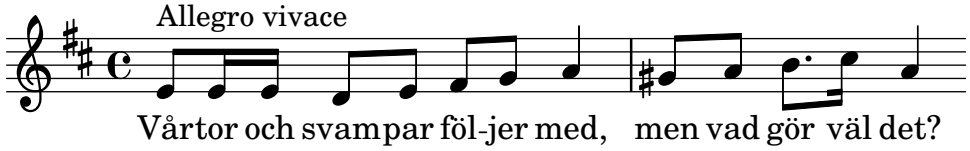

— K-LTH, *Sångarstriden, 1985*

The backgrounds to the $ZZ \to 4\ell$ process come in two categories, *irreducible* and *fake lepton* backgrounds. Irreducible backgrounds are backgrounds that include four leptons directly from the hard interaction, but which are not signal events. These backgrounds are estimated using MC samples. Fake lepton backgrounds are events where one or two reconstructed leptons are caused by non-leptons (or leptons not directly from the hard interaction). Fake backgrounds are estimated with a data-driven method.

5.1 Irreducible backgrounds

The processes that give rise to irreducible backgrounds contain leptonically decaying gauge bosons, which are for the purposes of the analysis in this thesis well modelled in Monte Carlo. The processes considered are $t\bar{t}Z$ (where both top quarks decay leptonically), WWZ, $ZZZ \to 4\ell 2\nu$ and $ZZZ \to 6\ell$. Monte Carlo samples were generated (detailed in table 5.1), and the ATLAS detector response was simulated (detailed in section 2.4).

All irreducible backgrounds are generated using Sherpa, except $t\bar{t}Z$ which is generated using MadGraph [69]. The $ZZ \to 2\tau 2\ell, 4\tau$ sample is the same sample as the signal $qq \to ZZ$ sample, but the τ cleaning is inverted. The numbers presented in this section are normalised to 36.1 fb^{-1} and a 3.1 % luminosity uncertainty is used. A 30 % uncertainty on the normalisation of each irreducible background is taken as the combined uncertainty on cross sections and reconstruction efficiencies. This is the recommended uncertainty for $t\bar{t}Z$ [70] and a conservative estimate for the gauge boson processes.

Process	generator	PDF	Cross section	Ref.
$ZZ \to 2\tau 2\ell, 4\tau$	Sherpa 2.2.1	CT10	6.50 pb	[21]
$ZZZ \to 6\ell$	Sherpa 2.1	CT10	17.06 ab	
$ZZZ \to 4\ell 2\nu$	Sherpa 2.1	CT10	441.3 ab	
$WWZ \to 4\ell 2\nu$	Sherpa 2.1	CT10	1.73 fb	
$t\bar{t}Z \to 4\ell 2\nu 2b$	MadGraph	NNPDF23LO	30.63 fb	[69]

Table 5.1: Details of MC sample used to determine the irreducible backgrounds. The cross sections were calculated by the generators for the entire sample (not just for events passing the selection cuts).

The results of applying the signal selection to these samples can be seen in table 5.7. The resulting background yields are approximately 1 % of the MC signal yields.

5.2 Data driven backgrounds

5.2.1 Overview

The background from fake leptons is the largest contribution to the backgrounds ($t\bar{t}$, WZ and $Z + X$ are expected to be the major contributions). Lepton misidentification

is not sufficiently well modelled in Monte Carlo and must be estimated with a data driven method.

A method called the Fake Factor method was chosen to determine the contribution. It works by establishing a fake background *control region* in which one or two leptons in an event fail certain lepton identification cuts. The ratio of fake leptons which pass the identification cuts to fake leptons that fail the identification cuts (the same as the ratio of fake events with four leptons which pass all cuts and events with four leptons of which, a given one fails the identification cuts) is known as the Fake Factor.

The Fake Factor is determined in data, using $Z + \ell$ events where the extra lepton is allowed to fail the identification cuts (the $Z + \ell$ region is assumed to have the same Fake Factor as the 4ℓ region.

For the purposes of this chapter, *real* leptons are defined as those coming from the decay of a gauge boson. In addition to non-leptons which have been misreconstructed as leptons, leptons coming from hadronic decays are also considered to be fake leptons.

5.2.2 Selected and inversion-tagged leptons

Leptons as selected in chapter 4 are considered *selected* leptons, whereas electrons that fail either the `Loose` identification (ID) or isolation (ISO) final cuts (final selection cuts in table 4.3), and muons that fail either the d_0 significance or isolation cuts (or both) are considered *inversion-tagged* or *i-tagged* leptons, as shown in table 5.2.

	electrons	muons
selected	Passes ID and ISO cuts	Passes d_0 significance and ISO cuts
i-tagged	Fails ID or ISO cut but not both	Fails d_0 significance or ISO cut or both

Table 5.2: Definitions of selected and i-tagged leptons.

The fake background control region is the same region as the signal region, except that the main quadruplet contains one or two i-tagged leptons instead of selected leptons. The main contribution to the fake lepton background is WZ + a fake lepton. The contribution from two real and two fake leptons, mainly from $t\bar{t}$ and WW (+ two

fake leptons) is also considered, whereas events with 3 or 4 fake leptons are assumed to be a much smaller contribution and are neglected.

The connection between real/fake (R/F) leptons and selected/i-tagged (L/J) leptons in events with four selected leptons is

$$\begin{aligned} N_{LLLL} = \; & N_{RRRR} + f_1 N_{FRRR} + f_2 N_{RFRR} + f_3 N_{RRFR} + f_4 N_{RRRF} \\ & + f_1 f_2 N_{FFRR} + f_1 f_3 N_{FRFR} + f_1 f_4 N_{FRRF} \\ & + f_2 f_3 N_{RFFR} + f_2 f_4 N_{RFRF} + f_3 f_4 N_{RRFF}, \end{aligned} \tag{5.1}$$

where N_{LLLL} is the count of reconstructed events with four selected leptons, f_n is the probability that the nth lepton (ordered descending by p_{T}), if it is a non-lepton, is reconstructed as a selected lepton and N_{RRFF} are the events with two real leptons and two fake leptons. Other combinations of R and F refer to events with that combination of real and fake leptons. The efficiency is taken to be 1 so all N_{RRRR} events contribute to N_{LLLL} (contributions to N_{LLLJ} from 4ℓ events are instead estimated in MC for a luminosity of 36.1 fb^{-1} and removed). The full dependence of any combination of selected and i-tagged leptons is

$$\begin{pmatrix} N_{LLLL} \\ N_{JLLL} \\ N_{LJLL} \\ N_{LLJL} \\ N_{LLLJ} \\ N_{JJLL} \\ N_{JLJL} \\ N_{JLLJ} \\ N_{LJJL} \\ N_{LJLJ} \\ N_{LLJJ} \end{pmatrix} = \begin{pmatrix} 1 & f_1 & f_2 & f_3 & f_4 & f_1 f_2 & f_1 f_3 & f_1 f_4 & f_2 f_3 & f_2 f_4 & f_3 f_4 \\ 0 & \bar{f}_1 & 0 & 0 & 0 & \bar{f}_1 f_2 & \bar{f}_1 f_3 & \bar{f}_1 f_4 & 0 & 0 & 0 \\ 0 & 0 & \bar{f}_2 & 0 & 0 & f_1 \bar{f}_2 & 0 & 0 & \bar{f}_2 f_3 & \bar{f}_2 f_4 & 0 \\ 0 & 0 & 0 & \bar{f}_3 & 0 & 0 & f_1 \bar{f}_3 & 0 & f_2 \bar{f}_3 & 0 & \bar{f}_3 f_4 \\ 0 & 0 & 0 & 0 & \bar{f}_4 & 0 & 0 & f_1 \bar{f}_4 & 0 & f_2 \bar{f}_4 & f_3 \bar{f}_4 \\ 0 & 0 & 0 & 0 & 0 & \bar{f}_1 \bar{f}_2 & 0 & 0 & 0 & 0 & 0 \\ 0 & 0 & 0 & 0 & 0 & 0 & \bar{f}_1 \bar{f}_3 & 0 & 0 & 0 & 0 \\ 0 & 0 & 0 & 0 & 0 & 0 & 0 & \bar{f}_1 \bar{f}_4 & 0 & 0 & 0 \\ 0 & 0 & 0 & 0 & 0 & 0 & 0 & 0 & \bar{f}_2 \bar{f}_3 & 0 & 0 \\ 0 & 0 & 0 & 0 & 0 & 0 & 0 & 0 & 0 & \bar{f}_2 \bar{f}_4 & 0 \\ 0 & 0 & 0 & 0 & 0 & 0 & 0 & 0 & 0 & 0 & \bar{f}_3 \bar{f}_4 \end{pmatrix} \begin{pmatrix} N_{RRRR} \\ N_{FRRR} \\ N_{RFRR} \\ N_{RRFR} \\ N_{RRRF} \\ N_{FFRR} \\ N_{FRFR} \\ N_{FRRF} \\ N_{RFFR} \\ N_{RFRF} \\ N_{RRFF} \end{pmatrix}, \tag{5.2}$$

where N_{LLJJ} is the number of events where the first two leptons are selected and the last two are i-tagged (any combination of L and J refers to the corresponding combination of selected and i-tagged leptons) and $\bar{f}_n$ is $1 - f_n$.

By taking the first row of this matrix equation and using the other lines to fill in

the unknown variables, N_{LLLL} is found to be

$$\begin{aligned} N_{LLLL} = N_{RRRR} \quad &+\frac{f_1}{\bar{f}_1}N_{JLLL} + \frac{f_2}{\bar{f}_2}N_{LJLL} + \frac{f_3}{\bar{f}_3}N_{LLJL} + \frac{f_4}{\bar{f}_4}N_{LLLJ} \\ &-\frac{f_1 f_2}{\bar{f}_1 \bar{f}_2}N_{JJLL} - \frac{f_1 f_3}{\bar{f}_1 \bar{f}_3}N_{JLJL} - \frac{f_1 f_4}{\bar{f}_1 \bar{f}_4}N_{JLLJ} \\ &-\frac{f_2 f_3}{\bar{f}_2 \bar{f}_3}N_{LJJL} - \frac{f_2 f_4}{\bar{f}_2 \bar{f}_4}N_{LJLJ} - \frac{f_3 f_4}{\bar{f}_3 \bar{f}_4}N_{LLJJ}. \end{aligned} \tag{5.3}$$

Since $pp \to ZZ$ events are not background even if they are only selected because of fake leptons, they are estimated in Monte Carlo and removed from the background estimate. The ratio

$$FF = \frac{f}{\bar{f}} \tag{5.4}$$

is called the *Fake Factor* (FF) and is estimated in section 5.2.3. The background part of eq. (5.3) is sometimes written in a simplified form as

$$N_{exp}^{DD} = \left(N_{LLLJ}^{\text{Data}} - N_{LLLJ}^{ZZMC}\right) FF - \left(N_{LLJJ}^{\text{Data}} - N_{LLJJ}^{ZZMC}\right) FF^2, \tag{5.5}$$

where N_{exp}^{DD} is the data driven background estimate, N_{LLLJ}^{Data} (N_{LLJJ}^{Data}) is the number of data events that would be reconstructed as signal events except one (two) leptons are i-tagged, FF is the Fake Factor, which is defined as the ratio of selected to i-tagged leptons and N_{LLLJ}^{ZZMC} (N_{LLJJ}^{ZZMC}) is the contribution to N_{LLLJ} (N_{LLJJ}) from ZZ (estimated in Monte Carlo). The application of the equation is described in more detail in section 5.2.4. This form is simplified in that it does not take into account that different leptons have different Fake Factors (the simplification is for legibility only).

5.2.3 Fake Factor

The Fake Factor (FF) is the ratio of reconstructed selected to i-tagged leptons that are not caused by real leptons. The factor is estimated in events with at least one fake lepton. The region $pp \to Z + \ell$ (where Z decays to two leptons and ℓ can be i-tagged or selected) was chosen, since it is similar to the ZZ region but has a fake lepton. Since only reconstructed leptons caused by non-leptons are to be considered, contributions from processes that give rise to three real leptons ($ZZ \to 4\ell$ using the $q\bar{q} \to 4\ell$ and

$gg \to 4\ell$ signal samples and $WZ \to 3\ell\nu$ using the sample in table 5.5) are estimated in Monte Carlo and removed from counts of both selected and i-tagged leptons. Fake Factors for electrons and muons are determined separately, and as a function of both p_{T} and η separately (because of low statistics, two one-dimensional histograms are produced and combined, instead of producing one two-dimensional histogram).

The Fake Factor is estimated in data, using dilepton triggers (14 GeV dimuon trigger, 12 and 17 GeV dielectron trigger for 2015 and 2016, respectively). Events with at least three leptons (i-tagged or selected) are selected. Two leptons must be selected, have opposite charge and same flavour, and have an invariant mass within 20 GeV of the Z pole mass and thus be considered a Z candidate. If several such pairs exist, the pair with invariant mass closest to the Z pole mass is considered the Z candidate. The event must also have a missing transverse momentum of less than 25 GeV (in order to suppress the WZ contribution). The selection of the region in which the Fake Factor is estimated can be seen in table 5.3. The masses of the Z boson candidates can be seen in fig. 5.1. Any lepton (i-tagged or selected) that is not used to reconstruct the Z candidate (*extra* lepton) is considered a fake lepton. Histograms of the extra leptons' η and p_{T} are used for the calculation of the Fake Factor and can be seen in figs. 5.2 to 5.5.

Initial event level cuts	
Good Runs List Passes trigger Primary vertex Cleaning cuts	14 GeV for 2μ, 12 (17) GeV 2015 (2016) for $2e$
Object preselection	See sections 4.4.1 and 4.4.2
Select one Z candidate from selected leptons	
Number of leptons in event ≥ 3 Same-flavour, opposite-charge 71 GeV$< m_Z <$111 GeV $\lvert\mathbf{p}_T^{miss}\rvert < 25$ GeV	selected or i-tagged Implicit in Z candidate formation
Extra leptons sorted into selected and i-tagged.	

Table 5.3: The selections and cuts for the Fake Factor region.

The Fake Factor in each bin is then calculated as

$$FF = \frac{L^{\text{Data}} - L^{ZZ,WZ}}{J^{\text{Data}} - J^{ZZ,WZ}}, \tag{5.6}$$

where FF is the Fake Factor, $L^{\text{Data}}(J^{\text{Data}})$ is the number of extra selected (i-tagged) leptons in events with a reconstructed Z boson in data and $L^{ZZ,WZ}$ ($J^{ZZ,WZ}$) is the number of extra selected (i-tagged) leptons in events with a reconstructed Z boson estimated from ZZ and WZ Monte Carlo. Fake Factors for electrons and muons are constructed separately, and plots of FF against p_{T} and η are used in the determination of the expected background. The Fake Factors can be seen in figs. 5.6 and 5.7 (with statistical uncertainties only). The bin sizes were chosen to give approximately the same yield in each bin, with the exception of the bins at $|\eta| = 1.5$, which correspond to the calorimeter crack region. The counts of selected and i-tagged electrons and muons drop off with growing p_{T} and are symmetrical in η. The plots also include an estimate for the Fake Factor from a $Z + X$ MC sample ($Z \to ee$ for the muon Fake Factor and vice versa) for purposes of the closure test (see section 5.2.5).

Figure 5.1

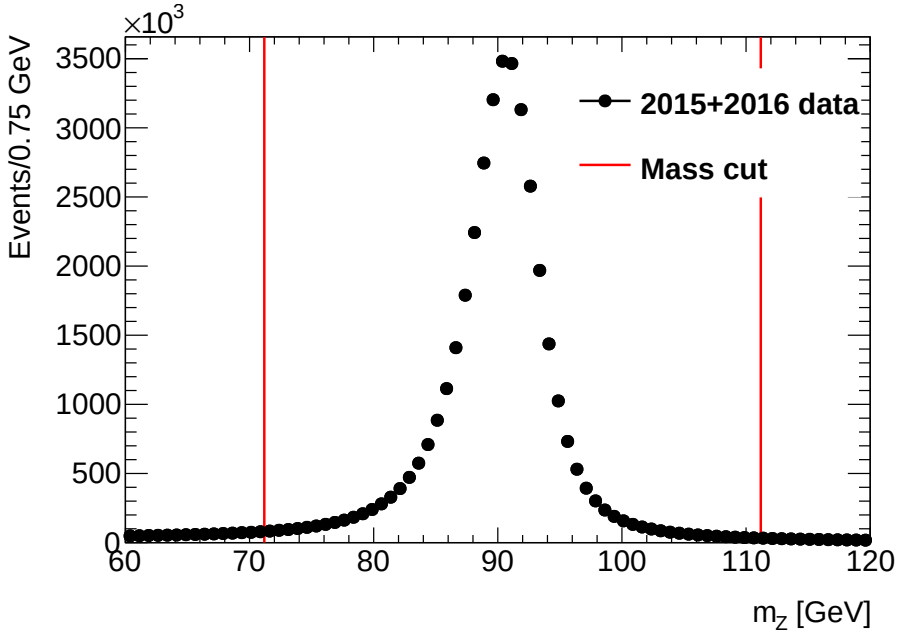

(a) The mass of all reconstructed Z candidates in data $Z + \ell$ events where ℓ can be either selected or i-tagged.

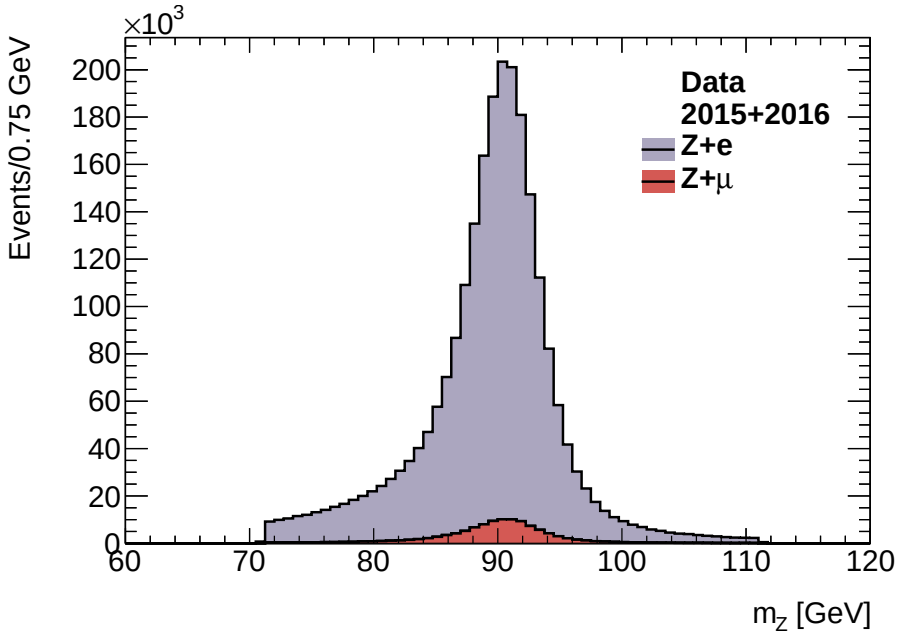

(b) The mass of reconstructed Z candidates in events that were used to estimate Fake Factors. The flavour breakdown is related to the flavour of the extra lepton, not the leptons used to construct the Z boson. The electron contribution is larger than the muon contribution since the ID cut rejects more electrons than the d_0 cut rejects muons (so inverting them gives rise to more i-tagged electrons than muons).

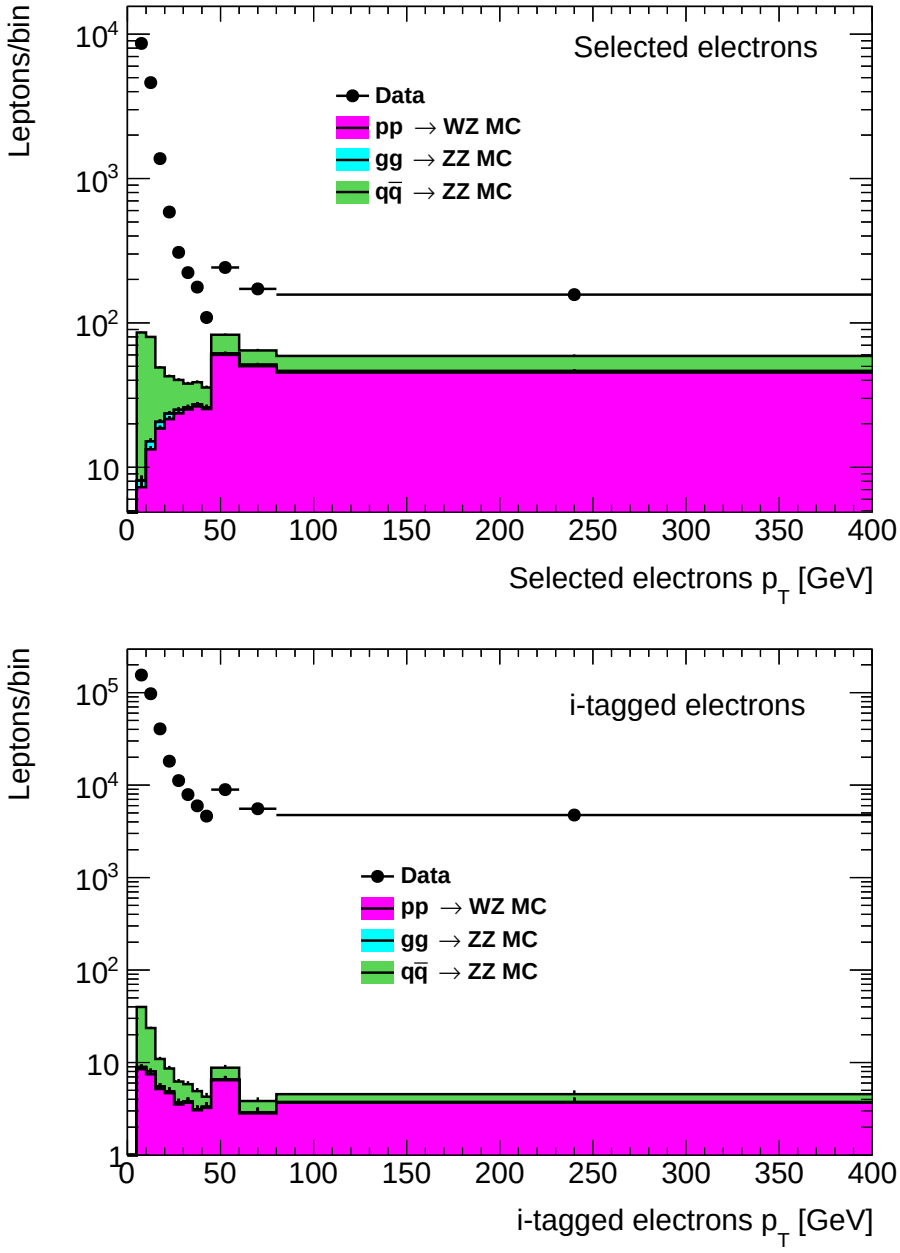

Figure 5.2: p_{T} distribution of selected and i-tagged extra electrons. Statistical uncertainty is included but generally too small to be seen. The step at 50 GeV is due to the variation in bin sizes.

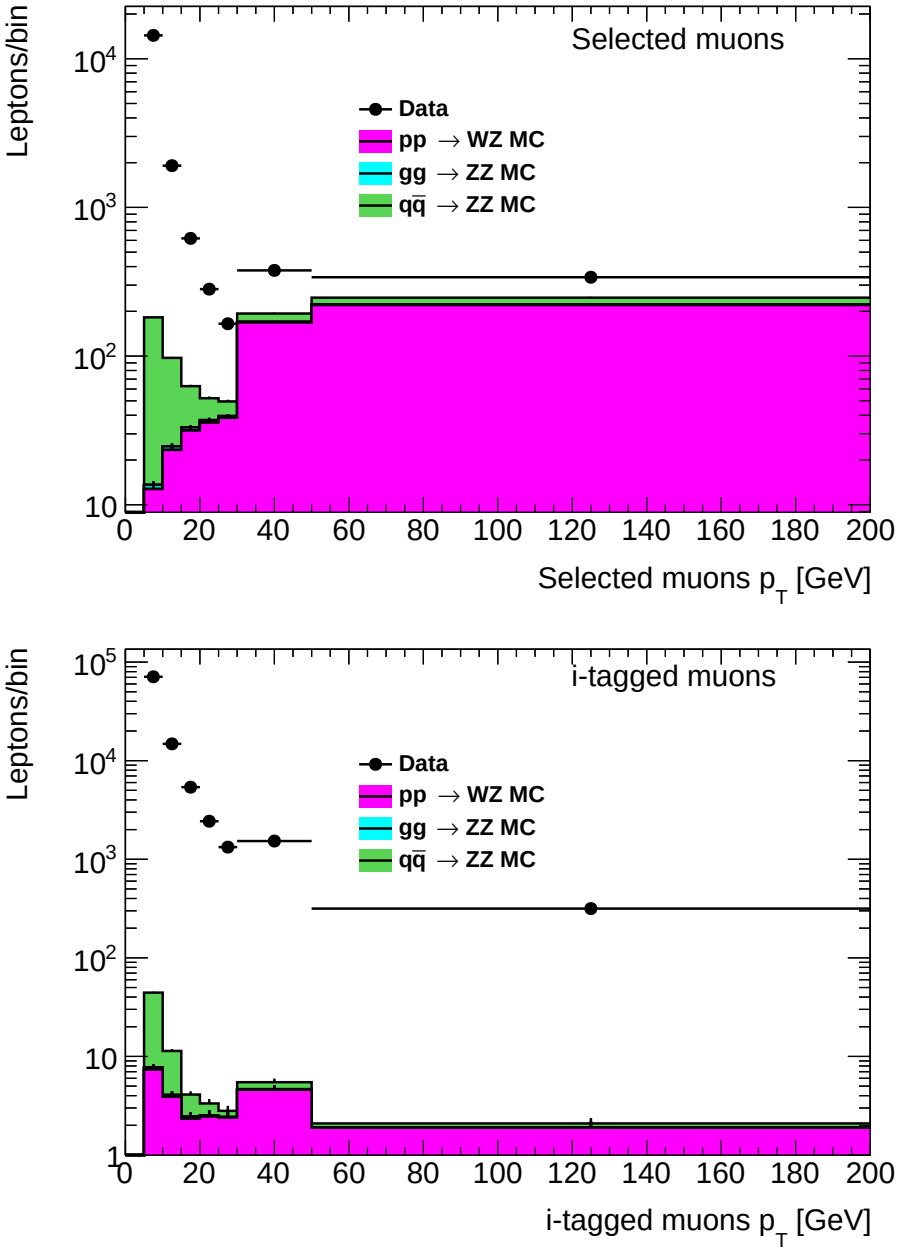

Figure 5.3: p_{T} distribution of selected and i-tagged extra muons. Statistical uncertainty is included but generally too small to be seen. The bump at 40 GeV is due to the variation in bin sizes.

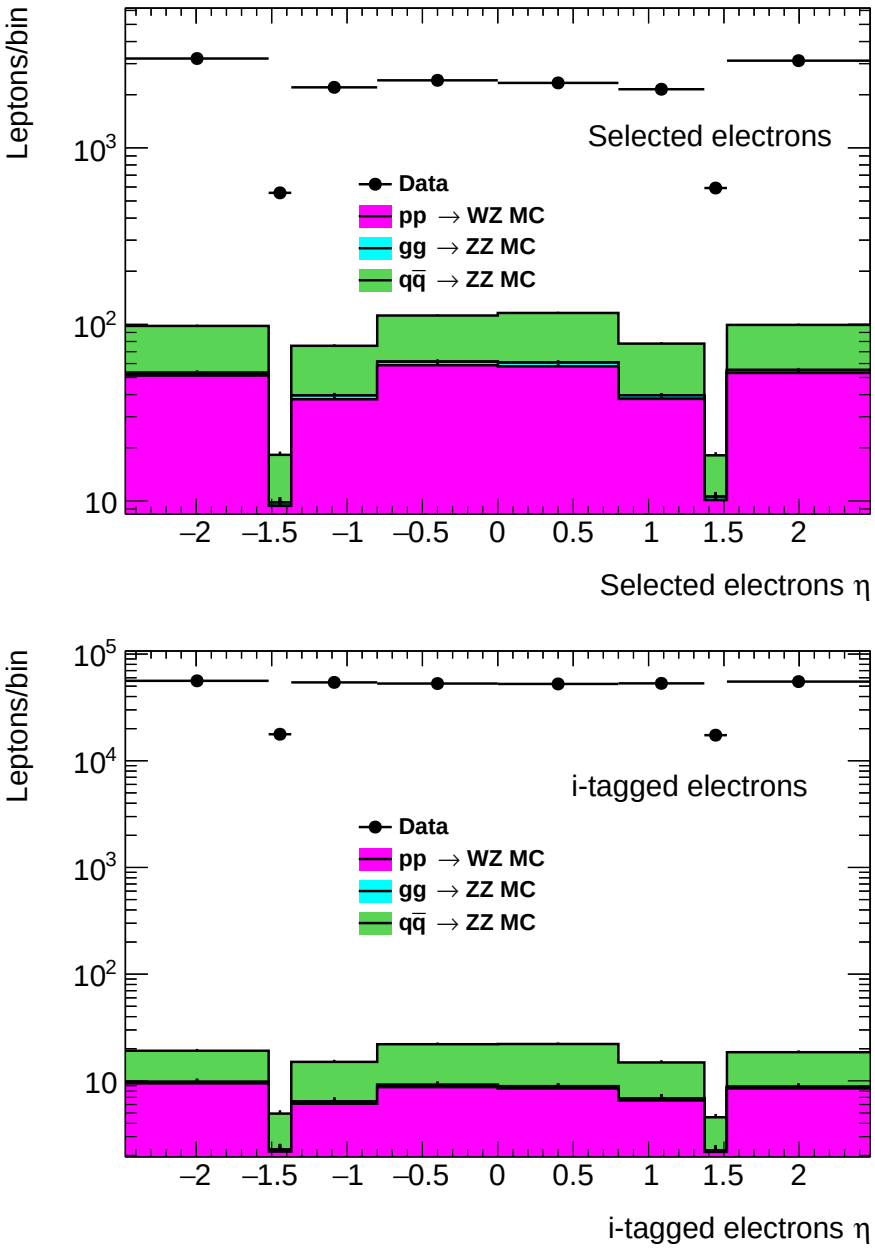

Figure 5.4: η distribution of selected and i-tagged extra electrons. Statistical uncertainty is included but generally too small to be seen. The bin at ± 1.5 covers the crack region. Its rates are low due to both the smaller reconstruction efficiency in this region and the small bin size.

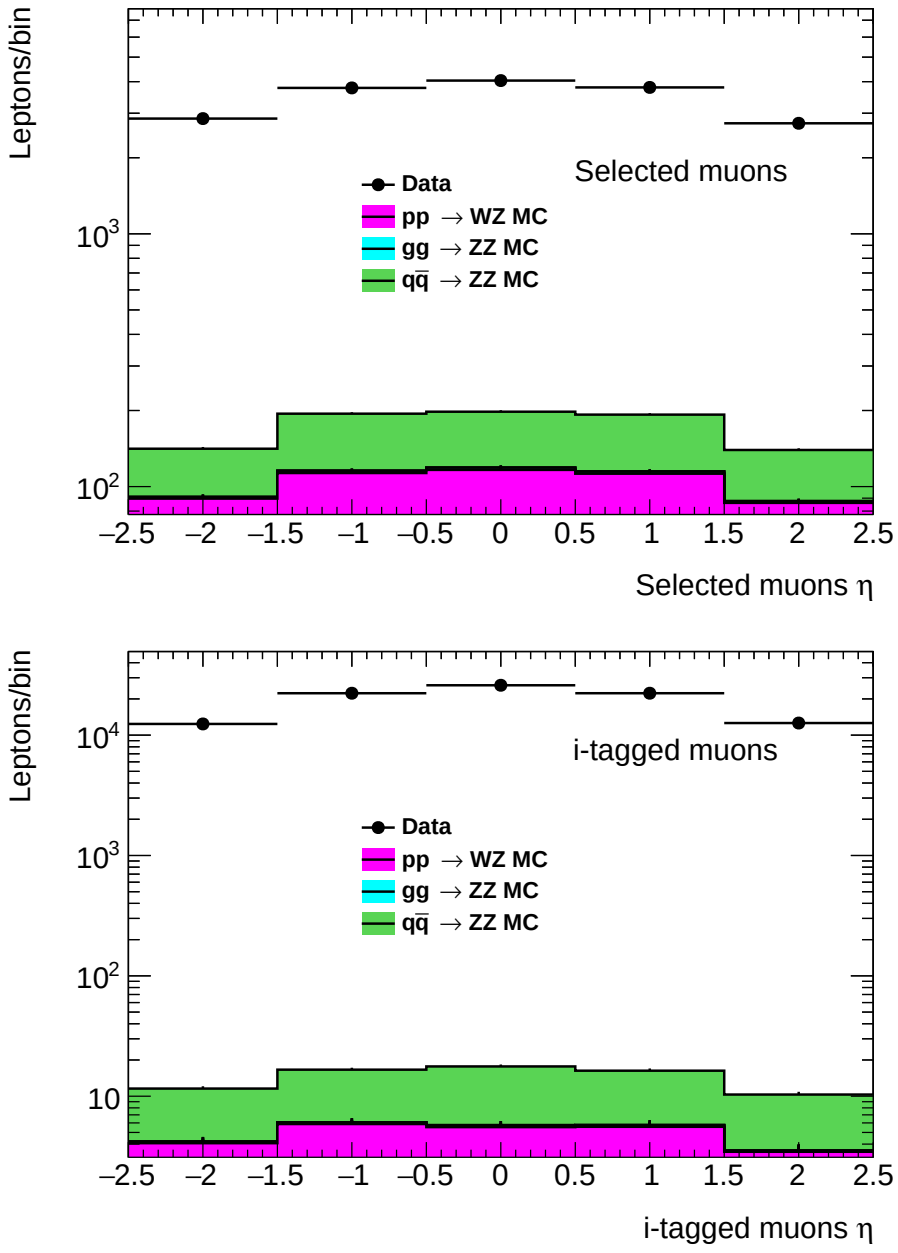

Figure 5.5: η distribution of selected and i-tagged extra muons. Statistical uncertainty is included but generally too small to be seen.

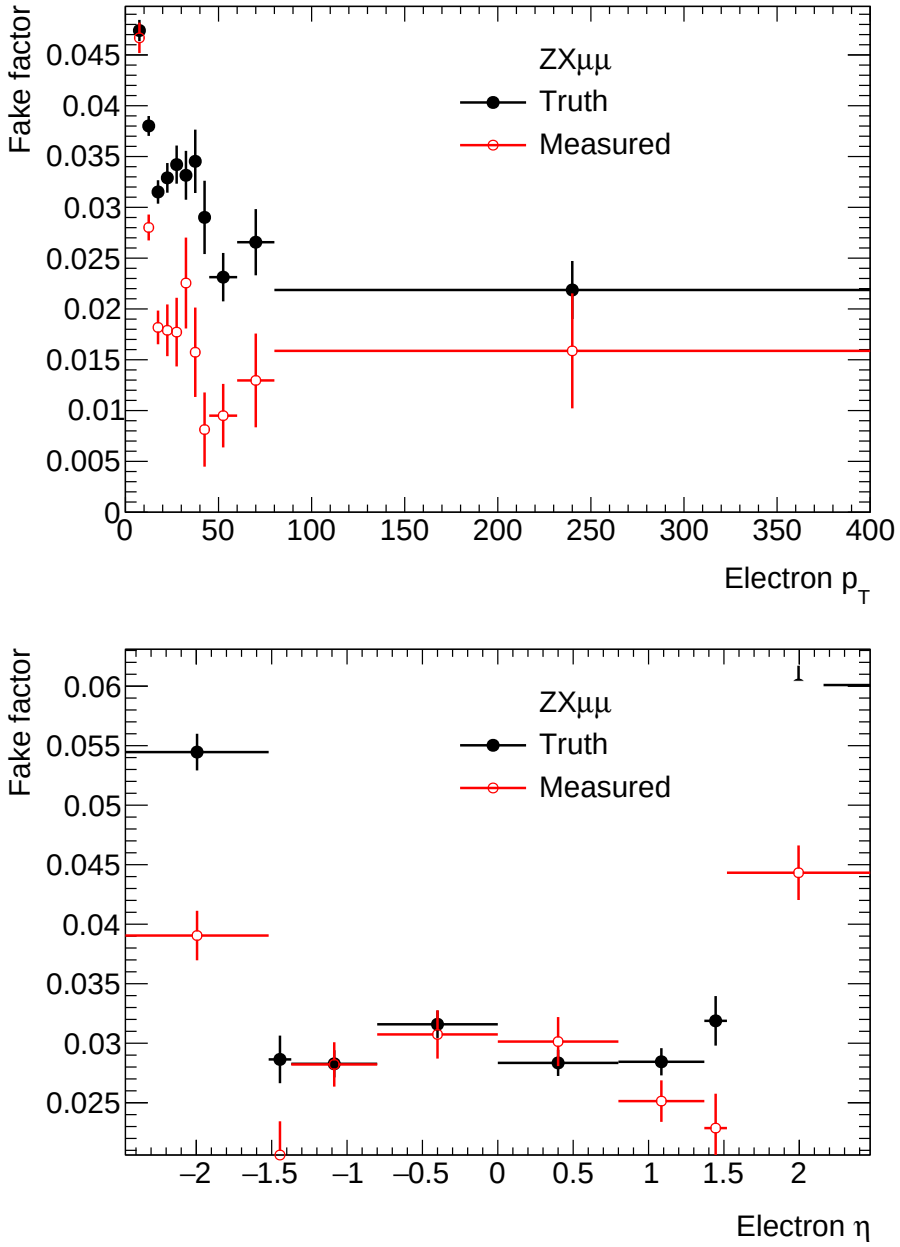

Figure 5.6: Electron Fake Factor as a function of p_{T} and η as estimated in data and a $pp \to Z + X$ MC sample (where the Z boson decays to muons, see section 5.2.5). The uncertainties are statistical.

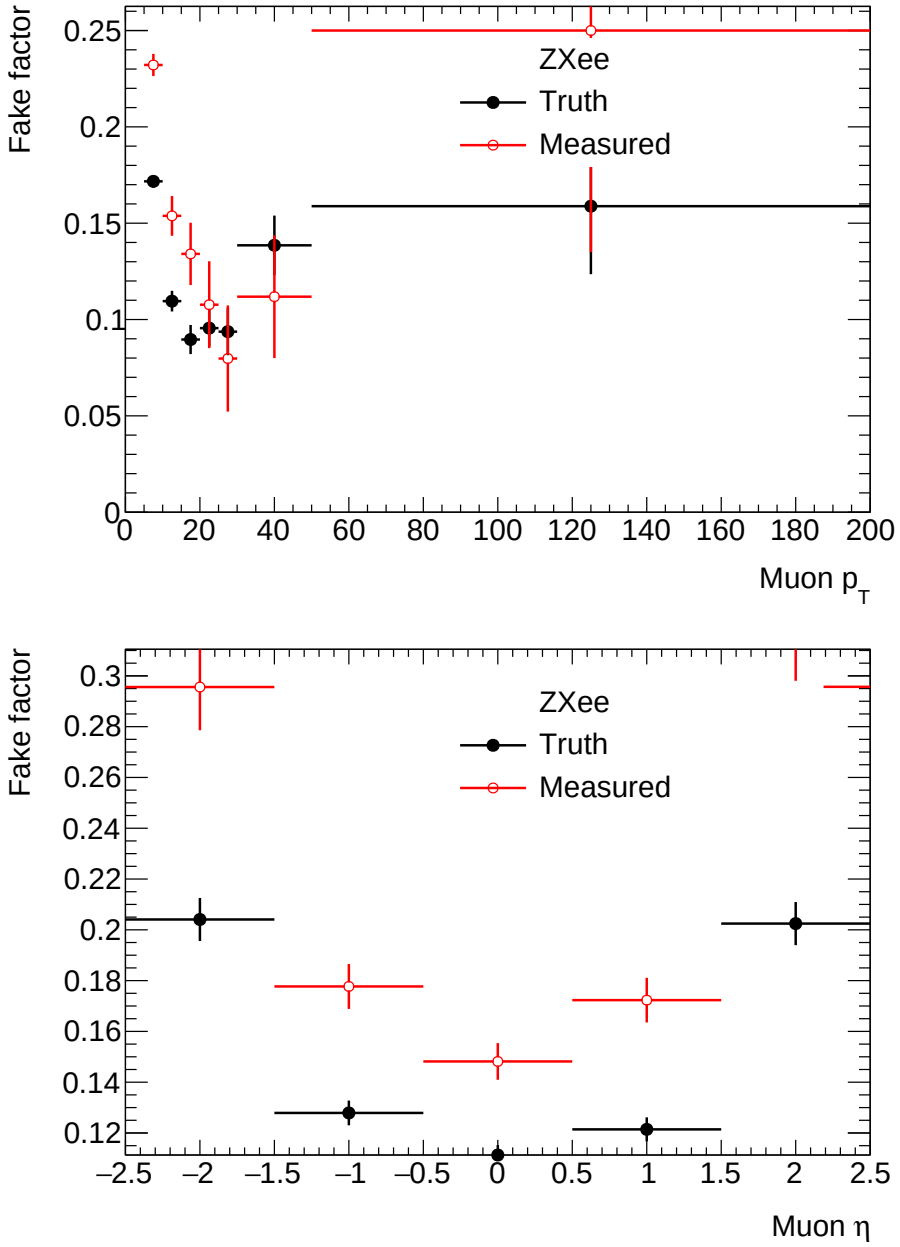

Figure 5.7: Muon Fake Factor as a function of p_{T} and η as estimated in data and a $pp \to Z + X$ MC sample (where the Z boson decays to electrons, see section 5.2.5). The uncertainties are statistical.

5.2.4 Background estimate

Once the Fake Factor is determined, events in the fake background control region are used to determine the expected background contribution to the reconstructed $ZZ \to 4\ell$ signal region. This is done by selecting events using the same selection as in chapter 4, but where the event fails because one or two leptons in the main quadruplet are i-tagged. While these events are rejected from the signal selection, they are used as the control region for the background estimate. The Fake Factor for each i-tagged lepton is taken to be the product of the Fake Factors for the η and p_{T} bins for that lepton, divided by the average of the same:

$$FF(\ell) = 2\frac{FF\left(p_{\mathrm{T}}^{\ell}\right) \times FF\left(\eta^{\ell}\right)}{FF\left(p_{\mathrm{T}}^{\ell}\right) + FF\left(\eta^{\ell}\right)}, \tag{5.7}$$

where $FF\left(\ell\right)$ is the Fake Factor of a particular lepton ℓ, $FF\left(p_{\mathrm{T}}^{\ell}\right)$ is the Fake Factor as a function of p_{T}, evaluated at the p_{T} of the lepton ℓ and $FF\left(\eta^{\ell}\right)$ is the Fake Factor as a function of η, evaluated at the η of the lepton ℓ.

The contribution from a data event in the control region to the data driven background estimate is the product of the Fake Factors of all i-tagged leptons in the 4ℓ system. Contributions to each channel are summed over all events in the control region and used as the data driven background estimate. The contribution to the control region from genuine ZZ is estimated in Monte Carlo and removed from the background estimate. A more complete form of eq. (5.5) is

$$N_{exp}^{DD} = N_{DD}^{Data} - N_{DD}^{MC\,ZZ} = \sum_{N_{LLXJ}^{\mathrm{Data}}} \prod_{\substack{\text{i-tagged} \\ \text{leptons } \ell}} FF(\ell) - \sum_{N_{LLXJ}^{MC\,ZZ}} \prod_{\substack{\text{i-tagged} \\ \text{leptons } \ell}} FF(\ell), \tag{5.8}$$

where N_{exp}^{DD} is the data driven, expected contribution from fake lepton backgrounds (and N_{DD}^{Data} and $N_{DD}^{MC\,ZZ}$ are its contributions from data and MC), N_{LLXJ}^{Data} ($N_{LLXJ}^{MC\,ZZ}$) is the number of data ($pp \to ZZ$ Monte Carlo) events which pass the signal selection except one or two leptons are i-tagged, and $FF(\ell)$ is the Fake Factor associated with a particular i-tagged lepton (as defined in eq. (5.7)).

The N_{LLXJ} with and without FF for both data and the MC subtraction, as well as the resulting background estimate can be seen in table 5.4.

	$4e$	$2e2\mu$	4μ
N_{LLLJ}^{Data}	107 ± 10	160 ± 13	77.0 ± 8.8
N_{LLJJ}^{Data}	381 ± 20	464 ± 22	154 ± 12
$FF * N_{LLLJ}^{Data}$	3.48 ± 0.35	11.10 ± 1.14	11.90 ± 1.40
$-FF^2 * N_{LLJJ}^{Data}$	−0.47 ± 0.03	−2.05 ± 0.20	−3.54 ± 0.30
N_{DD}^{Data}	3.00 ± 0.35	9.05 ± 1.16	8.36 ± 1.43
$N_{LLLJ}^{MC\,ZZ}$	48.9 ± 4.7	62.7 ± 5.1	23.7 ± 3.1
$N_{LLJJ}^{MC\,ZZ}$	6.71 ± 2.21	4.60 ± 2.27	4.19 ± 1.56
$FF * N_{LLLJ}^{MC\,ZZ}$	1.55 ± 0.15	4.59 ± 0.48	3.28 ± 0.46
$-FF^2 * N_{LLJJ}^{MC\,ZZ}$	−0.01 ± 0.00	−0.02 ± 0.01	−0.07 ± 0.03
$N_{DD}^{MC\,ZZ}$	1.55 ± 0.15	4.57 ± 0.48	3.21 ± 0.46
N_{exp}^{DD}	1.46 ± 0.38	4.49 ± 1.25	5.15 ± 1.50

Table 5.4: Input parameters for the estimation of the data driven background estimate (eq. (5.8)) for a luminosity of 36.1 fb^{-1}. The errors are the statistical uncertainty and are derived with standard error propagation. $FF * N_{LLLJ}$ is the sum of Fake Factors over events in $LLLJ$ events in the control region i.e. the contribution to N_{DD} from events with one i-tagged lepton ($-FF^2 * N_{LLJJ}$ is the same for the region with two i-tagged leptons, $LLJJ$).

5.2.5 Closure test and non-closure uncertainty

A closure test for the fake background estimate was performed, by applying the Fake Factor method to a $pp \to WZ \to \nu 3\ell$ background sample and comparing that background estimate to the expected yield obtained by applying the signal selection to the same sample. The WZ sample was chosen because it has three real leptons and only requires one fake lepton (whereas other contributions like $t\bar{t}$ and Z+hadrons require two fake leptons, which is a problem due to limited statistics).

To generate the Fake Factors for the closure test, a $pp \to Z + X$ MC sample was used, generated using Powheg [71](parton shower performed by Pythia8 [64]) and the PDF set CTEQ6 [72]. The Fake Factor extraction described in section 5.2.3 was performed on this sample (electron Fake Factors were estimated in events where the Z boson candidate was reconstructed from muons, and the muon Fake Factors were

estimated in events where the Z boson candidate was reconstructed from electrons). These Fake Factors can be seen in figs. 5.6 and 5.7. The selection for the control region was applied to a $pp \to WZ$ sample, also generated using POWHEG and CTEQ6 (details for both WZ and $Z+X$ samples can be seen in table 5.5), and the Fake Factor obtained from the $Z + X$ sample was applied. This gives an estimate of the backgrounds from the WZ process using the Fake Factor method. This estimate was compared to the background estimate obtained by running the signal selection (see chapter 4) directly on the WZ MC sample.

Process	Generator	Order	PDFs	Cross section
$pp \to 2e + X$	POWHEG [71]	NLO	CTEQ6 [72]	1.95 nb
$pp \to 2\mu + X$	POWHEG	NLO	CTEQ6	1.95 nb
$pp \to WZ$	POWHEG	NLO	CTEQ6	4.50 pb

Table 5.5: The MC samples used for the closure test, together with their generators, the order to which they have been generated, their PDFs and cross sections. All samples were normalised to a luminosity of 36.1 fb^{-1}.

The results can be seen in the last two lines of table 5.6. The estimate in the combined channel determined using the Fake Factor method is 1.93 ± 0.11 while the estimate determined using the signal selection is 0.60 ± 0.15, which is 31 % of the Fake Factor method number.

There is a disagreement between the estimate using the Fake Factor method and signal selection of up to 86 % (in the 4μ channel). To cover this non-closure, an uncertainty of 100 % is applied to the data driven background in all channels (this uncertainty covers both statistical and systematic uncertainties conservatively).

As a part of the ATLAS analysis, a number of further estimates of the systematic uncertainty were performed, including varying the MC subtraction by 50 % (up and down), using the average FF instead of histograms, using the FF obtained in MC as well as varying the FFs within their statistical uncertainties. The 100 % uncertainty covers the results from all those cross checks.

	$4e$	$2e2\mu$	4μ	Total
N^{WZ}_{LLLJ}	8.91 ± 0.57	12.98 ± 0.78	5.74 ± 0.54	27.63 ± 1.11
N^{WZ}_{LLJJ}	2.86 ± 0.34	2.99 ± 0.33	0.62 ± 0.19	6.47 ± 0.51
$FF * N^{WZ}_{LLLJ}$	0.21 ± 0.01	0.80 ± 0.07	0.95 ± 0.09	1.96 ± 0.11
$-FF^2 * N^{WZ}_{LLJJ}$	−0.00 ± 0.00	−0.01 ± 0.00	−0.02 ± 0.01	−0.03 ± 0.01
N^{WZ}_{FF}	0.20 ± 0.01	0.79 ± 0.07	0.93 ± 0.09	1.93 ± 0.11
N^{WZ}	0.16 ± 0.07	0.30 ± 0.11	0.13 ± 0.06	0.60 ± 0.15

Table 5.6: Background estimate in WZ sample, N^{WZ}_{FF} using the Fake Factor method (FF determined in $Z + X$ MC sample) and the signal selection (N^{WZ}, last line). $FF * N_{LLLJ}$ is the sum of Fake Factors over events in $LLLJ$ events in the control region i.e. the contribution to N_{DD} from events with one i-tagged lepton ($-FF^2 * N_{LLJJ}$ is the same for the region with two i-tagged lepton, $LLJJ$).

5.3 Results

The expected background event counts can be seen in table 5.7 and their distribution can be seen in figs. 5.8 to 5.12 with hatched error bands (statistical and systematic uncertainties added in quadrature).

The fluctuations of the data driven backgrounds are large due to the binning. The distributions of the data driven background are only used for distribution plots; for the cross section extraction, only the integrated background estimate is used. The aTGC studies in chapter 8 use a distribution of events over p_{T} of the Z boson with the highest p_{T}, but with a much coarser binning.

Compared to the signal predictions (see chapter 6), the backgrounds are estimated to be 1-2 % of the total yields.

5.3.1 Conclusions

Two types of background estimates are produced. An irreducible one, from MC samples, and a data driven one, representing objects that have been misidentified as leptons coming directly from a Z boson. In total, the backgrounds are expected to be 1-2 % of the total yields.

	$4e$ Nom. stat. syst.	$2e2\mu$ Nom. stat. syst.	4μ Nom. stat. syst.
$ZZ \to 4\tau, 2\tau 2\ell$	$0.61 \pm 0.09 \pm 0.18$	$0.69 \pm 0.09 \pm 0.21$	$0.58 \pm 0.08 \pm 0.17$
$t\bar{t}Z$	$0.52 \pm 0.02 \pm 0.16$	$1.19 \pm 0.04 \pm 0.36$	$0.90 \pm 0.04 \pm 0.27$
WWZ	$0.25 \pm 0.02 \pm 0.08$	$0.53 \pm 0.02 \pm 0.16$	$0.40 \pm 0.02 \pm 0.12$
$ZZZ \to 6\ell$	$0.04 \pm 0.00 \pm 0.01$	$0.10 \pm 0.00 \pm 0.03$	$0.06 \pm 0.00 \pm 0.02$
$ZZZ \to 4\ell$	$0.13 \pm 0.01 \pm 0.04$	$0.30 \pm 0.01 \pm 0.09$	$0.18 \pm 0.00 \pm 0.05$
Total irreducible	$1.5 \pm 0.1 \pm 0.5$	$2.8 \pm 0.1 \pm 0.8$	$2.1 \pm 0.1 \pm 0.6$
Data driven	$1.7 \pm 0.0 \pm 1.7$	$4.4 \pm 0.00 \pm 4.4$	$4.7 \pm 0.00 \pm 4.7$
Total backgrounds	$3.3 \pm 0.1 \pm 1.7$	$7.3 \pm 0.1 \pm 4.5$	$6.8 \pm 0.1 \pm 4.7$

Table 5.7: Number of expected background events, with statistical and systematic uncertainties. Total irreducible is the sum of the irreducible backgrounds (the systematic errors of the irreducible backgrounds are correlated and are therefore added linearly, the other uncertainties are added in quadrature). The statistical uncertainty on the data driven backgrounds are covered by the non-closure uncertainty and is therefore labelled as zero.

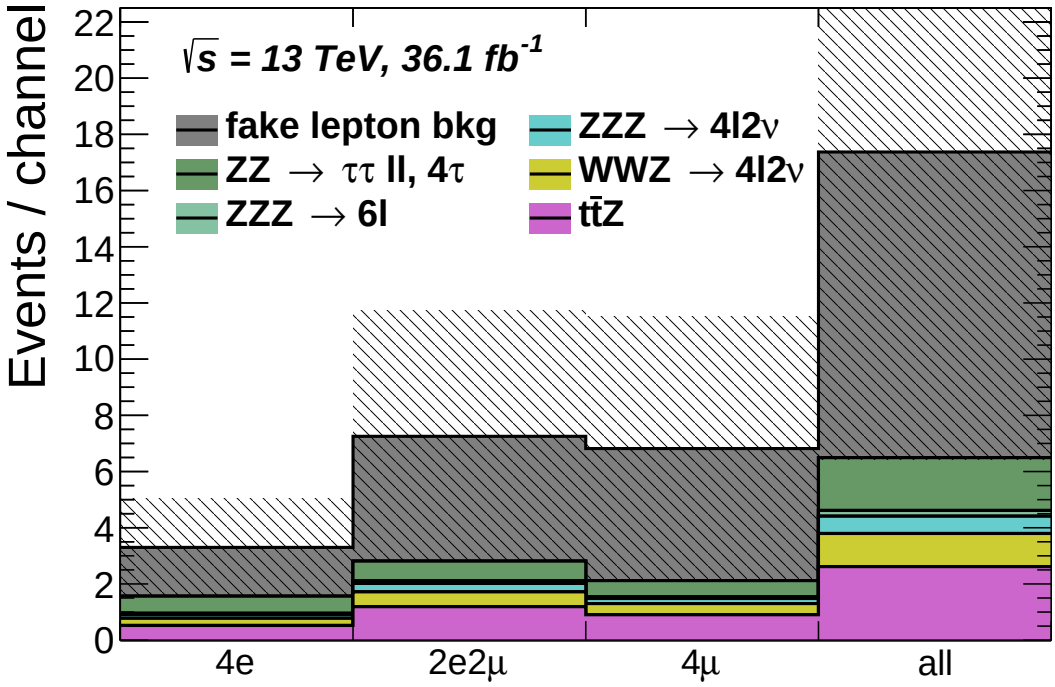

Figure 5.8: Distribution of expected background events over channels. The hatched area represents the total uncertainty.

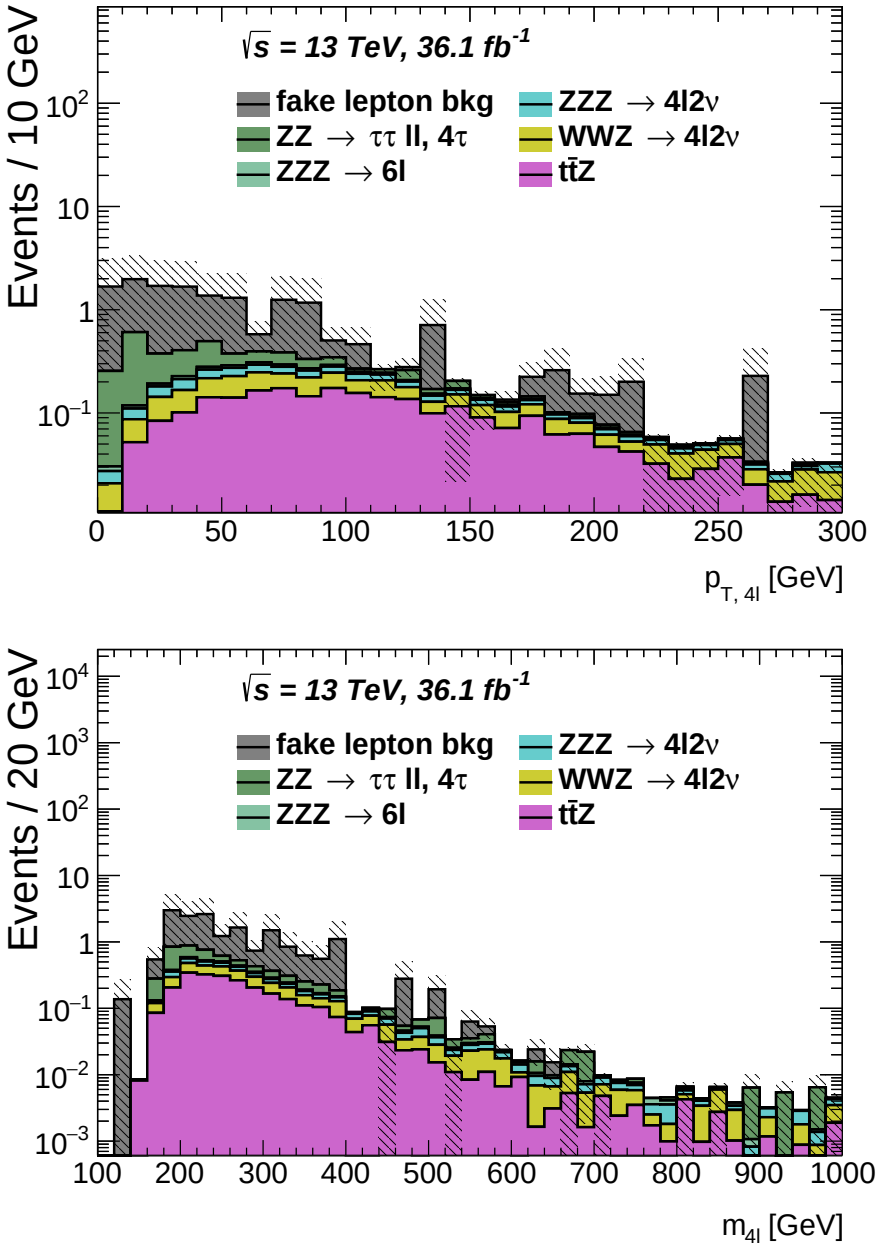

Figure 5.9: Distribution of expected background events over p_{T} and invariant mass of the 4ℓ system.

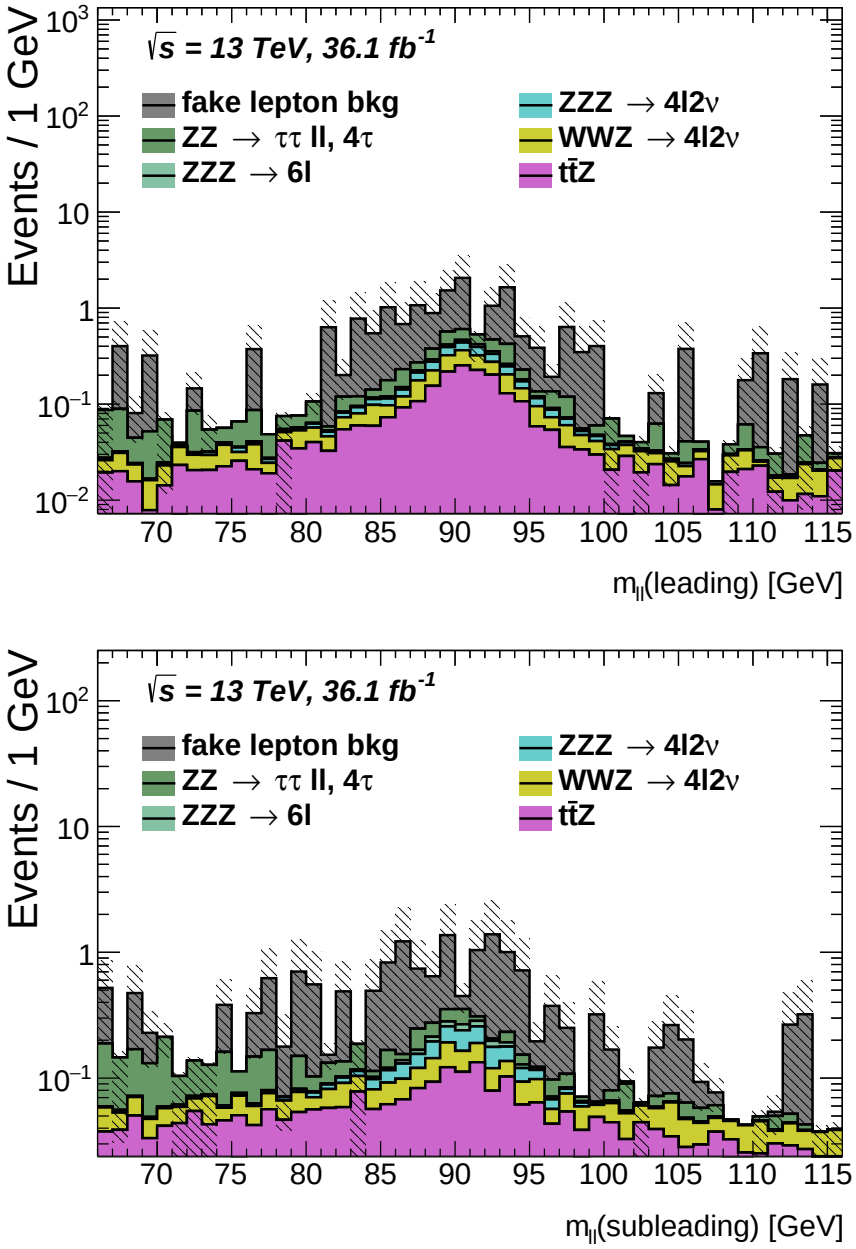

Figure 5.10: Distribution of expected background events over the mass of the leading and subleading Z boson candidate in the event. The leading Z boson candidate is defined as the selected Z boson candidate with the highest p_{T} (the subleading Z candidate is the other one). The selection of Z candidates close to the Z pole mass means that a peak around 91 GeV is expected even if the background process does not include a Z boson.

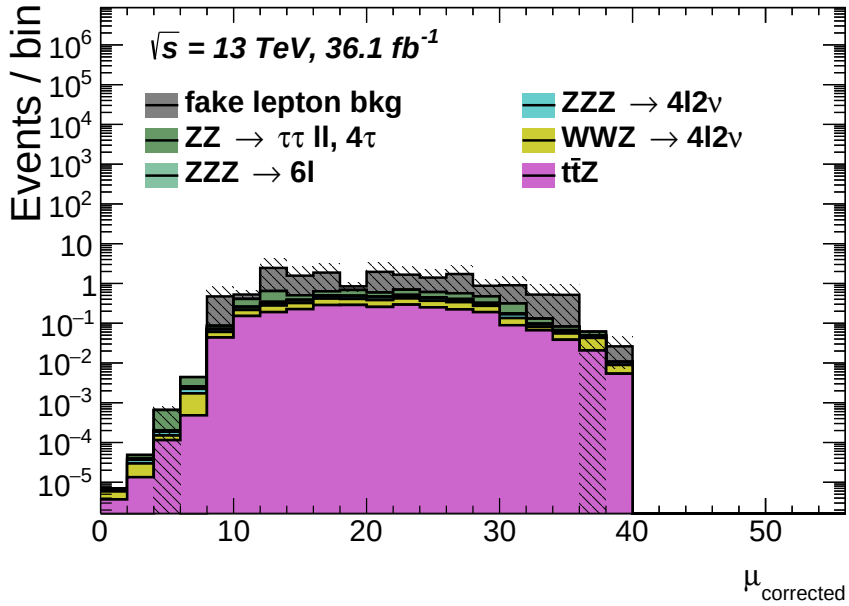

(a) Distribution of expected background events as a function of corrected average interactions per bunch crossing $\mu_{corrected}$.

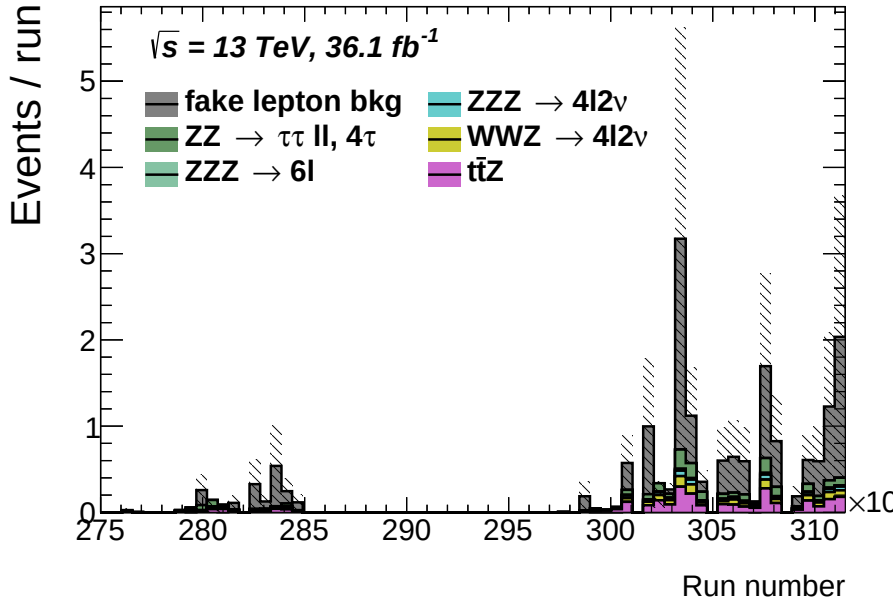

(b) Distribution of expected background events over run number. The runs are representative of the time ATLAS gathered data, which depends on machine status and performance. The gap in the middle of the graph represents a time of machine improvement between the 2015 and 2016 data taking periods.

Figure 5.11

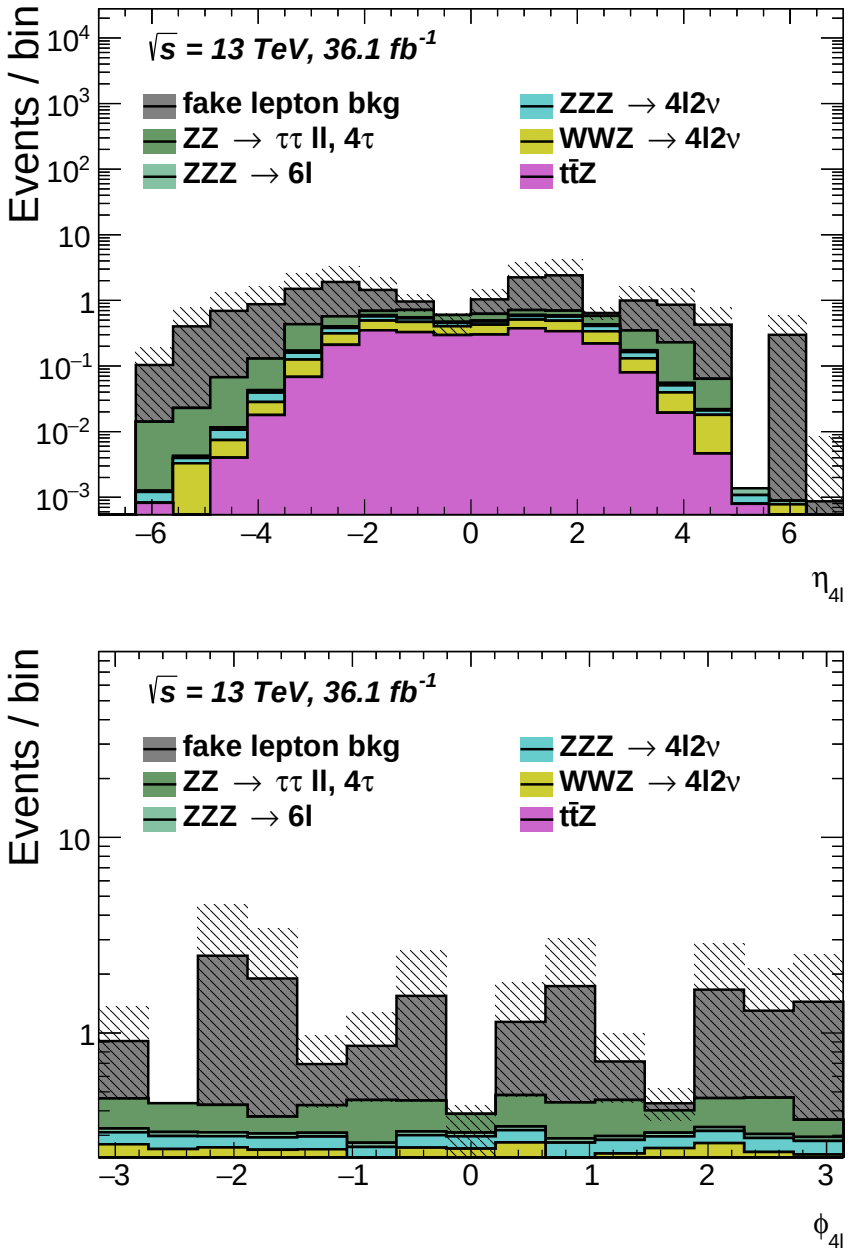

Figure 5.12: Distribution of expected background events over η and ϕ of the full 4ℓ system.

Chapter 6

Selected events

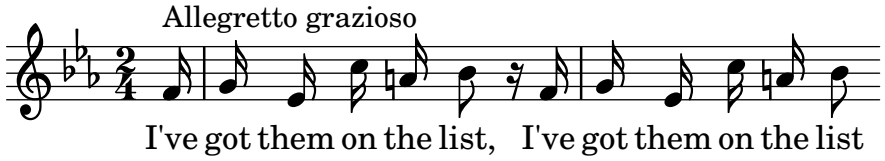

— Gilbert and Sullivan, *The Mikado, 1885*

This chapter includes tables and graphs of the data events gathered with the machinery detailed in chapter 3 and selected using the selections in chapter 4. For comparison, the expected yields for signal and background processes estimated in chapters 4 and 5 are also shown.

In table 6.1 can be seen the observed and expected yields.

Distributions of several variables can be seen in figs. 6.1 to 6.14. In the plots are shown statistical uncertainties for the data points, as well as the dominant uncertainties (statistical and luminosity) for the MC predictions (backgrounds also include the uncertainties mentioned in chapter 5). The ratio plots in the figures show $(data - MC)/\sqrt{data}$, where MC is the MC prediction, i.e. difference divided by statistical uncertainty (statistical uncertainty taken to be $\sqrt{data}$). The MC uncertainties are represented by shading.

Agreement between data and predictions is consistent with statistical fluctuations except in a few cases: An excess can be seen in the $4e$ channel in fig. 6.1 (discussed in more detail in section 6.1). Invariant mass and p_{T} of the 4ℓ system are also shown per decay channel, and the excess is visible in the $4e$ channel plots (figs. 6.3b and 6.5b).

In fig. 6.2, the dilepton mass cuts are shown, and a peak in the Z candidate invariant masses can be seen around the Z pole mass as expected. The position of the peak

	$4e$	$2e2\mu$	4μ
Data	249	465	303
$q\bar{q} \to ZZ$	$173.0 \pm 1.6\ ^{+6.6}_{-6.5}$	$402.4 \pm 2.3\ ^{+20.3}_{-20.2}$	$238.7 \pm 1.8\ ^{+20.5}_{-20.0}$
$gg \to ZZ$	$21.2 \pm 0.3\ ^{+0.8}_{-0.8}$	$49.8 \pm 0.4\ ^{+2.6}_{-2.6}$	$30.1 \pm 0.3\ ^{+2.7}_{-2.7}$
$pp \to ZZqq$	$1.7 \pm 0.1\ ^{+0.1}_{-0.1}$	$3.9 \pm 0.2\ ^{+0.2}_{-0.2}$	$2.5 \pm 0.1\ ^{+0.3}_{-0.3}$
Total signal	$195.9 \pm 1.6\ ^{+6.6}_{-6.5}$	$456.1 \pm 2.3\ ^{+20.5}_{-20.4}$	$271.3 \pm 1.8\ ^{+20.7}_{-20.2}$
$ZZ \to 4\tau, 2\tau 2\ell$	$0.61 \pm 0.09 \pm 0.18$	$0.69 \pm 0.09 \pm 0.21$	$0.58 \pm 0.08 \pm 0.17$
$t\bar{t}Z$	$0.52 \pm 0.02 \pm 0.16$	$1.19 \pm 0.04 \pm 0.36$	$0.90 \pm 0.04 \pm 0.27$
WWZ	$0.25 \pm 0.02 \pm 0.08$	$0.53 \pm 0.02 \pm 0.16$	$0.40 \pm 0.02 \pm 0.12$
$ZZZ \to 6\ell$	$0.04 \pm 0.00 \pm 0.01$	$0.10 \pm 0.00 \pm 0.03$	$0.06 \pm 0.00 \pm 0.02$
$ZZZ \to 4\ell$	$0.13 \pm 0.01 \pm 0.04$	$0.30 \pm 0.01 \pm 0.09$	$0.18 \pm 0.00 \pm 0.05$
Total irreducible	$1.5 \pm 0.1 \pm 0.5$	$2.8 \pm 0.1 \pm 0.8$	$2.1 \pm 0.1 \pm 0.6$
Data driven	$1.7 \pm 0.0 \pm 1.7$	$4.4 \pm 0.0 \pm 4.4$	$4.7 \pm 0.0 \pm 4.7$
Total backgrounds	$3.3 \pm 0.1 \pm 1.7$	$7.3 \pm 0.1 \pm 4.5$	$6.8 \pm 0.1 \pm 4.7$
Total prediction	$199.2 \pm 1.6\ ^{+6.9}_{-6.8}$	$463.3 \pm 2.3 \pm 20.9$	$278.1 \pm 1.8\ ^{+21.2}_{-20.7}$

Table 6.1: Measured and expected yields (combination of tables 4.5 and 5.7). Uncertainties are added in quadrature (except for systematic uncertainties on irreducible backgrounds, which are correlated and therefore added linearly).

indicates that the mass cuts are well placed. The invariant mass of the 4ℓ system has a lower limit of 132 GeV, as can be seen in figs. 6.5 and 6.6, due to the mass constraints on the Z candidates (132 GeV is twice the lower Z candidate mass cut 66 GeV). Figure 6.7 shows the masses of the Z candidates and clearly shows a peak at the Z pole mass of 91 GeV.

In figs. 6.8 and 6.9 can be seen the p_{T} of the leptons, ordered by p_{T}. There is a cut on all leptons on 5 GeV, which can be seen in fig. 6.9b. The leading, subleading and subsubleading leptons are required to have p_{T} higher than 20, 15 and 10 GeV, respectively. The distribution of events over η of the leptons, which can be seen fig. 6.10, decreases at high $|\eta|$, due to the topology of the detector.

Figure 6.11 shows the p_{T} of the leading and subleading Z candidates.

The distribution of events over time and average interactions per bunch crossing can be seen in fig. 6.12. A gap is visible in the middle of the time graph; it corresponds to a time of machine improvement between the 2015 and 2016 data taking periods.

The distribution of events over η and ϕ can be seen in figs. 6.13 and 6.14. The dip in the middle of the η range in both plots is due to the asymmetry in momentum carried

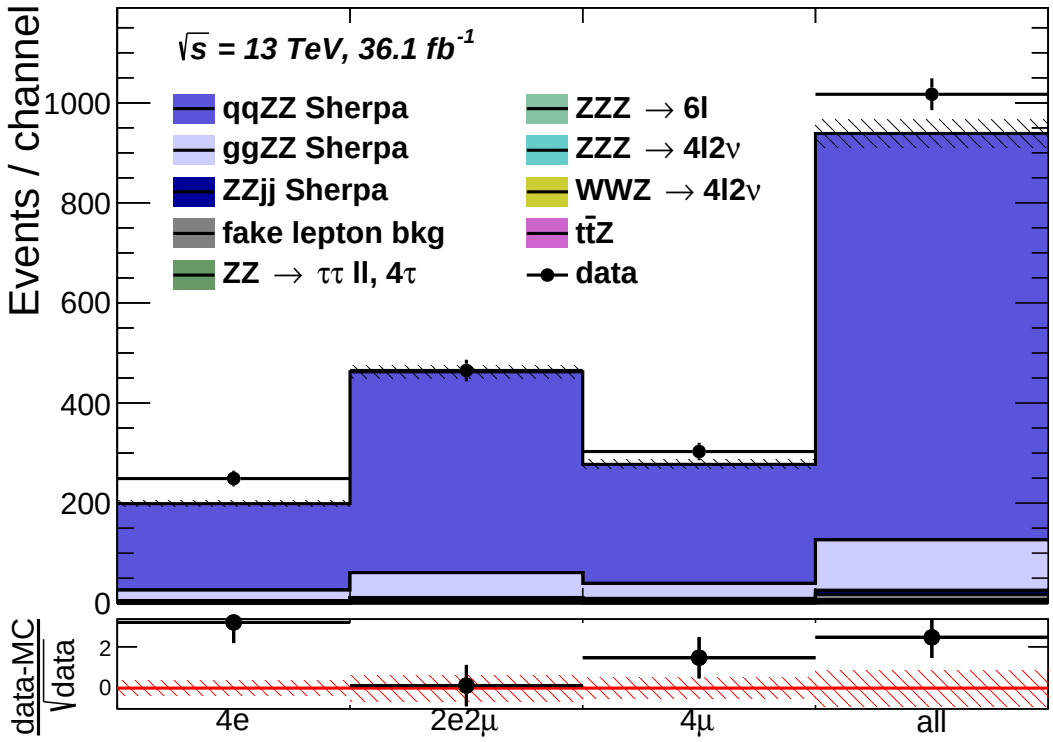

Figure 6.1: Distribution of events over channels. The error band represents the MC uncertainties.

by the quark and antiquark in the $q\bar{q} \to ZZ$ production mode. The distribution of events over ϕ is uniform due to the rotational symmetry of the detector.

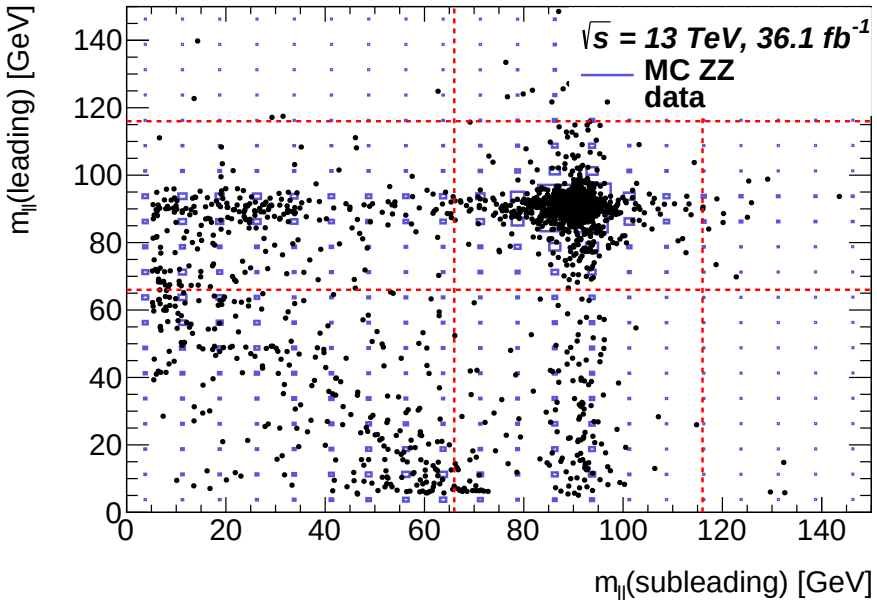

(a)

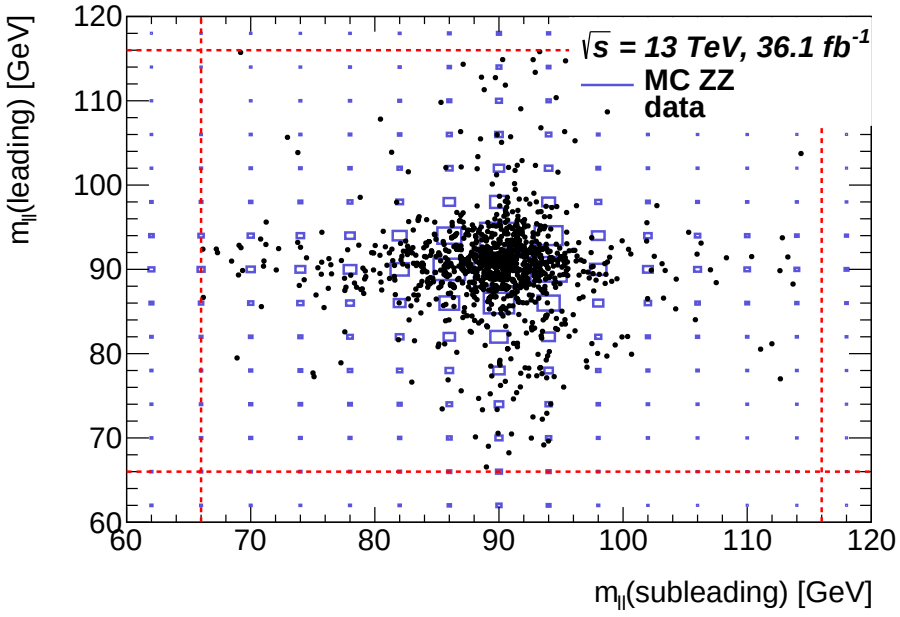

(b)

Figure 6.2: Distribution of events over leading and subleading Z candidate masses. The leading Z boson candidate is defined as the selected Z boson candidate with the highest p_{T} (the subleading Z candidate is the other one). In this plot, the mass cut on the Z candidate is not applied, but denoted by dotted lines. The signal MC prediction is shown in a box plot (box areas are proportional to number of expected events). Backgrounds are not shown. Fig. (b) is a zoomed in version of fig. (a).

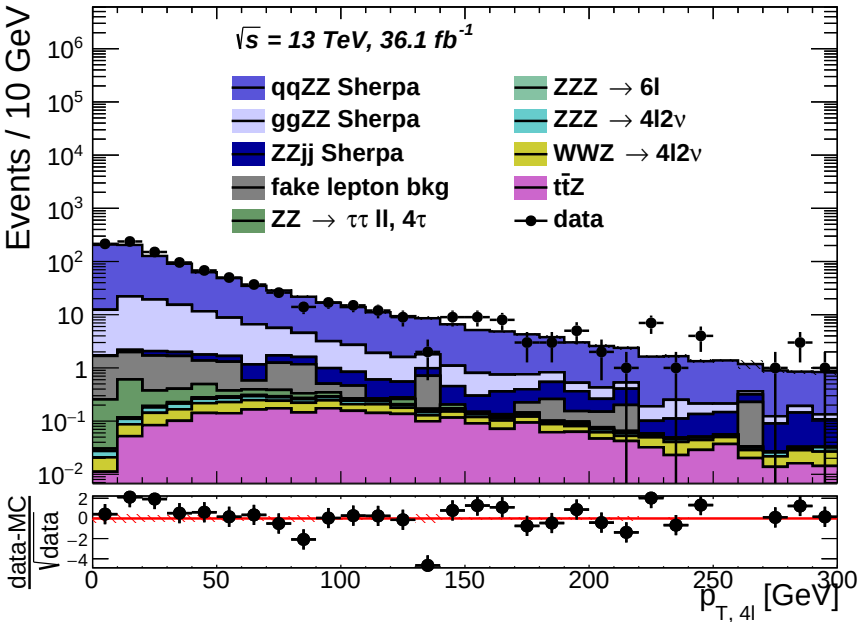

(a)

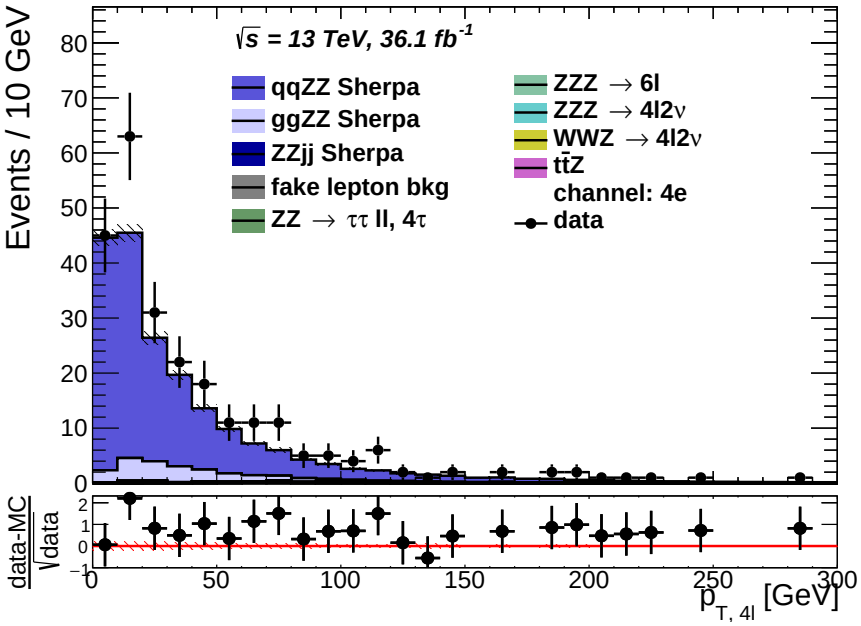

(b)

Figure 6.3: Distribution of events over p_{T} of the 4ℓ system for the combined channel as well as the $4e$ channel. The former is on a log plot in order to show the backgrounds more clearly.

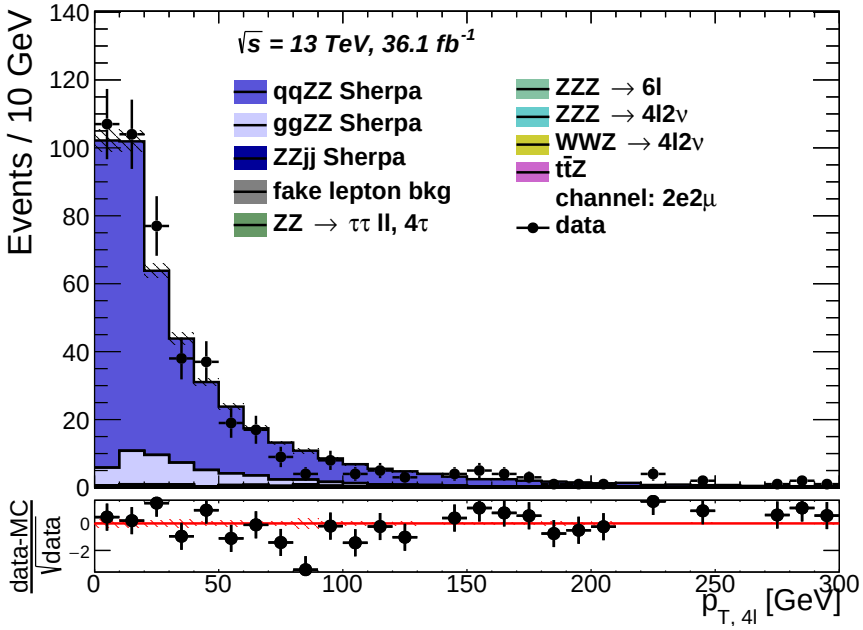

(a)

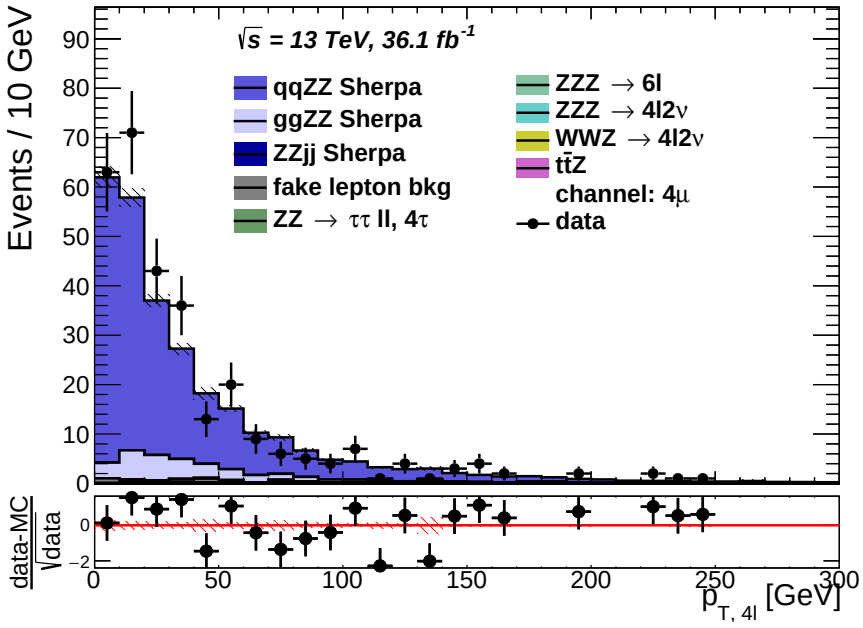

(b)

Figure 6.4: Distribution of events over p_{T} of the 4ℓ system for the $2e2\mu$ and 4μ channels.

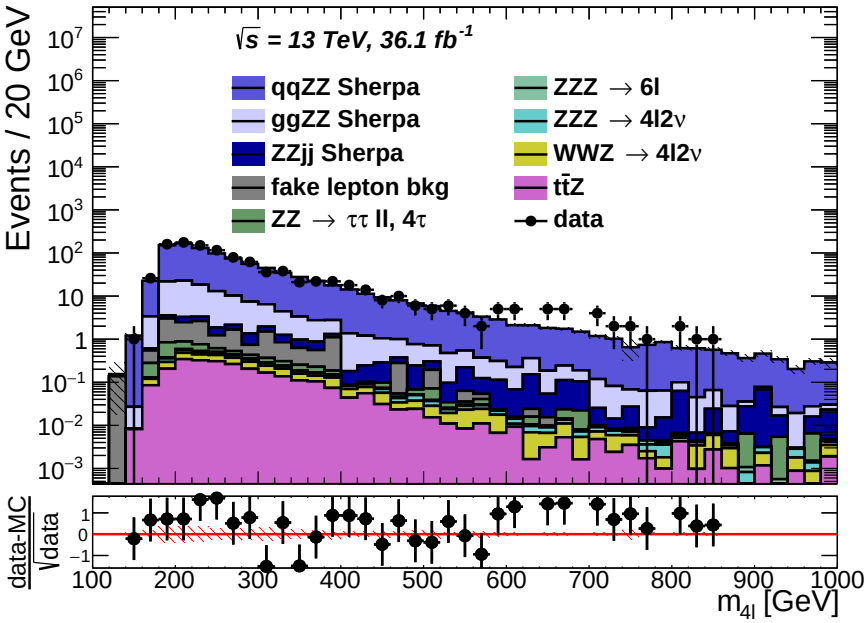

(a)

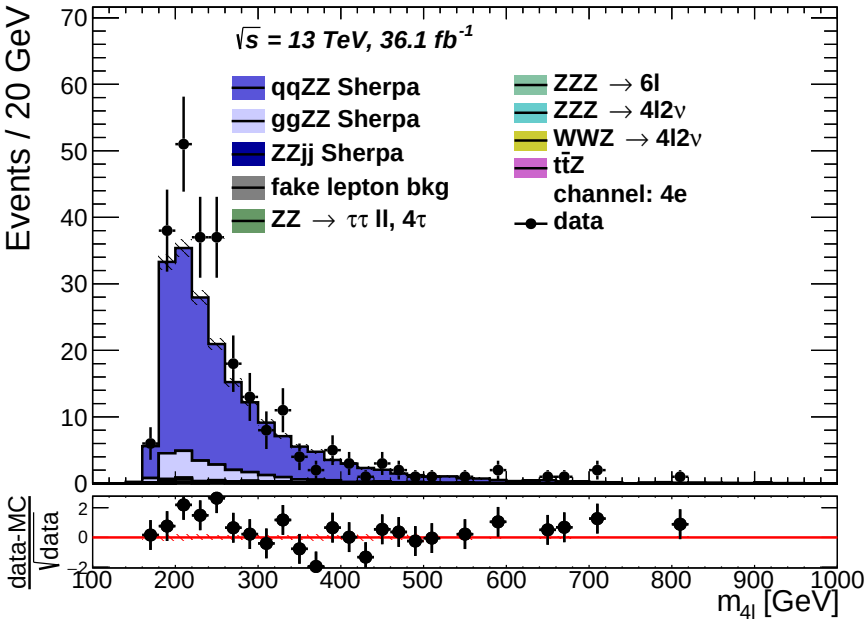

(b)

Figure 6.5: Distribution of events over the invariant mass of the 4ℓ system for the combined channel as well as the $4e$ channel.

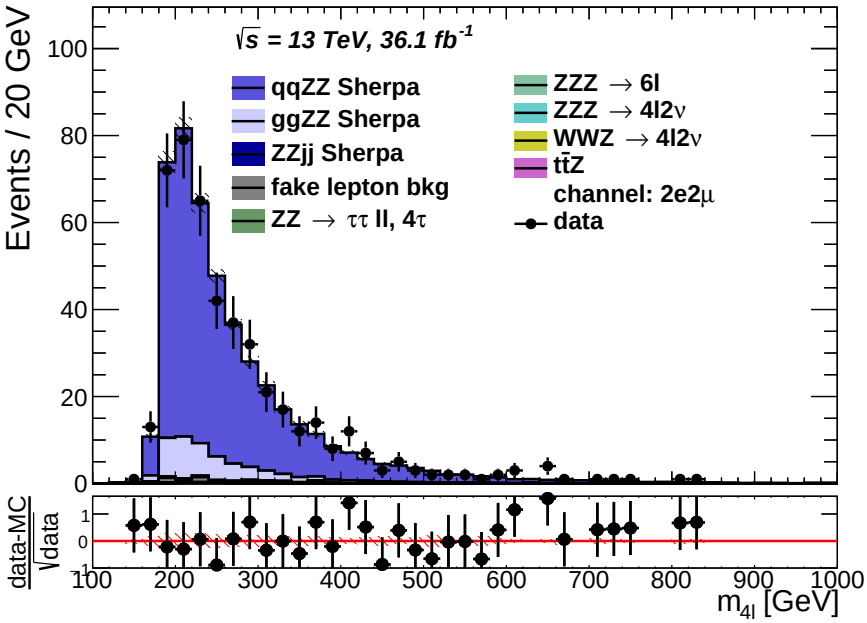

(a)

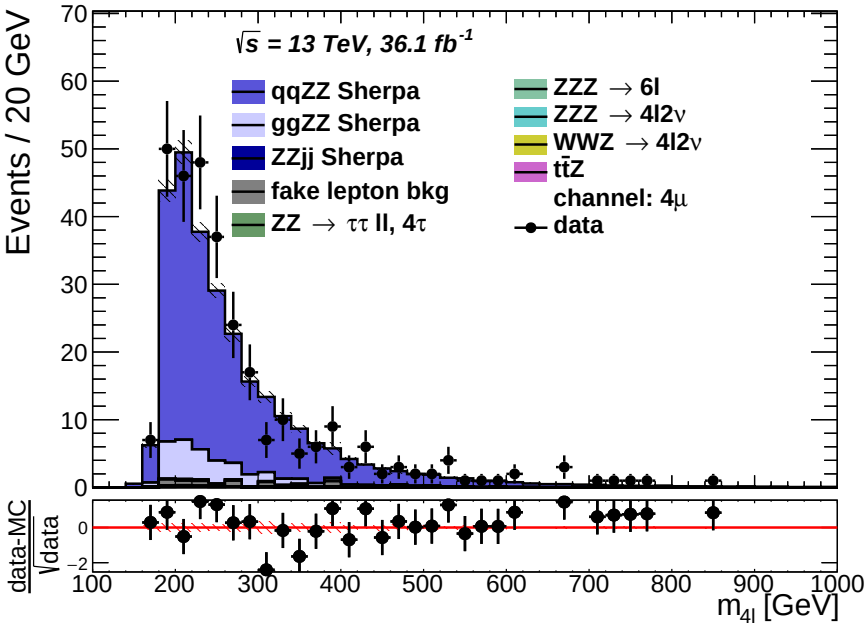

(b)

Figure 6.6: Distribution of events over the invariant mass of the 4ℓ system for the $2e2\mu$ and 4μ channels.

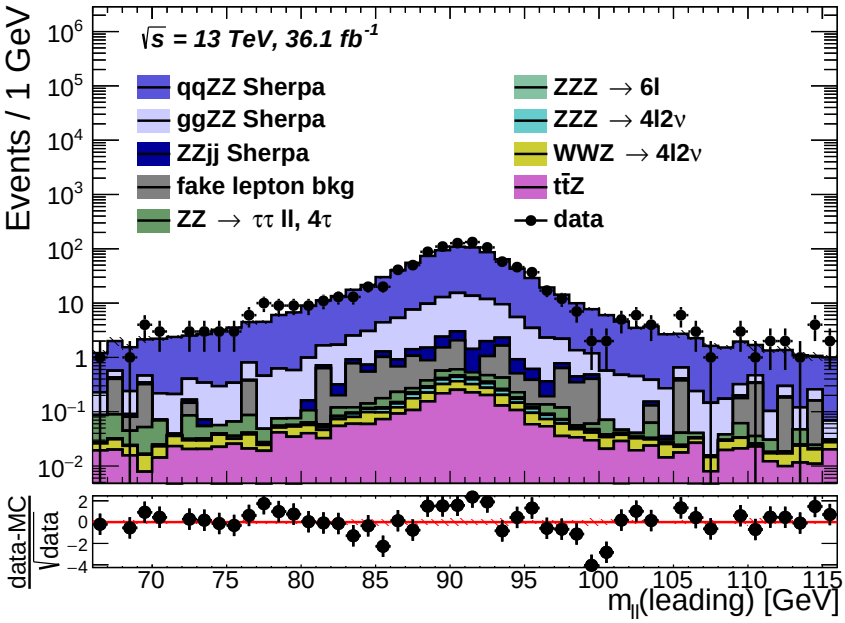

(a)

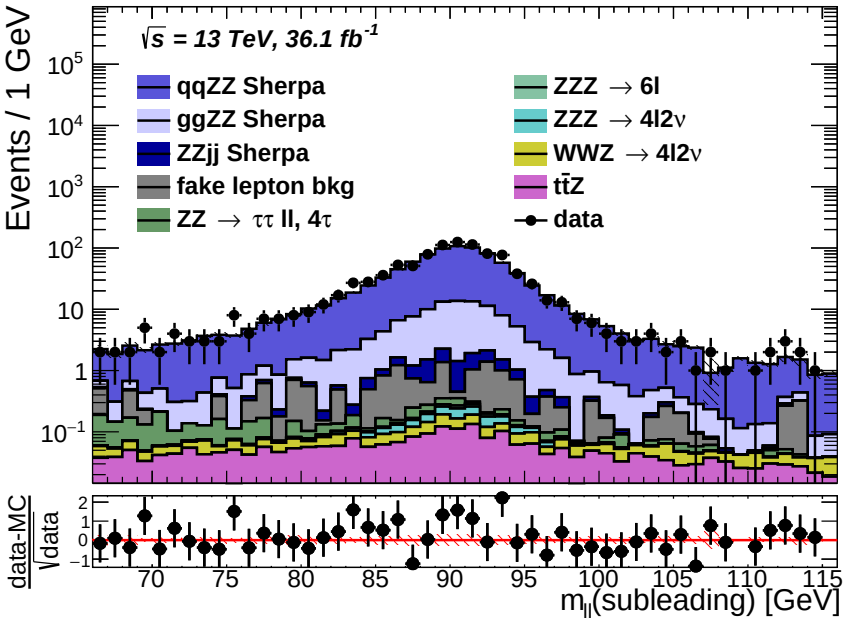

(b)

Figure 6.7: Distribution of events over the mass of the leading and subleading Z boson candidate in the event in the combined channel. The leading Z boson candidate is defined as the selected Z boson candidate with the highest p_{T} (the subleading Z candidate is the other one). The Z boson peak is clearly visible.

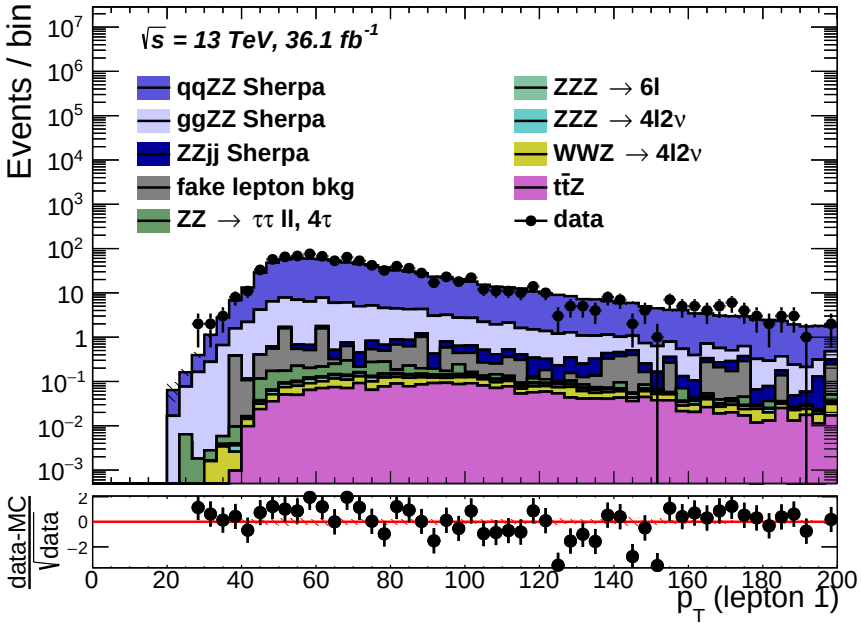

(a)

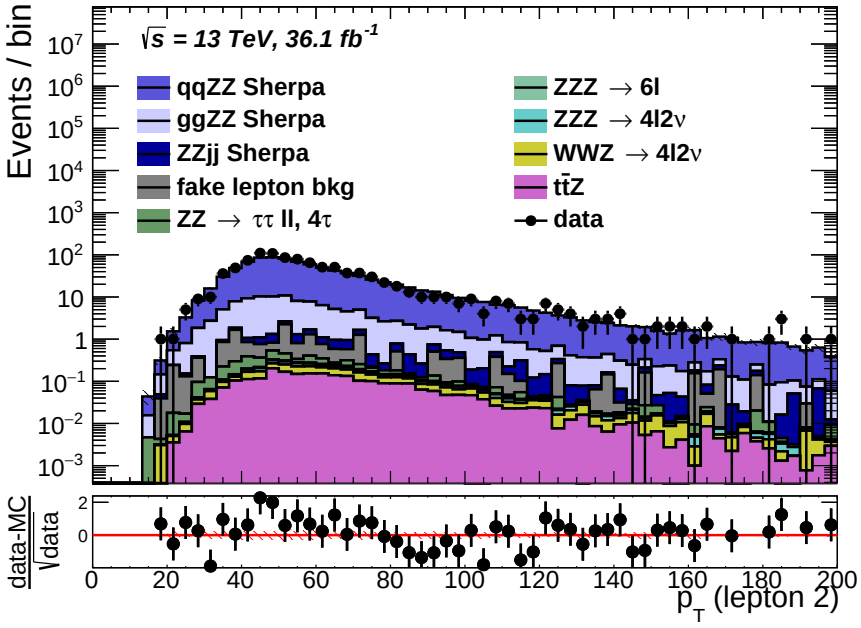

(b)

Figure 6.8: Distribution of events over the p_{T} of the leading and subleading lepton in the main Z candidate pair. The leading lepton is defined as the lepton with the highest p_{T} (the subleading lepton is second highest p_{T}).

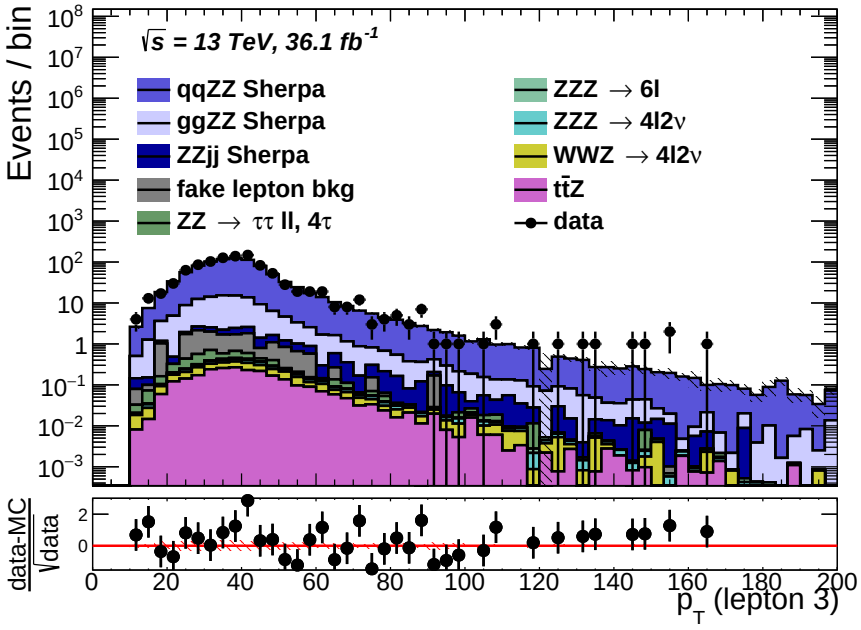

(a)

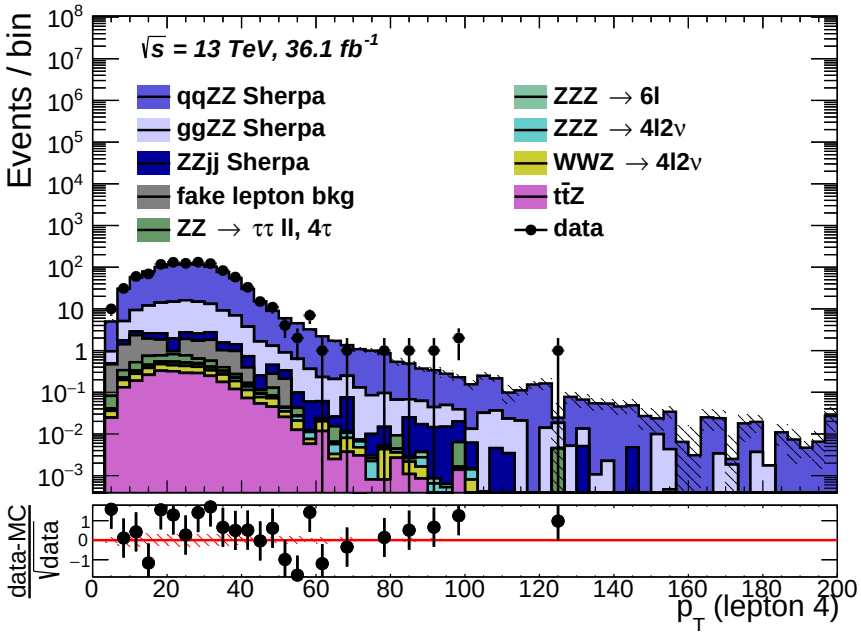

(b)

Figure 6.9: Distribution of events over the p_{T} of leptons 3 and 4 in the main Z candidate pair (in p_{T} order).

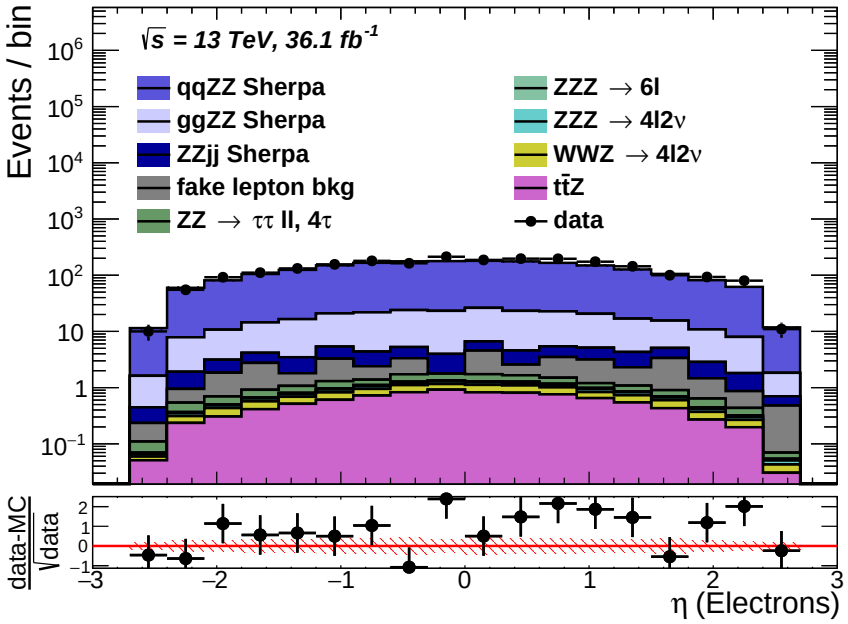

(a)

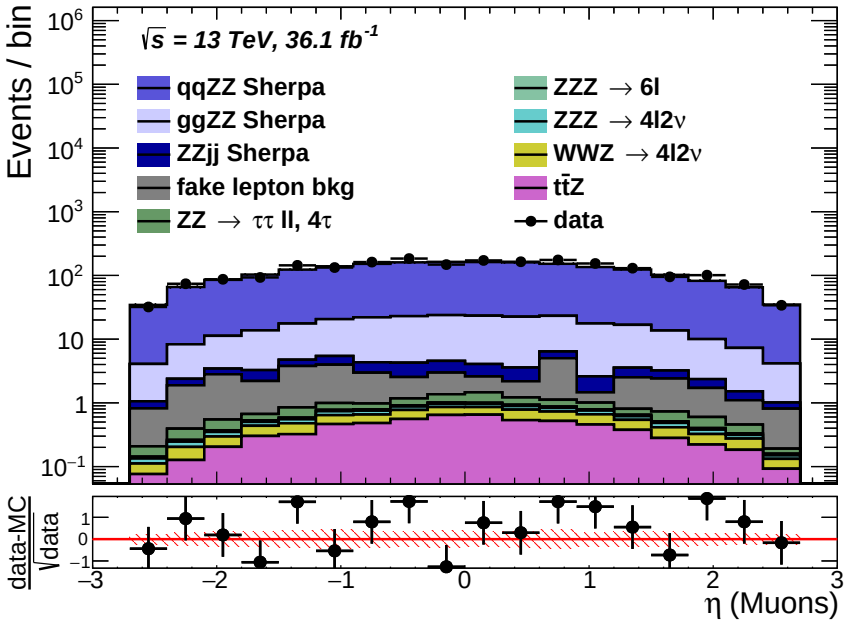

(b)

Figure 6.10: Distribution of lepton η in selected events (electrons and muons).

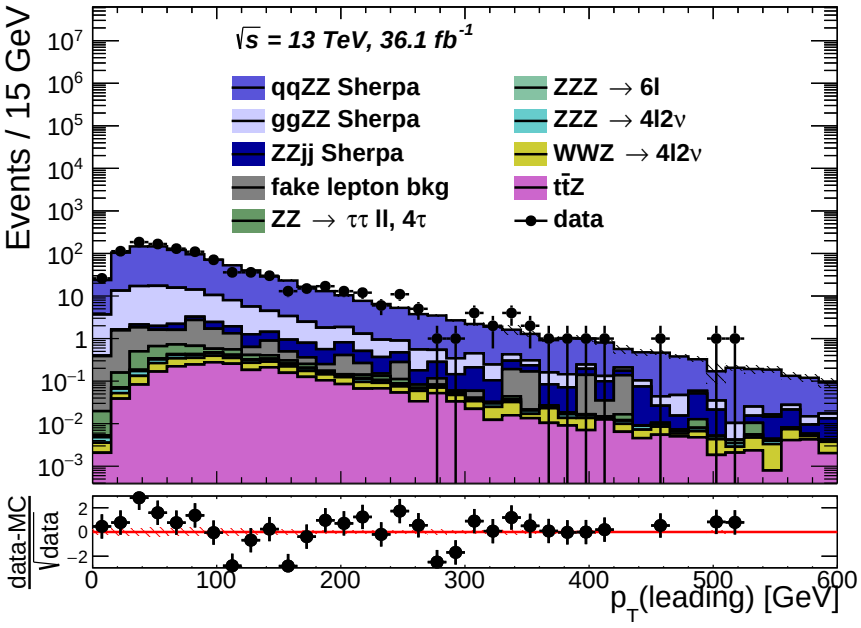

(a)

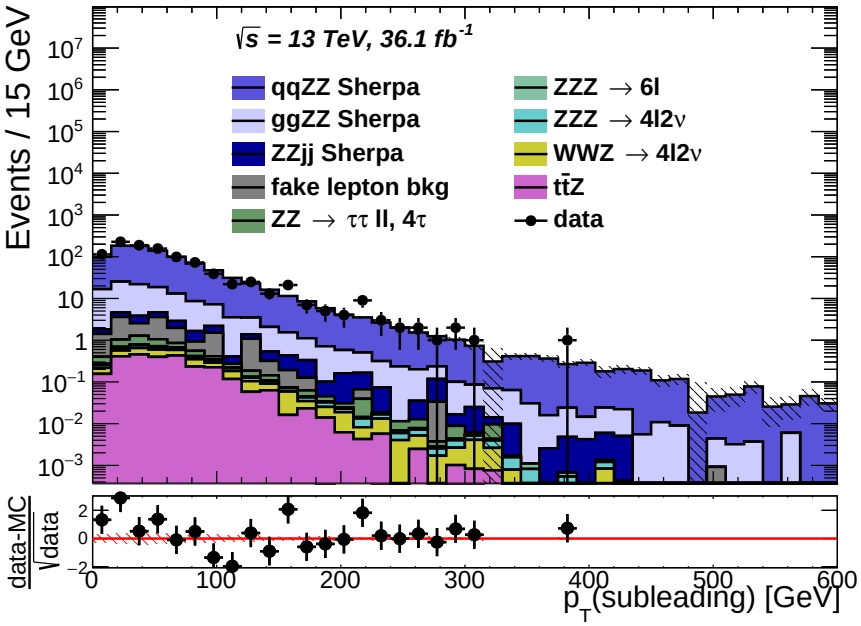

(b)

Figure 6.11: Distribution of events over the p_{T} of the leading and subleading Z boson candidate in the event. The leading Z boson candidate is defined as the selected Z boson candidate with the highest p_{T} (the subleading Z candidate is the other one).

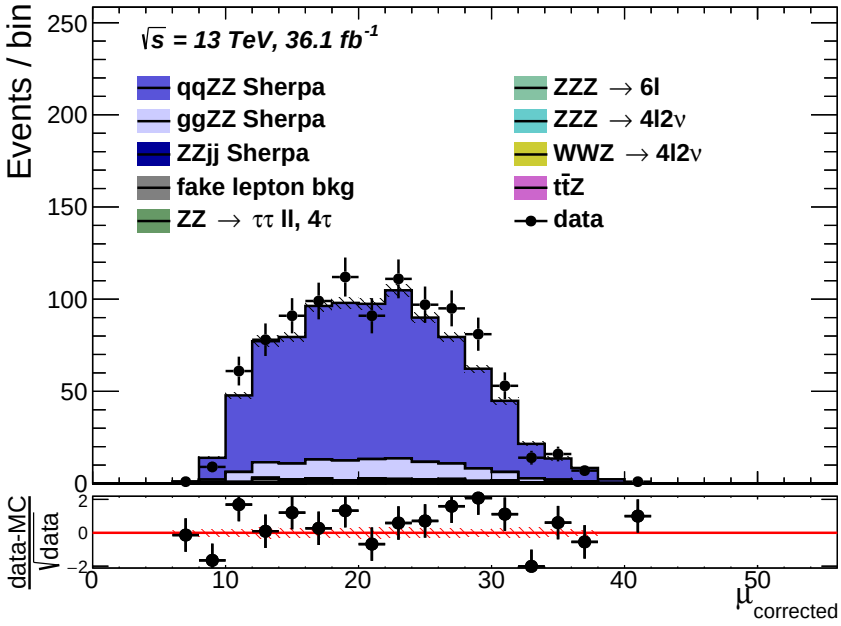

(a) Distribution of events as a function of corrected average interactions per bunch crossing. The $\mu_{corrected}$ is calculated based on the luminosity of each luminosity block.

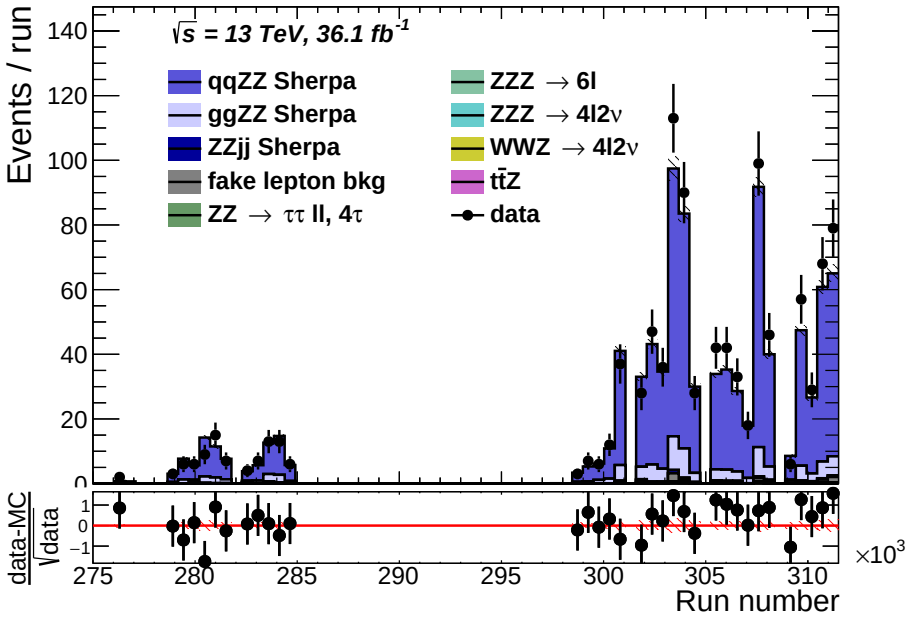

(b) Distribution of events over run number. The runs are representative of the time ATLAS gathered data, which depends on machine status and performance.

Figure 6.12

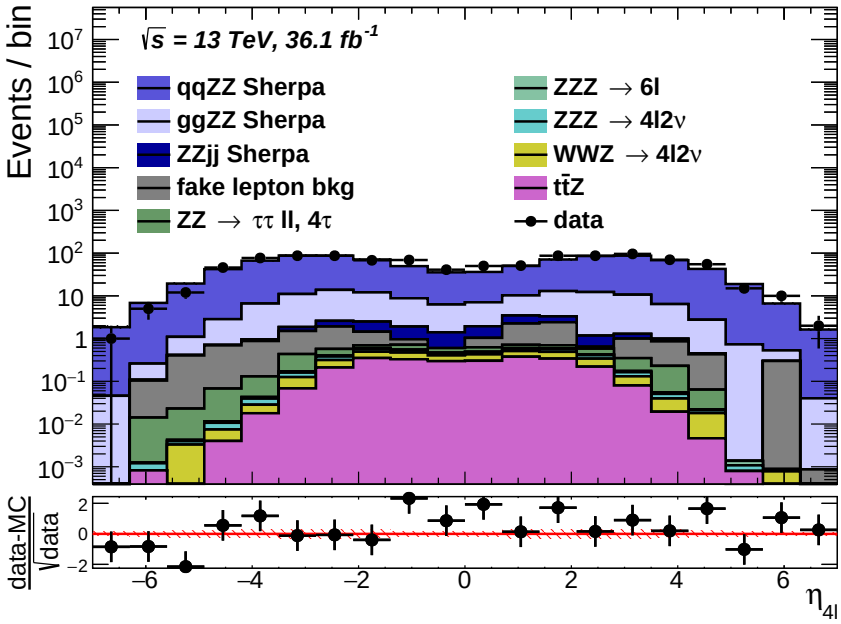

(a) The distribution of events over the pseudorapidity η of the 4ℓ system.

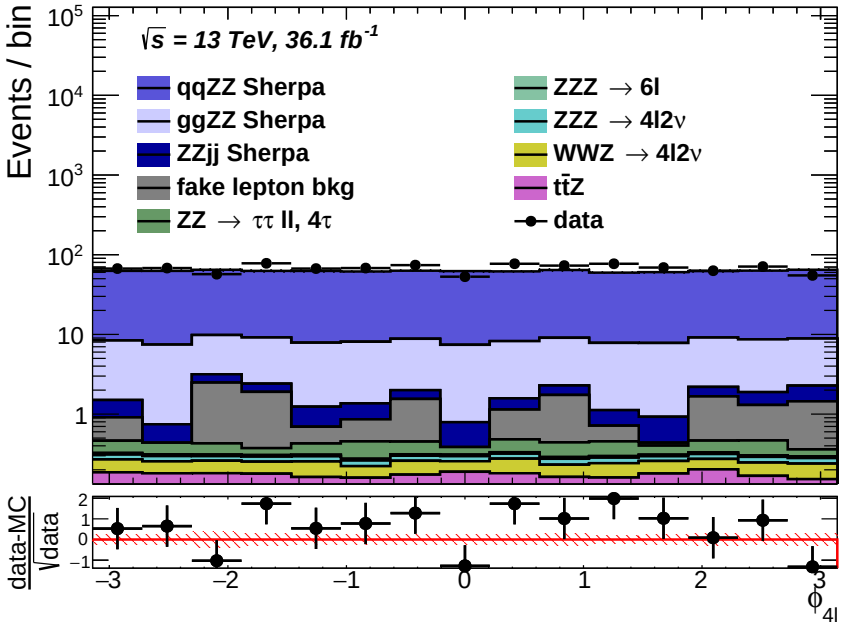

(b) The distribution of events over the azimuthal angle ϕ of the 4ℓ system.

Figure 6.13

Figure 6.14: Distribution of events in η against ϕ for the 4ℓ system. The signal prediction is shown as a box diagram (box area proportional to prediction). Backgrounds are not shown.

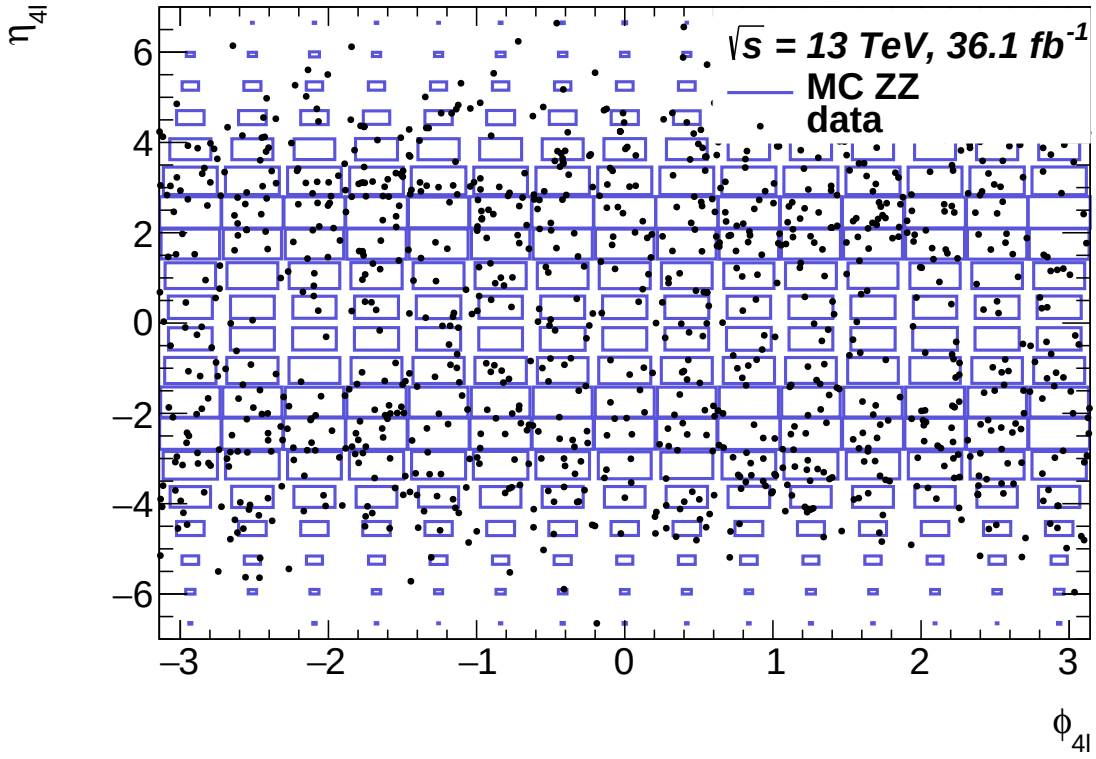

6.1 Excess in $4e$ channel

As can be seen in fig. 6.1, an excess is present in data, compared to MC, in the $4e$ channel (but not in the $2e2\mu$ or 4μ channels). This excess has been studied closely but no explanations of the excess other than statistical fluctuation has been established.

Possible explanations include new physics, physics modelling problems, electron performance problems, backgrounds and statistical fluctuations.

According to lepton universality, the only expected differences in behaviour between electrons and muons are related to their masses. Since the mass difference between electrons and muons is small compared to the Z mass and $\sqrt{s} = 13\,\text{TeV}$, any excess in the $4e$ channel should also manifest itself in the 4μ channel, where only an excess of approximately 1σ is observed. LHCb, another detector at the LHC, has observed decays of B-mesons which violate lepton universality [73], casting doubt on the principle of lepton universality as a whole. Thus it is possible that the excess is due to lepton universality violating new physics.

In fig. 6.3b, the distribution of p_{T} of the 4ℓ system, it can be seen that the excess is located primarily on the peak of the distribution. Similarly, the 4ℓ invariant mass plot fig. 6.5b shows the excess to be located on the peak of the distribution.

Further checks have been made [15, 74] (albeit not by the author of this thesis), by comparing the quantities listed in table 6.2 to three predictions (two predictions used separate SHERPA samples for the $qq \to ZZ$ contribution and one used POWHEG). The fact that the excess is present with comparison to three different predictions means that it is unlikely that the physics modelling is the reason for the excess.

The checks were also performed while applying a mass cut $87.5\,\text{GeV} < m_Z < 92.5\,\text{GeV}$ to the leading Z candidate (since that is a region where an excess was localised).

The checks listed in table 6.2 gave no indication that reconstruction or performance problems were the source of the excess.

The data driven background estimates in chapter 5 were given a conservative uncertainty of 100 % (even though the source of that uncertainty was the closure test, and closure was achieved in the $4e$ channel). If the excess was due to a background process (either one covered by the data driven method or not) an excess would also be expected in the $2e2\mu$ channel. Thus, it cannot be concluded that the excess is due to background processes.

Distributions/quantities
Number of primary vertices
Number of `Medium`/`Loose` electrons
Number of electrons removed through overlap removal
Number of electrons removed through lepton separation
1st, 2nd, 3rd and 4th lepton p_{T}, η and ϕ (numbered in p_{T} order)
3rd and 4th lepton track isolation and calorimeter isolation (numbered in p_{T} order)
largest d_0 of any lepton in leading and subleading dilepton
$d_0/\sigma(d_0)$ of each electron in leading and subleading dilepton, where $\sigma(d_0)$ is the uncertainty on d_0
Number of IBL, Pixel and SCT hits
Number of tracks associated with each electron
$z_0 \sin(\theta)$ of every lepton in main dilepton pair
ΔR between each combination of two leptons in the main dilepton pair
Main dilepton pair invariant mass
Main dilepton pair p_{T}
Leading and subleading dilepton invariant mass
Leading and subleading dilepton p_{T}
Closer and further dilepton invariant mass
Closer and further dilepton p_{T}
Mispaired dilepton invariant mass
Mispaired dilepton p_{T}
Triggers fired

Table 6.2: Checks performed (not by the author of this thesis) in search of explanation for $4e$ excess. Closer (further) dilepton means the dileptons whose invariant mass is closer (further) from the Z boson peak mass, 91.2 GeV. Mispaired dilepton refers to dilepton candidates which were not chosen as main dilepton pairs.

Chapter 7

Cross section

This chapter presents a measurement of the $pp \to ZZ$ cross section, which is compared to the SM prediction.

Three fiducial cross sections, each corresponding to the fiducial space in the different channels ($\sigma(pp \to ZZ \to 4e)$, $\sigma(pp \to ZZ \to 2e2\mu)$ and $\sigma(pp \to ZZ \to 4\mu)$), one combined fiducial cross section, corresponding to the fiducial region in all channels, regardless of decay channel ($\sigma(pp \to ZZ \to 4\ell)$) and one total cross section corresponding to $pp \to ZZ$ regardless of decay ($\sigma(pp \to ZZ)$) are extracted for proton-proton collisions at $\sqrt{s} = 13\,\text{TeV}$.

Signal acceptance and reconstruction efficiency are estimated. A statistical model is constructed in `RooFit` and used to extract the cross sections.

7.1 Expected event counts

Three statistical models are created and fitted to data, in order to extract three types of cross section: fiducial, combined fiducial and total cross sections (corresponding to the regions defined in section 4.1). There are three fiducial cross sections (one per channel), one combined fiducial cross section, and one total cross section. The fiducial cross sections is the cross section of $pp \to ZZ$ decaying into the fiducial region, and the total cross section is the cross section of any Z bosons in the $66\,\text{GeV} < m_Z < 116\,\text{GeV}$ mass range.

For a physics process, the expected number of events is given by $N_{exp} = \mathcal{L} \times \sigma$ where $\mathcal{L}$ is the integrated luminosity and σ is the cross section. In a detector like ATLAS, the reconstruction efficiency (the ratio of events that are reconstructed to be in the fiducial region to events that are truly in the fiducial region) and any expected background events also have to be taken into account.

Fiducial cross sections

For a given fiducial cross section and channel, the number of reconstructed $ZZ \to 4\ell$ events expected is given by

$$N_{exp}^{chan} = \sigma_{fid}^{chan} \mathcal{L}\, C_{ZZ}^{chan} + N_{DD}^{chan} + N_{Irr}^{chan}, \tag{7.1}$$

where N_{exp}^{chan} is the expected number of reconstructed events in the channel *chan*, σ_{fid}^{chan} is the fiducial cross section of the $pp \to ZZ \to chan$ process, $\mathcal{L}$ is the integrated luminosity, C_{ZZ}^{chan} is the reconstruction factor in the channel *chan* and N_{DD}^{chan} and N_{Irr}^{chan} are the expected background counts (Data Driven and Irreducible, respectively).

Total cross section

For a given value of the total cross section, the expected number of reconstructed $ZZ \to chan$ events (for a channel *chan*) is given by

$$N_{exp}^{chan} = \sigma_{tot} \mathcal{L}\, C_{ZZ}^{chan} A_{ZZ}^{chan} BR_{ZZ}^{chan} + N_{DD}^{chan} + N_{Irr}^{chan}, \tag{7.2}$$

where, in addition to the variables defined for eq. (7.1), σ_{tot} is the total cross section for $pp \to ZZ$, A_{ZZ}^{chan} is the fiducial extrapolation factor in the channel *chan* and BR_{ZZ}^{chan} is the branching ratio of $ZZ \to chan$. The branching ratios are 0.001131, 0.002264 and

0.001133 in the $4e$, $2e2\mu$ and 4μ channels, respectively (see table 2.2).

While eq. (7.1) involves three cross sections (which will be unconstrained in a subsequent fit), the fit using eq. (7.2) only allows one variable, σ_{tot}, to float freely.

Combined fiducial cross section

For a given combined fiducial cross section, the expected number of reconstructed $ZZ \to$ *chan* events (for a channel *chan*) is given by

$$N_{exp}^{chan} = \sigma_{fid}^{comb} \mathcal{L}\, C_{ZZ}^{chan} \frac{A_{ZZ}^{chan} BR_{ZZ}^{chan}}{\sum_{chan'} A_{ZZ}^{chan'} BR^{chan'}} + N_{DD}^{chan} + N_{Irr}^{chan}, \tag{7.3}$$

where in addition to the variables defined for eq. (7.2), σ_{fid}^{comb} is the combined fiducial cross section and $\sum_{chan'} A_{ZZ}^{chan'} BR^{chan'}$ is the sum of ${A_{ZZ}}^{chan} BR_{ZZ}^{chan}$ for all three channels. This is an extrapolation from the total cross section back to the combined fiducial cross section.

The combined fiducial cross section is the cross section of $ZZ \to 4\ell$ for all events that are within the fiducial region, regardless of channel. This is similar to adding together the fiducial cross sections for each channel (however, this method is more sophisticated in that it fixes the relative branching ratios of the different channels).

7.1.1 Reconstruction and extrapolation factors

C_{ZZ} is the reconstruction factor, i.e. the ratio of reconstructed events to events that are truly in the fiducial region:

$$C_{ZZ} = \frac{N_{reco}}{N_{fid}}. \tag{7.4}$$

This is estimated in the signal Monte Carlo samples by dividing the number of reconstructed events by the number of events in the fiducial region described in section 4.1 (the latter are called *truth fiducial* events). The reconstructed and truth fiducial events are reweighted to 36.1 fb^{-1} using the cross sections presented in table 2.3, and then summed over each signal sample (not including the aTGC sample).

Systematic uncertainties of C_{ZZ} were determined in the same way as yields were determined in section 4.6, except the luminosity uncertainty (which is correlated between the reconstructed and truth fiducial events and therefore has no impact on C_{ZZ}) and the statistical uncertainty, which is determined as follows. Given eq. (7.4), the statistical uncertainty is determined in the same sample as C_{ZZ}, using standard error

propagation as follows:

$$\sigma(C_{ZZ}) = \sigma\left(\frac{N_{reco}}{N_{fid}}\right) = \sigma\left(f\frac{N_T^r + N_{!T}^r}{N_T^r + N_T^{!r}}\right) \tag{7.5}$$

$$\begin{aligned}
\sigma(C_{ZZ}) &= \sigma(N_T^r)\frac{\partial C_{ZZ}}{\partial N_T^r} \oplus \sigma(N_T^{!r})\frac{\partial C_{ZZ}}{\partial N_T^{!r}} \oplus \sigma(N_{!T}^r)\frac{\partial C_{ZZ}}{\partial N_{!T}^r} = \\
&= f\left(\sigma(N_T^r)\frac{N_T^{!r} - N_{!T}^r}{(N_T^r + N_T^{!r})^2} \oplus \sigma(N_T^{!r})\frac{N_T^r + N_{!T}^r}{(N_T^r + N_T^{!r})^2} \oplus \sigma(N_{!T}^r)\frac{N_T^r + N_T^{!r}}{(N_T^r + N_T^{!r})^2}\right) = \\
&= \frac{f}{(N_T^r + N_T^{!r})^2}\left(\sigma(N_T^r)(N_T^{!r} - N_{!T}^r) \oplus \sigma(N_T^{!r})(N_T^r + N_{!T}^r) \oplus \sigma(N_{!T}^r)(N_T^r + N_T^{!r})\right) = \\
&= \frac{f}{(N_{fid})^2}\left(\sigma(N_T^r)(N_T^{!r} - N_{!T}^r) \oplus \sigma(N_T^{!r})(N_{reco}) \oplus \sigma(N_{!T}^r)(N_{fid})\right)
\end{aligned} \tag{7.6}$$

where N_T^r is the number of signal events that are both in the fiducial region and are reconstructed, $N_T^{!r}$ is the number of events that are in the fiducial region but are not reconstructed and $N_{!T}^r$ are reconstructed events that are not in the fiducial region (and $\oplus$ is addition in quadrature). The uncertainties $\sigma(N)$ are determined as $\sqrt{\sum w^2}$ where w is the weight of each event. Pileup reweighting and muon/electron scale factors (together referred to as reconstruction weights) are applied when evaluating the N_T^r and $N_{!T}^r$ for reconstructed events and not when evaluating the fiducial events.

C_{ZZ} and its uncertainties can be found in table 7.1. Some uncertainties vary unexpectedly from channel to channel, due to statistical fluctuations.

Similarly, A_{ZZ}, the fiducial extrapolation factor, is the ratio of events that truly are in the fiducial region to true events that are in the total region for a given channel:

$$A_{ZZ} = \frac{N_{fid}}{N_{tot}}. \tag{7.7}$$

This needs to be divided by the branching ratio of that channel to extrapolate it to the full ZZ phase space. Again, this is estimated in the Sherpa Monte Carlo sample and uncertainties are estimated by changing variables according to their uncertainties. A_{ZZ} and its uncertainties can be found in table 7.2. A_{ZZ} is estimated simultaneously in the $4e$ and 4μ channels (since the $4e$ and 4μ channels are expected to have very similar fiducial regions).

Uncertainties on A_{ZZ} are taken from [15] (except for the statistical uncertainty, which is derived by standard error propagation). A scale uncertainty is used, based on

	$4e$	$2e2\mu$	4μ
C_{ZZ}	0.517	0.638	0.769
Total	$^{+2.23\%}_{-1.37\%}$	$^{+1.6\%}_{-1.66\%}$	$^{+2.0\%}_{-2.17\%}$
Monte Carlo samples (stat.)	$^{+0.50\%}_{-0.50\%}$	$^{+0.24\%}_{-0.24\%}$	$^{+0.58\%}_{-0.58\%}$
e/γ resolution	$^{+0.12\%}_{-0.22\%}$	$^{-}_{-0.02\%}$	–
e/γ scale	$^{+0.04\%}_{-0.11\%}$	$^{-}_{-0.05\%}$	–
e ID efficiency	$^{+0.78\%}_{-0.79\%}$	$^{+0.29\%}_{-0.29\%}$	–
e Isolation efficiency	$^{+0.08\%}_{-0.08\%}$	$^{+0.03\%}_{-0.03\%}$	–
e reconstruction efficiency	$^{+0.49\%}_{-0.49\%}$	$^{+0.17\%}_{-0.18\%}$	–
μ efficiency (stat.)	–	$^{+0.27\%}_{-0.27\%}$	$^{+0.35\%}_{-0.36\%}$
μ eff. low p_{T} (stat.)	–	$^{+0.12\%}_{-0.12\%}$	$^{+0.16\%}_{-0.16\%}$
μ efficiency (syst.)	–	$^{+0.65\%}_{-0.66\%}$	$^{+0.83\%}_{-0.85\%}$
μ eff. low p_{T} (syst.)	–	$^{+0.13\%}_{-0.13\%}$	$^{+0.17\%}_{-0.17\%}$
μ identification	–	$^{+0.02\%}_{-0.01\%}$	$^{+0.06\%}_{-}$
μ isolation (stat.)	–	$^{+0.03\%}_{-0.03\%}$	$^{+0.04\%}_{-0.04\%}$
μ isolation (syst.)	–	$^{+0.16\%}_{-0.16\%}$	$^{+0.21\%}_{-0.21\%}$
μ identification (MS)	–	–	$^{+0.04\%}_{-}$
μ sagitta residual bias	–	$^{-}_{-0.01\%}$	$^{+0.01\%}_{-}$
μ sagitta ρ	–	$^{-}_{-0.04\%}$	$^{-}_{-0.08\%}$
μ scale	–	$^{+0.01\%}_{-0.01\%}$	$^{+0.03\%}_{-0.01\%}$
μ vertex assoc. (stat.)	–	$^{+0.84\%}_{-0.86\%}$	$^{+1.14\%}_{-1.22\%}$
μ vertex assoc. (syst.)	–	$^{+0.81\%}_{-0.83\%}$	$^{+1.10\%}_{-1.17\%}$
PDF	$^{+1.93\%}_{-0.67\%}$	$^{+0.59\%}_{-0.60\%}$	$^{+0.34\%}_{-0.58\%}$
PRW	$^{+0.35\%}_{-0.46\%}$	$^{+0.35\%}_{-0.46\%}$	$^{+0.35\%}_{-0.46\%}$
gg cross section	$^{+0.15\%}_{-0.15\%}$	$^{+0.07\%}_{-0.07\%}$	$^{+0.02\%}_{-0.02\%}$

Table 7.1: Reconstruction factor C_{ZZ} in the different channels, with uncertainty breakdown. Effects of less than 0.005 % are denoted by a dash.

	$4e$	$2e2\mu$	4μ
A_{ZZ}	0.590	0.574	0.590
Stat. unc	$^{+0.52\%}_{-0.52\%}$	$^{+0.52\%}_{-0.52\%}$	$^{+0.52\%}_{-0.52\%}$
PDF unc	$^{+0.36\%}_{-0.16\%}$	$^{+0.36\%}_{-0.16\%}$	$^{+0.36\%}_{-0.16\%}$
Scale unc	$^{+0.52\%}_{-0.52\%}$	$^{+0.52\%}_{-0.52\%}$	$^{+0.52\%}_{-0.52\%}$

Table 7.2: Fiducial extrapolation factor A_{ZZ} in the different channels, with uncertainties.

the choice of renormalisation and factorisation scales, normally set to the mass of the Z boson. The scales are varied individually by a factor 2 and the greatest deviation from the nominal A_{ZZ} is taken as its uncertainty. An uncertainty associated with the parton distribution functions was used. The PDF used (CT10) has 26 parameters that can be varied up and down within their uncertaintes. The PDF uncertainty is the deviation of A_{ZZ} from its nominal value for each parameter variation, added in quadrature (separately for up and down variations).

7.2 Likelihood model

To extract the cross sections from the observed data, a likelihood model is constructed in `RooFit` [75]. Its statistical part has the form

$$L_{stat} = \prod_{chan} Pois(N_{obs}^{chan}, N_{exp}^{chan}) \tag{7.8}$$

where $Pois(N_{obs}^{chan}, N_{exp}^{chan})$ is the Poisson distribution with mean N_{exp}^{chan} evaluated at the point N_{obs}^{chan}. N_{exp}^{chan} is chosen from eqs. (7.1) to (7.3) depending on which type of cross section is to be extracted.

This model is completed by the introduction of nuisance parameters associated with the uncertainties on the variables (further detailed in section 7.2.1) and then fitted to data using `Minuit2` [76]. The resulting cross sections and their uncertainties can be found in table 7.3.

7.2.1 Uncertainties

The variables C_{ZZ}, A_{ZZ}, $\mathcal{L}$, N_{Irr}, N_{DD} in eqs. (7.1) to (7.3) have uncertainties. These are introduced by allowing the variables to fluctuate, but constraining these fluctuations by modifying the likelihood model. Each variable V (out of C_{ZZ}, A_{ZZ}, $\mathcal{L}$, N_{Irr}, N_{DD}) is given the form

$$V^{chan} = V^{chan}_{Nom} + \sum_{unc} \begin{cases} \Delta V^{chan}_{unc-} \alpha^{chan}_{V\,unc}, & \text{if } \alpha^{chan}_{V\,unc} < -1 \\ poly^6, & \text{if } -1 < \alpha^{chan}_{unc} < 1 \\ \Delta V^{chan}_{unc+} \alpha^{chan}_{V\,unc}, & \text{if } \alpha^{chan}_{V\,unc} > 1 \end{cases} \tag{7.9}$$

where V is the value of the variable (used in eqs. (7.1) to (7.3) to generate expected counts), *chan* is the relevant channel (and all variables with the superscript *chan* are evaluated separately for each channel, except for $\mathcal{L}$ which is the same regardless of channel), V_{Nom} is the nominal value of the variable, *unc* is a source of uncertainty (and all variables with the subscript *unc* are evaluated separately for each source of uncertainty), $\Delta V_{unc\pm}$ is the uncertainty of the variable V due to the uncertainty source *unc* in the up and down direction, α_V is a nuisance parameter (which will be constrained in eq. (7.10)), and $poly^6$ is a six dimension polynomial which gives $V(\alpha)$ a smooth behaviour at $\alpha = \pm 1$ and $V(0) = V_{Nom}$. Some uncertainties are correlated, which means all α parameters associated with that uncertainty are the same in each channel and for each variable it affects, i.e. $\alpha^{chan}_{V\,unc} = \alpha_{unc}$ (uncorrelated uncertainties are labelled "stat." in table 7.1). An example of a variable as a function of a nuisance parameter can be seen in fig. 7.1.

To constrain the nuisance parameters in eq. (7.9), constraints are added to the likelihood model

$$L = L_{stat} * \left(\prod_{unc', V, chan} Gaus(\alpha^{chan}_{V\,unc'}, 0, 1) \right) * \left(\prod_{unc''} Gaus(\alpha_{unc''}, 0, 1) \right) \tag{7.10}$$

where, in addition to previously defined variables, L is the total likelihood, unc' is a source of uncorrelated uncertainty, unc'' is a source of correlated uncertainty and $Gaus(\alpha, 0, 1)$ is a Gaussian distribution with mean 0 and standard deviation 1, evaluated at α (L_{stat} also depends on the α parameters via eq. (7.9)).

In the fit to data, the uncertainties are turned off individually (by setting α parame-

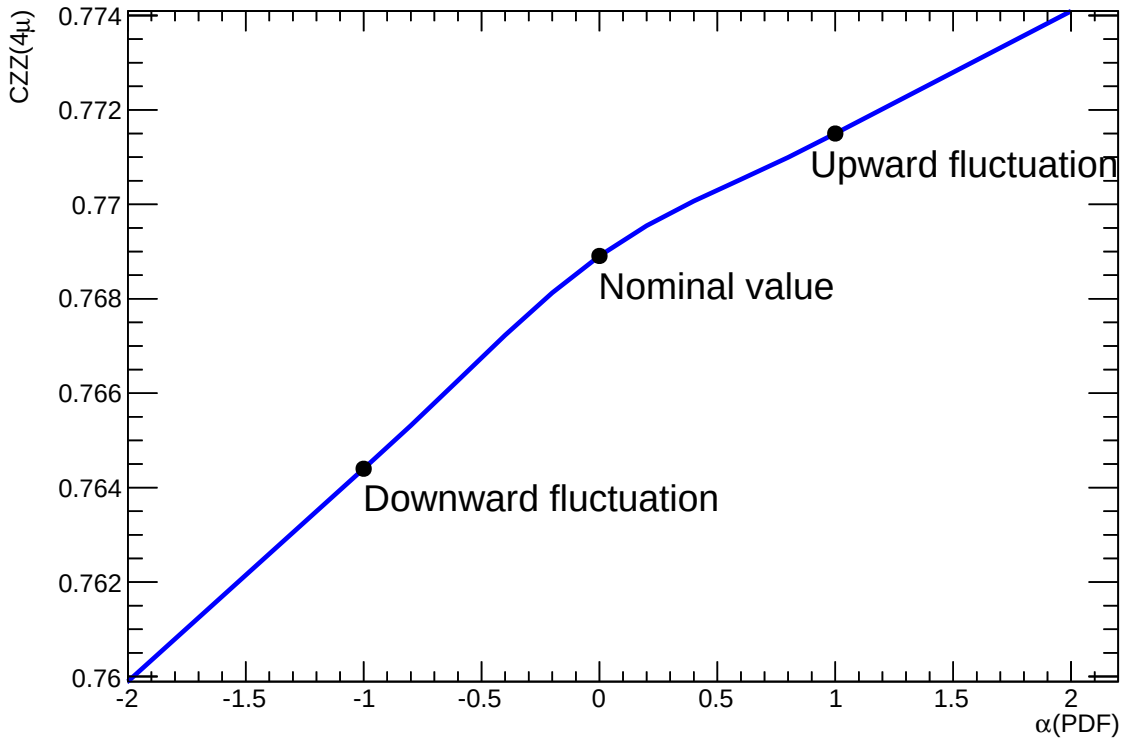

Figure 7.1: An example of a variable ($C_{ZZ}^{4\mu}$) as a function of a nuisance parameter (associated with the PDFs). When the nuisance parameter is outside the range $-1 < \alpha < 1$, the variable is linear. Inside that range, the two linear pieces are joined smoothly by a sixth order polynomial.

ters constant) in order to determine the contribution to the total uncertainty from each source.

7.3 Fitting procedure and goodness of fit

7.3.1 Fit to data and uncertainty extraction

Once the likelihood model in eq. (7.10) is constructed, the model is fitted to data, using `Minuit2`. The fiducial cross sections are fitted simultaneously, and the total and combined fiducial cross sections are fitted separately. The result and uncertainties (determined by `Minos` [77]) can be seen in table 7.3.

The contribution to the uncertainty from statistics is determined by refitting the model but setting all nuisance parameters constant at zero. The systematic uncertainty contribution from different sources are determined by setting the nuisance parameters associated with the source in question constant and subtracting the resulting uncertainty from the total uncertainty in quadrature. The combined systematic uncertainty is determined by the same process but setting all nuisance parameters constant. A full breakdown of the uncertainty contributions from different sources can be found in table 7.4.

A validation of the cross section extraction can be seen in fig. 7.2, where 100,000 pseudo experiments were generated, using a total cross section of 16.5 fb (which is the measured cross section). The pseudo experiments were generated using the same model as is used in the cross section extraction. It contains all uncertainties and their correlations. A Gaussian fit to the distribution of measured cross sections can also be seen. Its mean is 16.50 ± 0.0003 pb, which is consistent with the cross section at which the pseudo experiments were generated and it has a width of 0.807 ± 0.002 pb, which is consistent with the uncertainty of the total cross section from table 7.3. The uncertainties from the pseudo experiments can be seen in fig. 7.3. The uncertainties from the pseudo experiments are consistent with the uncertainty of the measured total cross section from table 7.3.

7.3.2 Goodness of fit

To determine an estimate of the quality of the fit, a test statistic Λ is compared in data and pseudo experiments (same as in section 7.3.1). The model in equation 7.10 can be

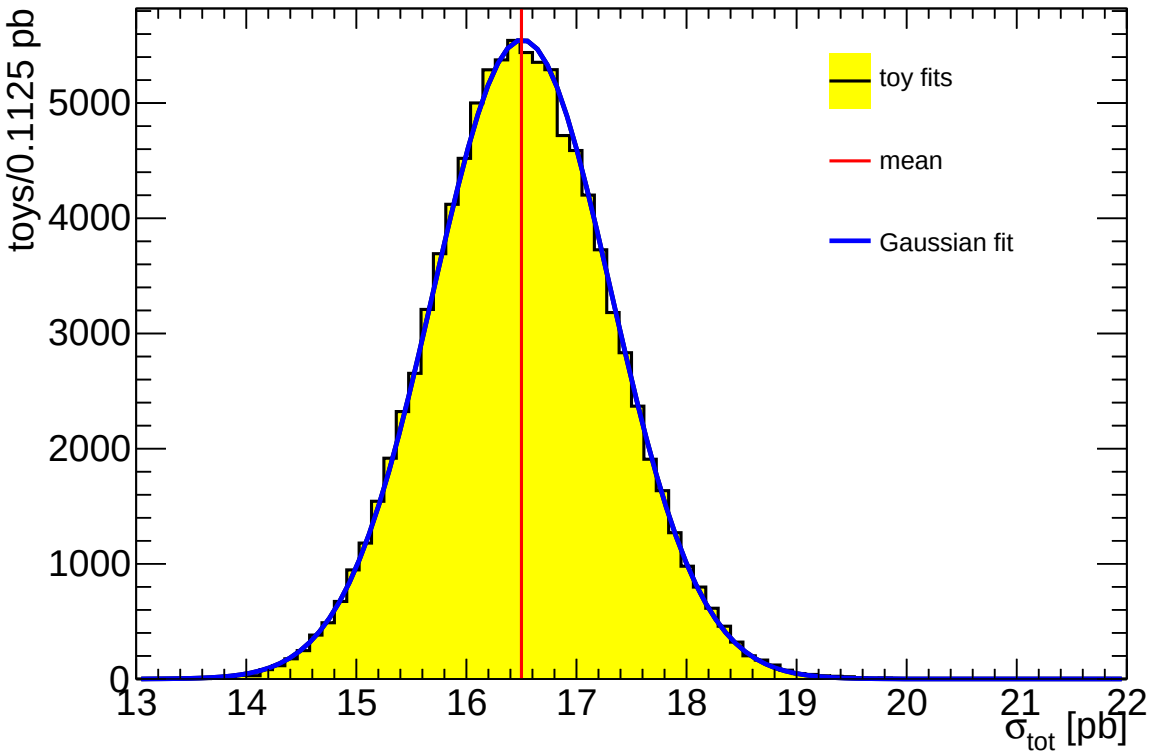

Figure 7.2: The measured total cross section in 100,000 pseudo experiments, generated with a total cross section σ^{gen} of 16.5 pb, the measured total cross section. A Gaussian fit to the distribution of measured cross sections can also be seen. Its mean is 16.50±0.0003 pb, which is consistent with the cross section at which the pseudo experiments were generated and it has a width of 0.807±0.002 pb, which is consistent with the uncertainty of the total cross section from table 7.3.

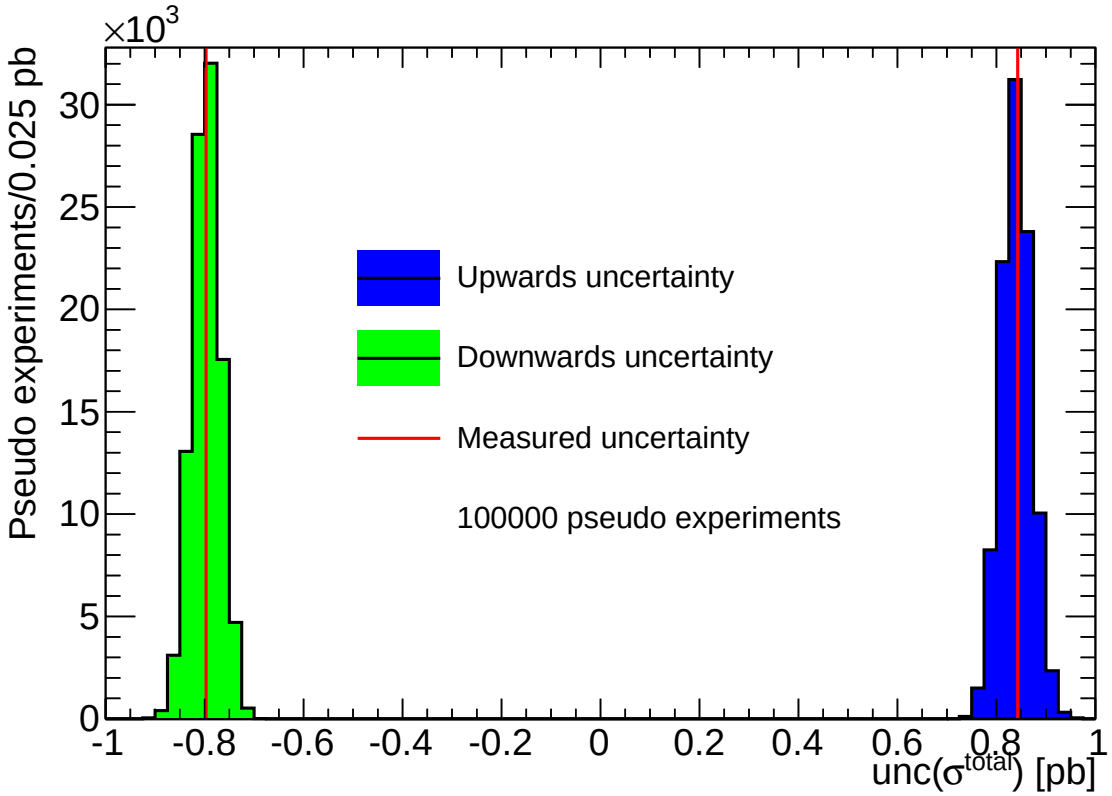

Figure 7.3: The measured total cross section uncertainty in 100,000 pseudo experiments used for fig. 7.2. The uncertainties from the pseudo experiments are consistent with the uncertainty of the measured total cross section from table 7.3. The measured cross section uncertainty can be seen as vertical lines in this plot.

used to produce pseudo data for a large number of pseudo experiments. Λ is defined as

$$\Lambda = -2 \ln \left(\frac{L(data)}{L(best)} \right), \tag{7.11}$$

where *data* is the dataset with respect to which Λ is calculated (can be observed data or pseudo data) and *best* is the hypothetical dataset which has the best possible agreement with the given cross section (in other words, N_{exp}^{chan} from eqs. (7.1) to (7.3)). $L(x)$ is the likelihood after fitting to a dataset x. Since *best* is the dataset that is most consistent with σ^{gen}, L_{best} is the highest likelihood value possible (given the measured cross section). The test statistic Λ is χ^2 distributed in the absence of uncertainties. The distribution of Λ from pseudo experiments and the Λ from the fit to data can be seen in fig. 7.4.

A p-value is determined by calculating what fraction of pseudo experiments have a higher Λ than observed in data. The observed Λ of 10.3 corresonds to p-value of 0.7 %. In the fiducial cross section calculations (except the combined fiducial), N_{exp}^{chan} is only constrained to be as close to N_{obs}^{chan} as possible, and so all components to the likelihood are at their maximum, Λ is always zero and the p-value is undefined. In other words, there are three degrees of freedom to three observables, so the fit is underconstrained.

7.4 Results

The results of the cross section extraction can be found in table 7.3, with an uncertainty breakdown in table 7.4.

A comparison of measured fiducial cross sections can be seen in fig. 7.5. A comparison of the total cross section and a NNLO theoretical prediction (using MATRIX [24]) as well as other measurements of the same process can be seen in fig. 7.6.

The Λ for the total cross section fit is 10.3, which corresponds to a p-value of 0.7 % as can be seen in fig. 7.4. By construction, p-values are distributed equally over the range $0 \to 1$. The low p-value of the fit is due to the excess in the $4e$ channel.

The values of the nuisance parameters after the fit to the total cross section can be seen in fig. 7.7. The deviations from zero are due to the unexpected excess in the $4e$ channel. The non-zero α values indicate that the most likely scenario (according to the model) is that the excess is due to the PDF uncertainty since the PDF introduces the largest uncertainties (in addition to statistical fluctuations and undermeasured muon

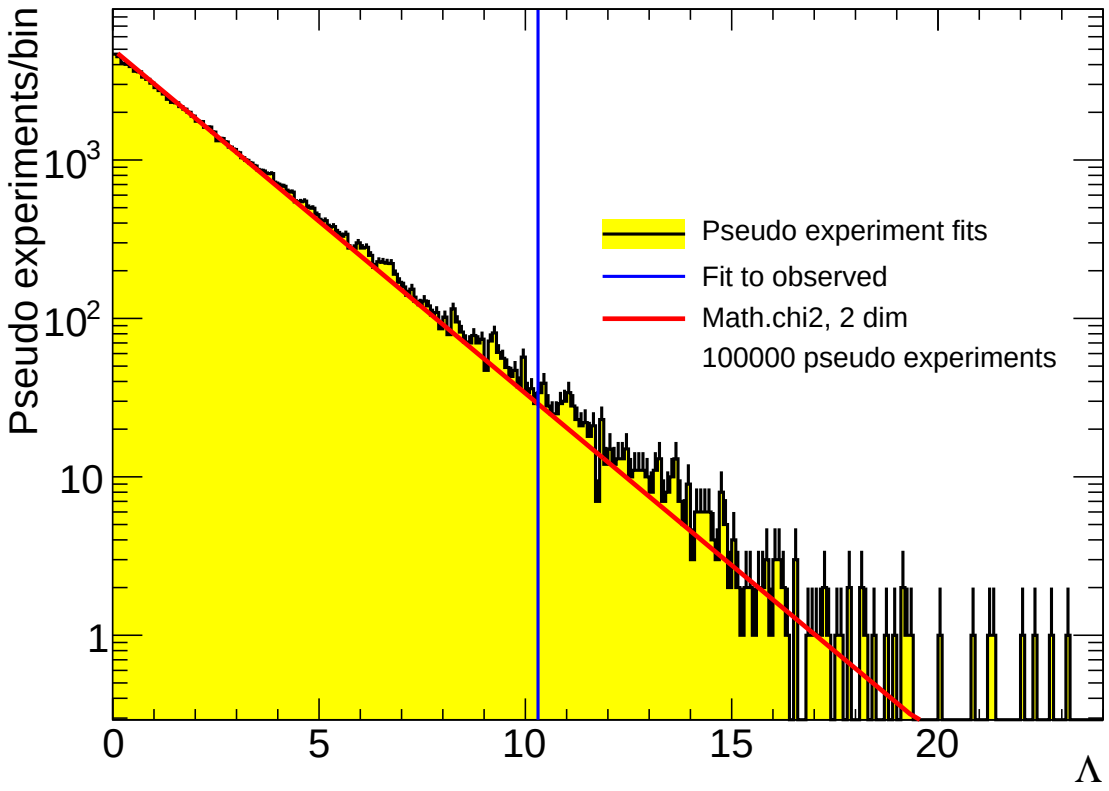

Figure 7.4: The goodness of fit test statistic Λ from the total cross section fit compared to its expected distribution, evaluated in cross section measurements of 100,000 pseudo experiments. The observed Λ of 10.3 corresonds to p-value of 0.7 %. The plot also shows the χ^2 distribution for two degrees of freedom, labelled Math.chi2, 2 dim (one degree for each of the three channels, minus one degree for the fit parameter). The χ^2 distribution is normalised to have the same integral as the Λ distribution. The deviation of Λ from χ^2 is due to the uncertainties, whose nuisance parameters effectively act as partial degrees of freedom.

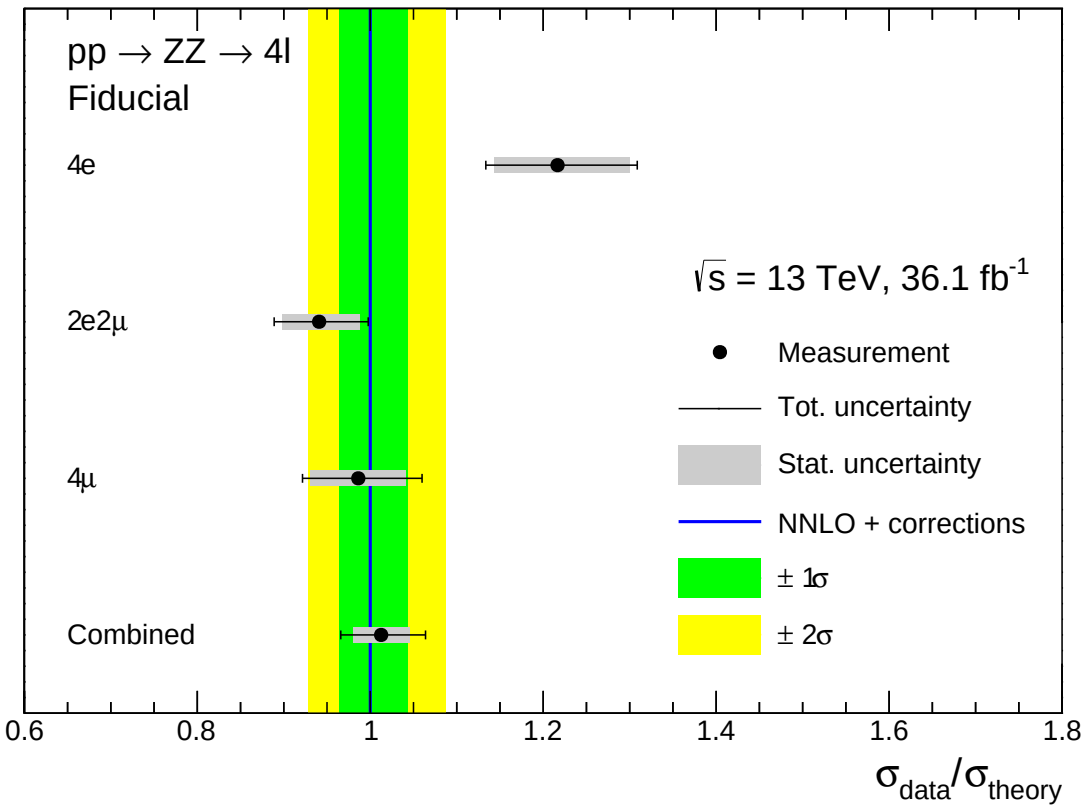

Figure 7.5: The ratio of measured cross section to prediction from MATRIX from table 2.4 (with SHERPA for $ZZqq$). The MATRIX prediction uses the PDFs NNPDF 3.0 NNLO [25] and includes electroweak corrections [26, 27] as well as the k-factor of 1.67 on the gg contribution. The error bands are the QCD scale uncertainty shown as a one- and a two-standard-deviation band. For the measured cross sections, both statistical and total uncertainties are shown.

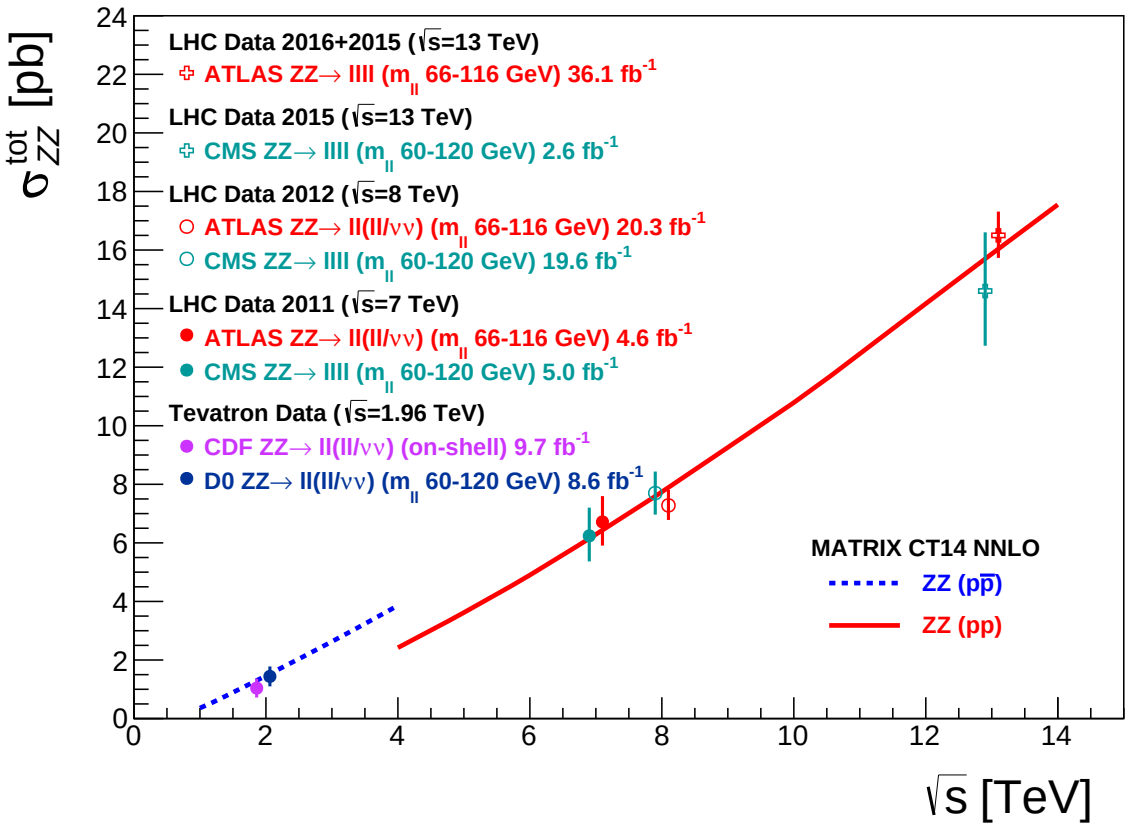

Figure 7.6: A comparison of the measured total cross section ($\sigma(pp \to ZZ)$) to NNLO theoretical prediction as well as other measurements of the same process [14, 18, 19, 29–32, 78, 79]. The NNLO prediction is calculated the same way as in fig. 7.5 except that it does not include electroweak corrections (since they are not available as a function of $\sqrt{s}$). The measurement presented in this thesis corresponds to the rightmost data point.

Measurement								
σ		(tot.)	(stat.)	(syst.)	(lumi.)		Prediction	
σ_{4e}^{fid}	13.2	$^{+1.0}_{-0.9}$	$^{+0.9}_{-0.8}$	$^{+0.2}_{-0.3}$	$^{+0.4}_{-0.4}$	fb	$10.9^{+0.5}_{-0.4}$	fb
$\sigma_{2e2\mu}^{fid}$	19.9	$^{+1.2}_{-1.2}$	$^{+1.0}_{-0.9}$	$^{+0.4}_{-0.4}$	$^{+0.7}_{-0.6}$	fb	$21.2^{+0.9}_{-0.8}$	fb
$\sigma_{4\mu}^{fid}$	10.7	$^{+0.8}_{-0.7}$	$^{+0.6}_{-0.6}$	$^{+0.3}_{-0.3}$	$^{+0.4}_{-0.3}$	fb	$10.9^{+0.5}_{-0.4}$	fb
σ_{comb}^{fid}	43.4	$^{+2.2}_{-2.1}$	$^{+1.4}_{-1.4}$	$^{+0.9}_{-0.8}$	$^{+1.4}_{-1.3}$	fb	$42.9^{+1.9}_{-1.5}$	fb
σ^{total}	16.5	$^{+0.8}_{-0.8}$	$^{+0.5}_{-0.5}$	$^{+0.4}_{-0.4}$	$^{+0.5}_{-0.5}$	pb	$16.9^{+0.6}_{-0.5}$	pb

Table 7.3: Results from the cross section extraction, with uncertainties. The predicted values are taken from table 2.4.

efficiencies due to muon reconstruction and TTVA). In the fiducial cross section fit, the variables are simultaneously fitted to three observables, so $N_{obs}^{chan} = N_{exp}^{chan}(\sigma_{fid}^{chan})$ in every channel. Thus, all nuisance parameters in the fiducial cross section extraction are zero.

7.4.1 Discussion

The results are compatible with the earlier measurements of 13 TeV data seen in table 2.5 but have a higher precision. The measured value of the combined fiducial cross section 43.4 fb is compatible with the sum of the measured fiducial cross sections per channel, 43.8 fb. Given the dependence of the precision on the luminosity, future data taking and upgrades such as a High Luminosity LHC will be able to improve the precision. High Luminosity LHC is expected to provide approximately $3000\,\text{fb}^{-1}$, which could lower the statistical uncertainty as low as 0.4 %. Future experiments, like CLIC [80] and future circular colliders [81, 82] can also provide measurements at other energies in the future.

Some cross section uncertainties are asymmetric even though the uncertainty introduced in the model is symmetric. This is most noticeable in the luminosity uncertainty. This is due to a statistical effect: When an uncertainty is introduced on the mean of a poisson distribution, that mean is allowed to fluctuate up and down. Since the statistical uncertainty due to a poisson distributed variable goes approximately as $\sqrt{\text{mean}}$, the statistical uncertainty becomes larger when the mean fluctuates upwards, but smaller

	σ_{fid}^{4e}	$\sigma_{fid}^{2e2\mu}$	$\sigma_{fid}^{4\mu}$	σ_{fid}^{comb}	σ_{total}
Luminosity	$^{+3.33\%}_{-2.92\%}$	$^{+3.28\%}_{-2.96\%}$	$^{+3.32\%}_{-2.94\%}$	$^{+3.26\%}_{-2.99\%}$	$^{+3.26\%}_{-2.99\%}$
Statistical	$^{+6.56\%}_{-6.29\%}$	$^{+4.78\%}_{-4.64\%}$	$^{+5.99\%}_{-5.76\%}$	$^{+3.22\%}_{-3.15\%}$	$^{+3.22\%}_{-3.15\%}$
Systematic	$^{+1.86\%}_{-1.96\%}$	$^{+1.97\%}_{-1.83\%}$	$^{+2.74\%}_{-2.52\%}$	$^{+2.05\%}_{-1.89\%}$	$^{+2.31\%}_{-2.13\%}$
- Monte Carlo samples (stat.)	$^{+0.53\%}_{-0.46\%}$	$^{+0.25\%}_{-0.22\%}$	$^{+0.62\%}_{-0.55\%}$	$^{+0.24\%}_{-0.22\%}$	$^{+0.24\%}_{-0.22\%}$
- e/γ resolution	$^{+0.19\%}_{-0.16\%}$	$^{+0.02\%}_{-0.02\%}$	-	$^{+0.04\%}_{-0.04\%}$	$^{+0.04\%}_{-0.04\%}$
- e/γ scale	$^{+0.08\%}_{-0.07\%}$	$^{+0.02\%}_{-0.02\%}$	-	$^{+0.03\%}_{-0.03\%}$	$^{+0.03\%}_{-0.03\%}$
- e ID efficiency	$^{+0.83\%}_{-0.73\%}$	$^{+0.31\%}_{-0.28\%}$	-	$^{+0.32\%}_{-0.30\%}$	$^{+0.32\%}_{-0.30\%}$
- e Isolation efficiency	$^{+0.08\%}_{-0.07\%}$	$^{+0.03\%}_{-0.03\%}$	-	$^{+0.03\%}_{-0.03\%}$	$^{+0.03\%}_{-0.03\%}$
- e reconstruction efficiency	$^{+0.51\%}_{-0.45\%}$	$^{+0.18\%}_{-0.16\%}$	-	$^{+0.20\%}_{-0.18\%}$	$^{+0.20\%}_{-0.18\%}$
- μ identification	-	$^{+0.02\%}_{-0.02\%}$	$^{+0.03\%}_{-0.03\%}$	$^{+0.02\%}_{-0.02\%}$	$^{+0.02\%}_{-0.02\%}$
- μ identification (MS)	-	-	$^{+0.02\%}_{-0.02\%}$	$^{+0.01\%}_{-0.01\%}$	$^{+0.01\%}_{-0.01\%}$
- μ scale	-	$^{+0.02\%}_{-0.02\%}$	$^{+0.02\%}_{-0.02\%}$	$^{+0.01\%}_{-0.01\%}$	$^{+0.01\%}_{-0.01\%}$
- μ efficiency (stat.)	-	$^{+0.29\%}_{-0.26\%}$	$^{+0.38\%}_{-0.34\%}$	$^{+0.26\%}_{-0.23\%}$	$^{+0.26\%}_{-0.23\%}$
- μ eff. low p_{T} (stat.)	-	$^{+0.13\%}_{-0.12\%}$	$^{+0.17\%}_{-0.15\%}$	$^{+0.11\%}_{-0.10\%}$	$^{+0.11\%}_{-0.10\%}$
- μ efficiency (syst.)	-	$^{+0.68\%}_{-0.62\%}$	$^{+0.90\%}_{-0.79\%}$	$^{+0.61\%}_{-0.56\%}$	$^{+0.61\%}_{-0.56\%}$
- μ eff. low p_{T} (syst.)	-	$^{+0.13\%}_{-0.12\%}$	$^{+0.18\%}_{-0.16\%}$	$^{+0.12\%}_{-0.11\%}$	$^{+0.12\%}_{-0.11\%}$
- μ isolation (stat.)	-	$^{+0.03\%}_{-0.03\%}$	$^{+0.04\%}_{-0.04\%}$	$^{+0.03\%}_{-0.03\%}$	$^{+0.03\%}_{-0.03\%}$
- μ isolation (syst.)	-	$^{+0.16\%}_{-0.15\%}$	$^{+0.22\%}_{-0.20\%}$	$^{+0.15\%}_{-0.13\%}$	$^{+0.15\%}_{-0.13\%}$
- μ vertex assoc. (stat.)	-	$^{+0.89\%}_{-0.80\%}$	$^{+1.26\%}_{-1.10\%}$	$^{+0.84\%}_{-0.76\%}$	$^{+0.84\%}_{-0.76\%}$
- μ vertex assoc. (syst.)	-	$^{+0.87\%}_{-0.78\%}$	$^{+1.22\%}_{-1.06\%}$	$^{+0.80\%}_{-0.73\%}$	$^{+0.80\%}_{-0.73\%}$
- μ sagitta residual bias	-	$^{+0.01\%}_{-0.01\%}$	$^{+0.01\%}_{-0.01\%}$	$^{+0.01\%}_{-0.01\%}$	$^{+0.01\%}_{-0.01\%}$
- μ sagitta ρ	-	$^{+0.02\%}_{-0.02\%}$	$^{+0.04\%}_{-0.04\%}$	$^{+0.03\%}_{-0.02\%}$	$^{+0.03\%}_{-0.02\%}$
- PDF	$^{+1.20\%}_{-1.45\%}$	$^{+0.63\%}_{-0.56\%}$	$^{+0.51\%}_{-0.42\%}$	$^{+0.93\%}_{-0.77\%}$	$^{+0.93\%}_{-0.77\%}$
- Pileup reweighting	$^{+0.44\%}_{-0.37\%}$	$^{+0.43\%}_{-0.37\%}$	$^{+0.44\%}_{-0.37\%}$	$^{+0.43\%}_{-0.38\%}$	$^{+0.43\%}_{-0.38\%}$
- gg cross section	$^{+0.15\%}_{-0.14\%}$	$^{+0.07\%}_{-0.06\%}$	$^{+0.01\%}_{-0.01\%}$	$^{+0.07\%}_{-0.06\%}$	$^{+0.07\%}_{-0.06\%}$
- A_{ZZ} (stat.)	-	-	-	-	$^{+0.54\%}_{-0.50\%}$
- A_{ZZ} PDF	-	-	-	-	$^{+0.42\%}_{-0.37\%}$
- A_{ZZ} Scale	-	-	-	-	$^{+0.81\%}_{-0.77\%}$
- Irreducible bkg. (stat.)	$^{+0.04\%}_{-0.04\%}$	$^{+0.02\%}_{-0.02\%}$	$^{+0.03\%}_{-0.03\%}$	$^{+0.02\%}_{-0.02\%}$	$^{+0.02\%}_{-0.02\%}$
- Irreducible bkg. (syst.)	$^{+0.19\%}_{-0.19\%}$	$^{+0.19\%}_{-0.18\%}$	$^{+0.22\%}_{-0.21\%}$	$^{+0.20\%}_{-0.19\%}$	$^{+0.20\%}_{-0.19\%}$
- Data driven bkg. (syst.)	$^{+0.71\%}_{-0.70\%}$	$^{+0.98\%}_{-0.96\%}$	$^{+1.59\%}_{-1.58\%}$	$^{+1.08\%}_{-1.05\%}$	$^{+1.08\%}_{-1.05\%}$

Table 7.4: Uncertainty breakdown for cross section extractions. "Systematic" is a combination of all systematic uncertainties (except for luminosity) and "Statistical" is the statistical uncertainty on the data. Contributions less than 0.005 % are denoted by a dash.

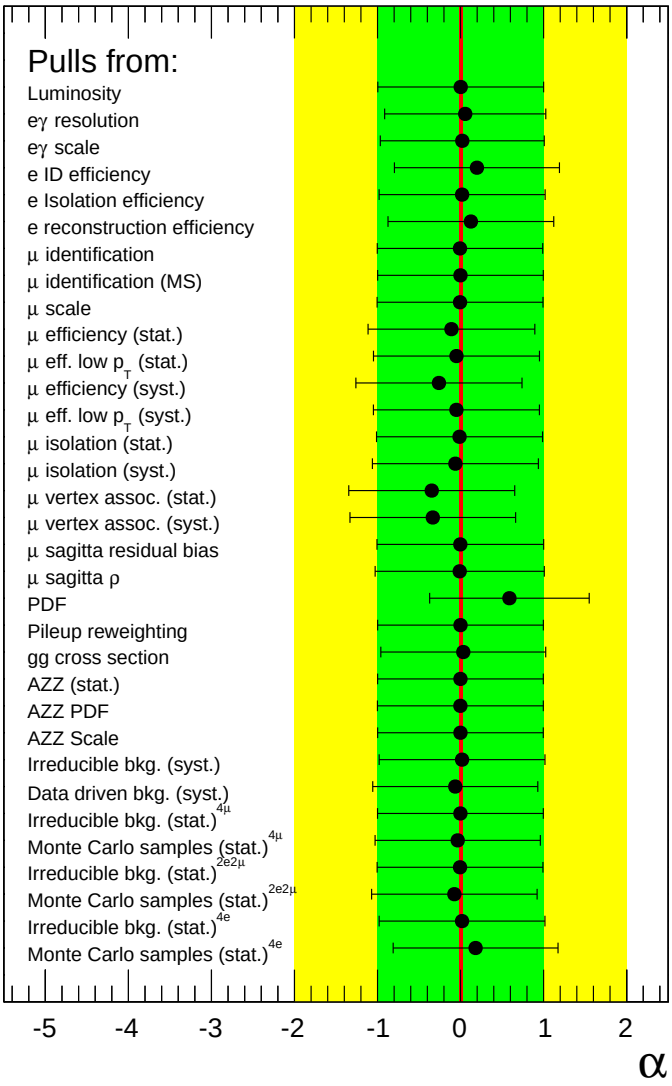

Figure 7.7: The nuisance parameters on the fit to the total cross section. The parameters are expected to be uniformly zero with an uncertainty of one. The uncertainty bands correspond to standard deviations of 1 (the width of the Gaussian which constrains the nuisance parameters) and 2.

when the mean fluctuates downwards. Therefore, the contribution to the total uncertainty introduced by a symmetric uncertainty is asymmetric.

The nuisance parameters in the total cross section fit, seen in fig. 7.7, all satisfy $|\alpha| < 1$. The largest α values are due to the distribution over channels (i.e. the excess in the $4e$ channel).

The observed fiducial cross section in the 4μ channel is lower than the expected cross section, despite the fact that the observed count in the 4μ channel is larger than the expected count (see fig. 6.1). This is due to the fact that the expected values for the counts and the cross sections are done with different predictions, SHERPA and MATRIX, respectively.

In the $4e$ channel, the observed data is higher than the expected value by $2.9\,\sigma$ $((obs - MC)/\sqrt{MC + \sigma^2(obs)})$ and this is reflected in the measurement of the $4e$ fiducial cross section being above the expected value. The largest uncertainty for the total cross section is the luminosity, at 3.5 %, followed by the statistical uncertainty, just above 3 %. In the fiducial cross sections, the statistical uncertainty is larger, reaching 6.5 % for the $4e$ channel.

The excess in the $4e$ channel has been studied in detail, but no reason for the excess has been found. If lepton universality is true, Z bosons decay equally to electrons and muons, making it unlikely that the excess is due to the $pp \to ZZ$ production.

Chapter 8

Anomalous triple gauge couplings

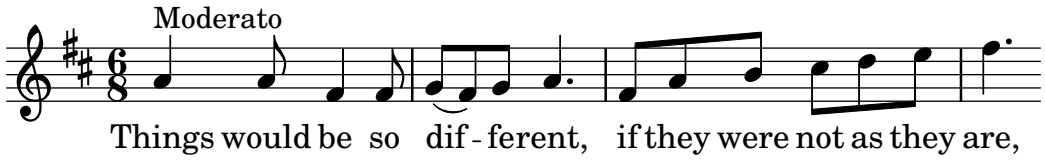

— Anna Russel, *1960*

This chapter describes studies of the anomalous neutral triple gauge couplings (aTGCs) discussed in section 2.3.1. Neutral triple gauge couplings are zero in the SM, but physics beyond the SM may give rise to non-zero triple gauge couplings. A likelihood model is constructed and used to find the compatibility of observed data and MC predictions. From this model, the most likely value of the coupling strengths can be measured. If the measured values of the couplings are consistent with the SM value of zero, limits can be set.

8.1 Introduction and Monte Carlo samples

As mentioned in chapter 2, neutral triple gauge couplings f_4^γ, f_4^Z, f_5^γ and f_5^Z, are all zero in the SM. As such, the search for processes with these couplings is a search for beyond SM physics. The kinematic properties of processes with and without the triple gauge couplings are different and can be used to search for evidence of non-zero couplings.

The method used in this thesis to set limits on the aTGCs works by comparing the distribution of the leading Z p_{T} in data and Monte Carlo (this variable was found to be the most sensitive, out of leading Z p_{T}, leading lepton p_{T} and invariant mass of the 4ℓ system [18]). A likelihood model is constructed, relating the observed data to MC predictions. From this likelihood, the most likely coupling strengths can be extracted. By comparing the best fit likelihood to the likelihood given a test value, limits on the coupling strengths can be set.

For this, a Monte Carlo prediction with variable aTGCs is required. Sherpa is able to generate $pp \to ZZ \to 4\ell$ events and cross sections with the anomalous couplings non-zero at LO. An "aTGC" sample with all four neutral triple gauge couplings set to 0.1 was generated (100 000 events), using the PDF set CT10. Most of this chapter uses that sample reweighted to the coupling strengths needed. An "SM" reference sample, generated in the same way but with the couplings all set to zero was used in fig. 2.3. The SM contribution was estimated in the same NLO Sherpa sample as used for chapter 4. Backgrounds were estimated using the methods in chapter 5.

In this analysis, the p_{T} of the leading Z candidate is used as differentiating variable. A histogram of that variable in truth MC can be seen in fig. 2.3, for a number of values of the variable f_4^γ. All lines in the plot use the same sample, reweighted using the method described in section 8.2, except for the line labelled SM, which uses the SM reference sample. The aTGC contribution is most prominent in the highest leading Z p_{T} bin (see fig. 2.3).

The reconstructed distribution of p_{T} of the leading Z boson can be seen in fig. 8.1. It shows that no excesses are seen in the high p_{T} region, where the aTGCs would be manifest.

Four p_{T} bins were considered, in the ranges [0,313], [313,607], [607,876] and [876,∞] GeV. The binning was chosen by setting f_4^γ to twice its expected limits from ref. [18], plotting the expected reconstructed leading Z p_{T} with 1 GeV bins and combining bins (starting with the highest) until the significance $\sigma = s/\sqrt{(s + b + \delta^2)}$ (where s is the signal, b is the SM contribution and δ is the systematic uncertainty) exceeds 5.0 or until

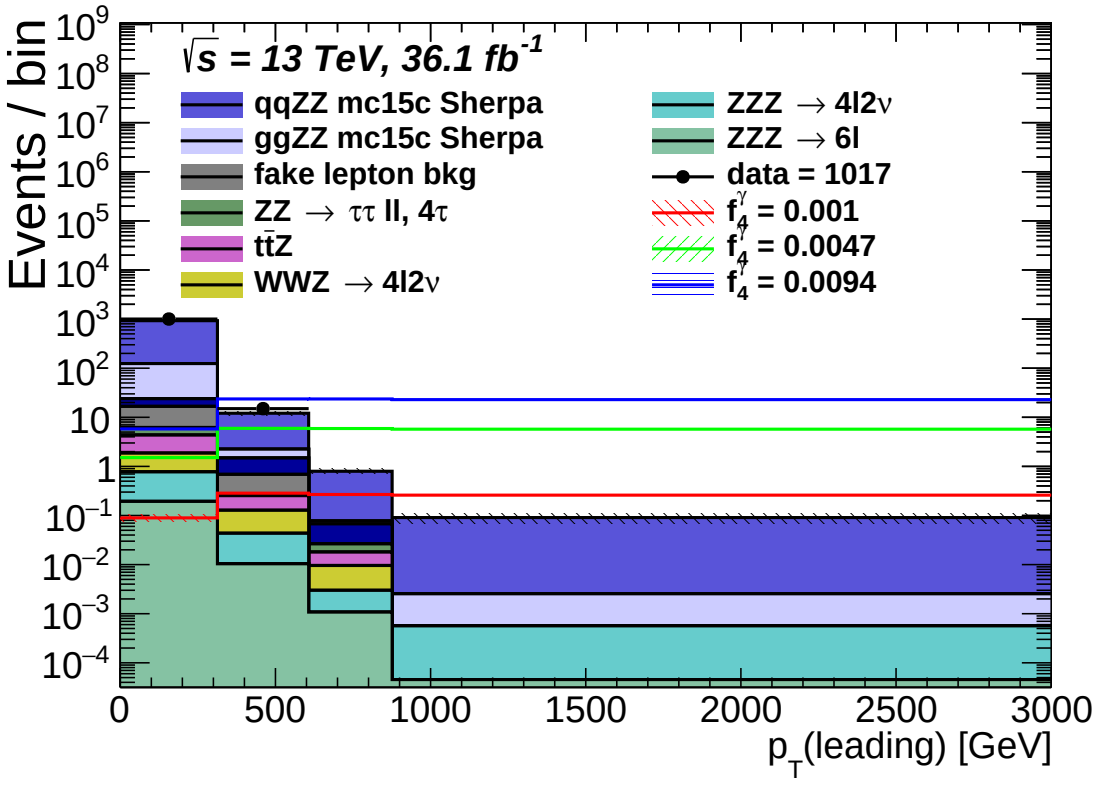

Figure 8.1: The distribution of reconstructed leading Z p_{T} as well as the predicted aTGC contribution for three values of f_4^γ (the limit from [18], twice that limit and 0.1, the other couplings turned off). The SM contribution is the same as in fig. 6.11 (except the bin sizes). Backgrounds are estimated using the methods in chapter 5. Total uncertainties are shown as error bands. This plot includes all decay channels. The number 1017 is the total number of observed events. The first bin has an observed count of 1002 and an SM expected value of 927 ± 56.

the combination of bins decreases the significance (this method was chosen to create exactly four bins, since more bins would be too CPU time consuming). Since the three highest p_{T} bins have relatively low backgrounds and low statistical MC uncertainty, the expected yield in each of these bins are approximately the same (the predicted aTGC yield in fig. 8.1 looks flat). The choice of binning was made without taking the observed yields into consideration.

The shape difference between fig. 8.1 and fig. 2.3 are due to the SM contribution having been removed from the aTGC lines and the choice of binning.

8.2 Yields and expected events

Similarly to eq. (2.16), the expected reconstructed counts in any bin can be written as

$$\begin{aligned} N_{exp} = & N_{00} + f_4^\gamma \ N_{01} + f_5^\gamma \ N_{02} + f_4^Z \ N_{03} + f_5^Z \ N_{04} \\ & + (f_4^\gamma)^2 N_{11} + f_5^\gamma f_4^\gamma N_{12} + f_4^Z f_4^\gamma N_{13} + f_5^Z f_4^\gamma N_{14} \\ & + (f_5^\gamma)^2 \ N_{22} + f_4^Z f_5^\gamma N_{23} + f_5^Z f_5^\gamma N_{24} \\ & + (f_4^Z \ )^2 N_{33} + f_5^Z f_4^Z N_{34} \\ & + (f_5^Z)^2 \ N_{44} \\ & + N_{DD} + N_{Irr}, \end{aligned} \tag{8.1}$$

where N_{exp} is the expected reconstructed count, f_i^V ($i = 4, 5$ and $V = Z, \gamma$) are the triple gauge couplings, N_{jk} are expected reconstructed yield contributions from different combinations of couplings and N_{DD} and N_{Irr} are the expected fake lepton and irreducible background rates. A LO Sherpa sample with all aTGCs set to 0.1 was generated (see section 8.1). The N_{jk} coefficients were determined by giving each MC event that passes the selection 16 weights (using eq. (2.15) and singling out the relevant contributions, a method from ref. [18]) representing the contribution to the 16 coefficients in eq. (8.1) and N_{jk} are the sums of those weights (for each term in eq. (8.1)). By setting the variables f_i^V to different values, N_{exp} can be reweighted to reflect the expected yield given those values of f_i^V. The N_{00} coefficient is the SM contribution and was replaced with a NLO Sherpa prediction.

8.3 Likelihood model

A likelihood model is constructed to compare the observed data to expected data as a function of the coupling strength.

Like in eq. (7.8), the statistical part of the likelihood is

$$L_{stat} = \prod_{bin} Pois(N_{obs}^{bin}, N_{exp}^{bin}), \tag{8.2}$$

where N_{obs}^{bin} is the observed reconstructed event count in each bin, N_{exp}^{bin} is the expected

reconstructed event count in each bin and $Pois(N_{obs}^{bin}, N_{exp}^{bin})$ is a Poisson distribution with the mean N_{exp}^{bin}, evaluated at N_{obs}^{bin}. The N_{jk} coefficients, the expected background yields and the integrated luminosity are given systematic uncertainties in the same way variables for the cross section extraction were (see section 7.2.1). The total likelihood is the product of L_{stat} and likelihood contributions from the uncertainties, like in eq. (7.10).

The coefficients N_{jk} can be seen in table 8.1.

The model is fitted to the observed distribution of p_{T} of the leading Z candidate in data and so a set of most likely coupling strengths can be extracted. Since no events are observed in the most sensitive bins, the most likely value of all couplings are zero.

8.4 Limit setting

Since the best fit value of the couplings are consistent with the SM, 1D limits on the couplings can be set (for each coupling). When considering only one coupling, that coupling is labelled μ and all other couplings are set to zero.

Once the fit has been performed and a best likelihood fit is obtained, a one sided test statistic Λ is used to quantify the compatibility between the data and any value of μ [83]. First, the *negative profile log likelihood* (PLL), is introduced. It is a simple measure of the disagreement between the model evaluated a given value of μ and the model evaluated at the best fit value of μ. It is defined as

$$PLL^{data}(\mu_{\mathrm{test}}) = -2\ln\left(\frac{L(\mu_{\mathrm{test}}, \theta_{\mathrm{test}}, data)}{L(\mu_{\mathrm{fit}}, \theta_{\mathrm{fit}}, data)}\right), \tag{8.3}$$

where μ_{test} is the value of μ at which Λ is to be evaluated and $data$ is the dataset it is fitted to (for instance observed data (obs), but pseudodata ($psData$) can also be used). $L(\mu_{\mathrm{test}}, \theta_{\mathrm{test}}, data)$ is the likelihood obtained by fitting the model to the dataset $data$ but not allowing μ to float in the fit (instead fixing it to μ_{test}). Similarly, μ_{fit} is the value of μ obtained by the unconstrained fit (without fixing μ) and $L(\mu_{\mathrm{fit}}, \theta_{\mathrm{fit}}, data)$ is the likelihood obtained by fitting the model to $data$ with μ unconstrained (this is equivalent to fixing μ to μ_{fit}). The θ_{test} and θ_{fit} are the sets of nuisance parameters from each fit (the "profile" in profile log likelihood means that θ_{test} is evaluated individually for each value of μ_{test}).

When $\mu_{\mathrm{fit}} = \mu_{\mathrm{test}}$, both likelihoods are the same and $PLL^{data}(\mu_{\mathrm{fit}}) = 0$.

p_T (leading) [GeV]	$[0-313]$		$[313-607]$		$[607-876]$		$[876-\infty]$	
N_{obs}	1002		15		0		0	
N_{SM}	911	$^{+55}_{-54}$	11	$^{+1}_{-1}$	0.779	$^{+0.104}_{-0.087}$	0.0905	$^{+0.0205}_{-0.0217}$
N_{01}	26.7	$^{+14.2}_{-13.4}$	19.6	$^{+5.2}_{-5.3}$	0.649	$^{+1.2}_{-0.944}$	0.73	$^{+0.657}_{-0.35}$
N_{02}	9.8	$^{+23.4}_{-23.5}$	15.2	$^{+5.2}_{-5.3}$	-0.33	$^{+1.26}_{-1.08}$	0.382	$^{+0.71}_{-0.435}$
N_{03}	-0.15	$^{+5.72}_{-5.71}$	0.936	$^{+0.73}_{-0.727}$	0.073	$^{+0.117}_{-0.131}$	-0.0404	$^{+0.0695}_{-0.0544}$
N_{04}	0.5	$^{+11.2}_{-11.4}$	0.89	$^{+1.08}_{-1.05}$	0.215	$^{+0.172}_{-0.183}$	-0.0054	$^{+0.0764}_{-0.0665}$
N_{11}	62700	$^{+5100}_{-4600}$	265000	$^{+17000}_{-17000}$	267000	$^{+23000}_{-22000}$	259000	$^{+24000}_{-23000}$
N_{12}	62900	$^{+4900}_{-4300}$	247000	$^{+16000}_{-16000}$	243000	$^{+20000}_{-20000}$	226000	$^{+21000}_{-20000}$
N_{13}	-4.08	$^{+2.54}_{-2.56}$	-4.95	$^{+6.81}_{-6.75}$	-8.61	$^{+7.45}_{-7.36}$	-2.73	$^{+6.49}_{-6.99}$
N_{14}	-2.22	$^{+1.53}_{-1.52}$	-1.3	$^{+2.59}_{-2.6}$	-3.75	$^{+3.25}_{-3.18}$	-0.07	$^{+2.61}_{-2.83}$
N_{22}	99100	$^{+7600}_{-6600}$	378000	$^{+24000}_{-24000}$	370000	$^{+30000}_{-30000}$	337000	$^{+31000}_{-30000}$
N_{23}	-2.41	$^{+1.56}_{-1.54}$	-1.41	$^{+2.61}_{-2.61}$	-3.76	$^{+3.27}_{-3.18}$	-0.08	$^{+2.61}_{-2.84}$
N_{24}	-7.6	$^{+5.46}_{-5.4}$	-2.92	$^{+7.66}_{-7.74}$	-11.2	$^{+10.3}_{-10.1}$	1.2	$^{+7.8}_{-8.7}$
N_{33}	58300	$^{+4800}_{-4300}$	263000	$^{+17000}_{-17000}$	267000	$^{+23000}_{-22000}$	260000	$^{+20000}_{-20000}$
N_{34}	58400	$^{+4500}_{-4000}$	244000	$^{+16000}_{-15000}$	243000	$^{+20000}_{-20000}$	227000	$^{+21000}_{-20000}$
N_{44}	92000	$^{+7000}_{-6000}$	373000	$^{+24000}_{-24000}$	370000	$^{+30000}_{-30000}$	340000	$^{+31000}_{-30000}$
N_{Irr}	6.19	± 1.88	0.28	± 0.09	0.027	± 0.012	0.0006	± 0.0003
N_{DD}	10	± 10	0.41	± 0.41	-0.012	± 0.012	-0.0003	± 0.0003
$N(0.0047)$	929	$^{+56}_{-55}$	17.6	$^{+1.2}_{-1.2}$	6.69	$^{+0.52}_{-0.49}$	5.82	$^{+0.53}_{-0.51}$

Table 8.1: The coefficients N_{jk} with total uncertainties. The N_{00} from the aTGC sample is not used, but is replaced by the N_{SM}, the SM contribution evaluated in the samples in chapter 4. The last line shows the expected counts for the case where $f_4^\gamma = 0.0047$ (and all other aTGCs set to zero, uncertainties added in quadrature).

The test statistic Λ is defined as [84]:

$$\Lambda^{data}(\mu_{\text{test}}) = \begin{cases} 0 & \text{if } (\mu_{\text{fit}} < \mu_{\text{test}} < 0) \\ 0 & \text{if } (0 < \mu_{\text{test}} < \mu_{\text{fit}}) \\ PLL^{data}(\mu_{\text{test}}) & \text{else} \end{cases}. \tag{8.4}$$

In the case that μ_{test} lies between 0 and μ_{fit}, Λ is set to zero, i.e. the model is considered fully consistent with data if $|\mu_{\text{test}}| < |\mu_{\text{fit}}|$ and both have the same sign (this is because failure of the fit with floating μ to converge to μ_{test} should not drive the disagreement between μ_{fit} and μ_{test}).

Pseudo experiments for a range of hypothetical coupling strengths μ_{test} are generated from the model (nuisance parameters are generated according to their likelihoods). A p-value is constructed as an estimate of the compatilibity between the observed data and a coupling strength μ_{test}. The p-value is defined as the fraction of pseudo experiments that have a higher $\Lambda^{psData}(\mu_{\text{test}})$ than $\Lambda^{obs}(\mu_{\text{test}})$:

$$p(\mu_{\text{test}}) = \frac{n_{\text{toys}}(\Lambda^{psData}(\mu_{\text{test}}) > \Lambda^{obs}(\mu_{\text{test}}))}{n_{\text{toys}}}, \tag{8.5}$$

where n_{toys} is the total number of toy experiments and $n_{\text{toys}}(\Lambda^{psData}(\mu_{\text{test}}) > \Lambda^{obs}(\mu_{\text{test}}))$ is the number of toy experiments with $\Lambda^{psData}(\mu_{\text{test}})$ greater than $\Lambda^{obs}(\mu_{\text{test}})$. Since Λ is non-negative and $\Lambda^{obs}(\mu_{\text{fit}}) = 0$, $p(\mu_{\text{fit}}) = 1$.

Examples of the PLL and $p(\mu_{\text{test}})$ can be seen in figs. 8.2 and 8.3.

The 95 % confidence limit CL_s is the coupling strength μ_{limit} such that the p-value is 5 % ($p(\mu_{\text{limit}}) = 0.05$). Two such μ_{limit} are present, in the positive and negative directions, respectively. The limit was estimated by interpolating linearly between the adjacent points in figs. 8.2 and 8.3 and finding the point that crosses over the 5 % line.

In simpler terms, consider a pseudo experiment taking place in a pseudo universe in which μ has a given value μ_{test}. In that universe, $p(\mu_{\text{test}})$ is the probability that the experiment generates a dataset which has a higher likelihood than our observed data has. If $p(\mu_{\text{test}})$ is less than 5 %, that universe is excluded with a 95 % confidence.

8.5 Asymptotic estimates

There exists an asymptotic equation that predicts that $\Lambda^{obs}(\mu_{\text{limit}}) = 1.92$ [85]. For comparison, figs. 8.2 and 8.3 also include lines representing the PLL values at the limits. These lines are not fully consistent with the asymptotic estimate due to backgrounds

and asymmetric N_{jk} coefficients. However, the aymptotic equation is much faster at setting the limits. Some parts of this analysis cannot be done using the pseudo experiment method (due to CPU time constraints) but can be done using asymptotic limit setting.

Histograms of the asymptotic limits (upwards and downwards) for pseudo experiments generated with all coupling strengths set to zero can be seen in figs. 8.4 and 8.5. A faint repeated peak-like structure within each plot is due to the limited number of events generated in the highest p_{T} bin (the most significant bin). If the SM is excluded for a pseudo experiment (which happens in 5 % of pseudo experiments) the limit setting breaks down and both the upper and lower limit is on the same side of 0. This can be seen as a small bump in the plots. The measured limits are also seen in these plots as vertical lines (see table 8.2). The measured limits are tight compared to the distributions seen in figs. 8.4 and 8.5, due to the yields in the most sensitive bins being zero.

Two dimensional limits are also set using asymptotic limits, by using Λ as a function of two couplings and finding the contour at which $\Lambda = 1.92$. These plots, for each combination of two couplings f_i^V can be seen in fig. 8.6 (the other two couplings set to zero).

8.6 Results

Using the method above, all anomalous gauge couplings were found to be consistent with the SM. The 95 % confidence limits on the couplings can be found in table 8.2.

coupling	95 % confidence interval
f_4^γ	$-0.0017 < f_4^\gamma < 0.0018$
f_5^γ	$-0.0017 < f_5^\gamma < 0.0018$
f_4^Z	$-0.0016 < f_4^Z < 0.0016$
f_5^Z	$-0.0016 < f_5^Z < 0.0016$

Table 8.2: Measured 95 % confidence intervals of anomalous triple gauge couplings.

The results are an improvement by a factor approximately 2 from the ATLAS results from the analysis performed on 2012 data [18]. The results are consistent with the SM and remain approximately symmetric around zero.

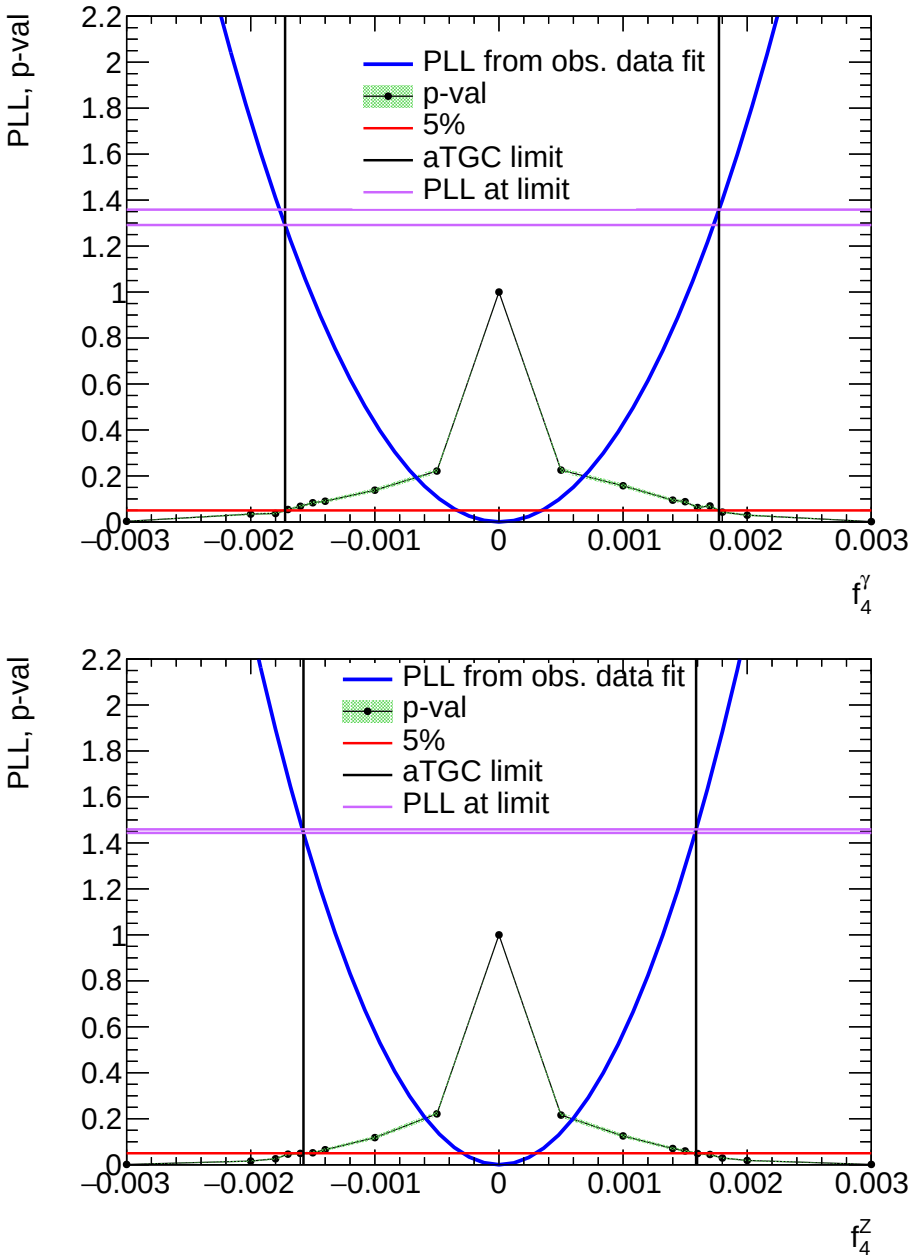

Figure 8.2: The negative profile log likelihood (PLL) as a function of f_4^γ and f_4^Z. The p-value is also seen, estimated in pseudo experiments, as a function of the value of f_4^V at which the pseudo experiments were generated (statistical uncertainty in error bands). The figure also shows the 5 % CL_s cut off, as well as the value of the PLL at the limit.

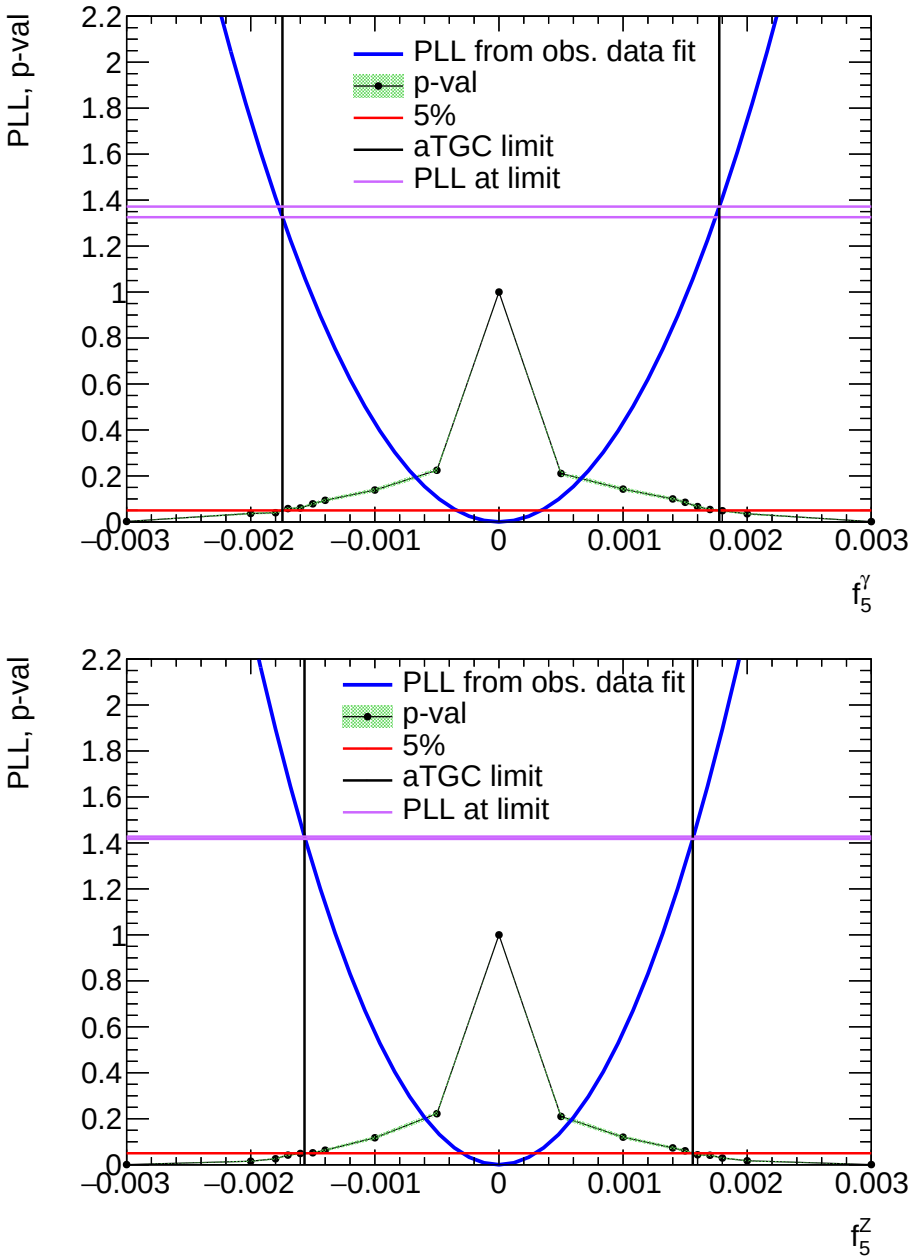

Figure 8.3: The negative profile log likelihood (PLL) as a function of f_5^γ and f_5^Z. The p-value is also seen, estimated in pseudo experiments, as a function of the value of f_5^V at which the pseudo experiments were generated (statistical uncertainty in error bands). The figure also shows the 5 % CL_s cut off, as well as the value of the PLL at the limit.

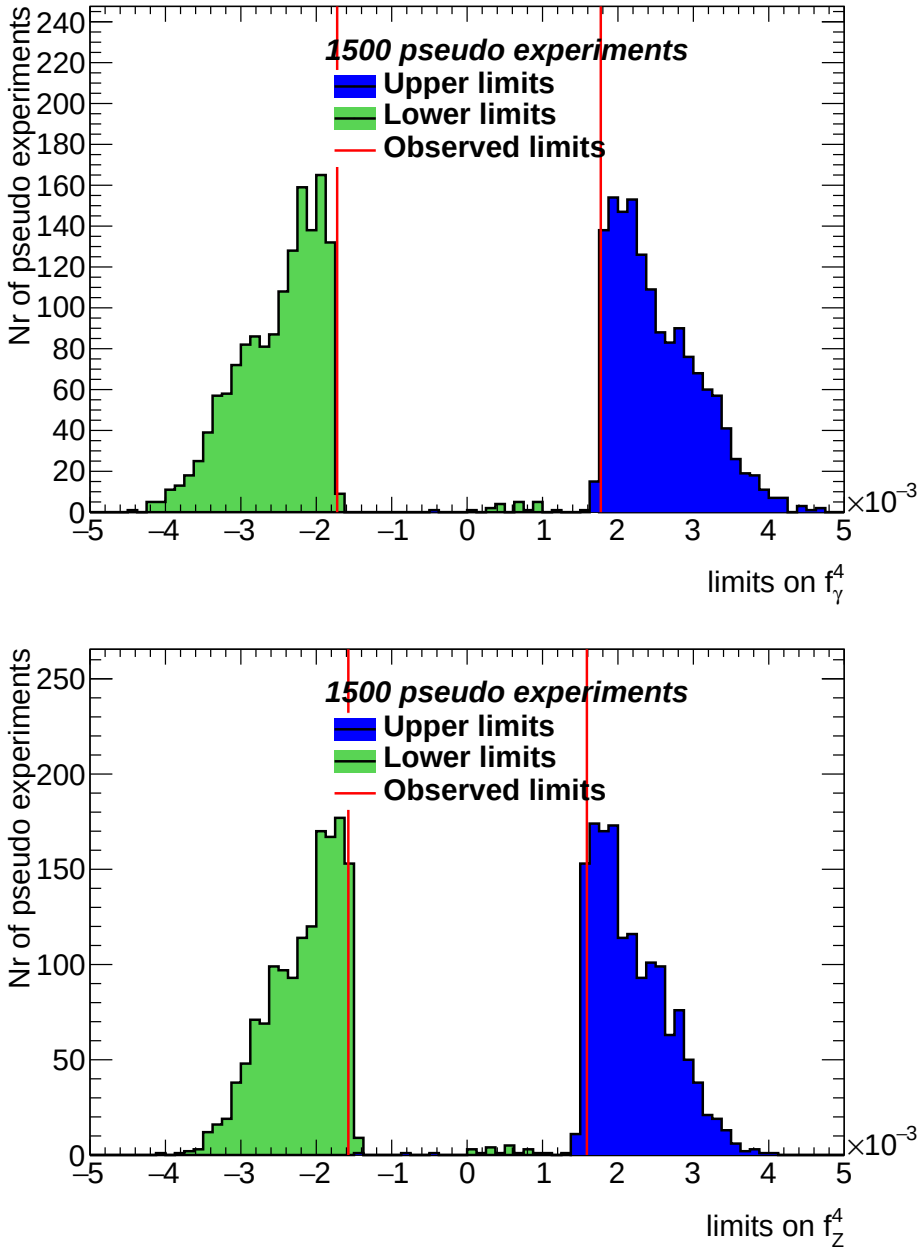

Figure 8.4: The asymptotic limits (upwards and downwards) for pseudo experiments generated with all coupling strengths set to zero, as a function of the couplings f_4^γ and f_4^Z. The measured limits are also shown.

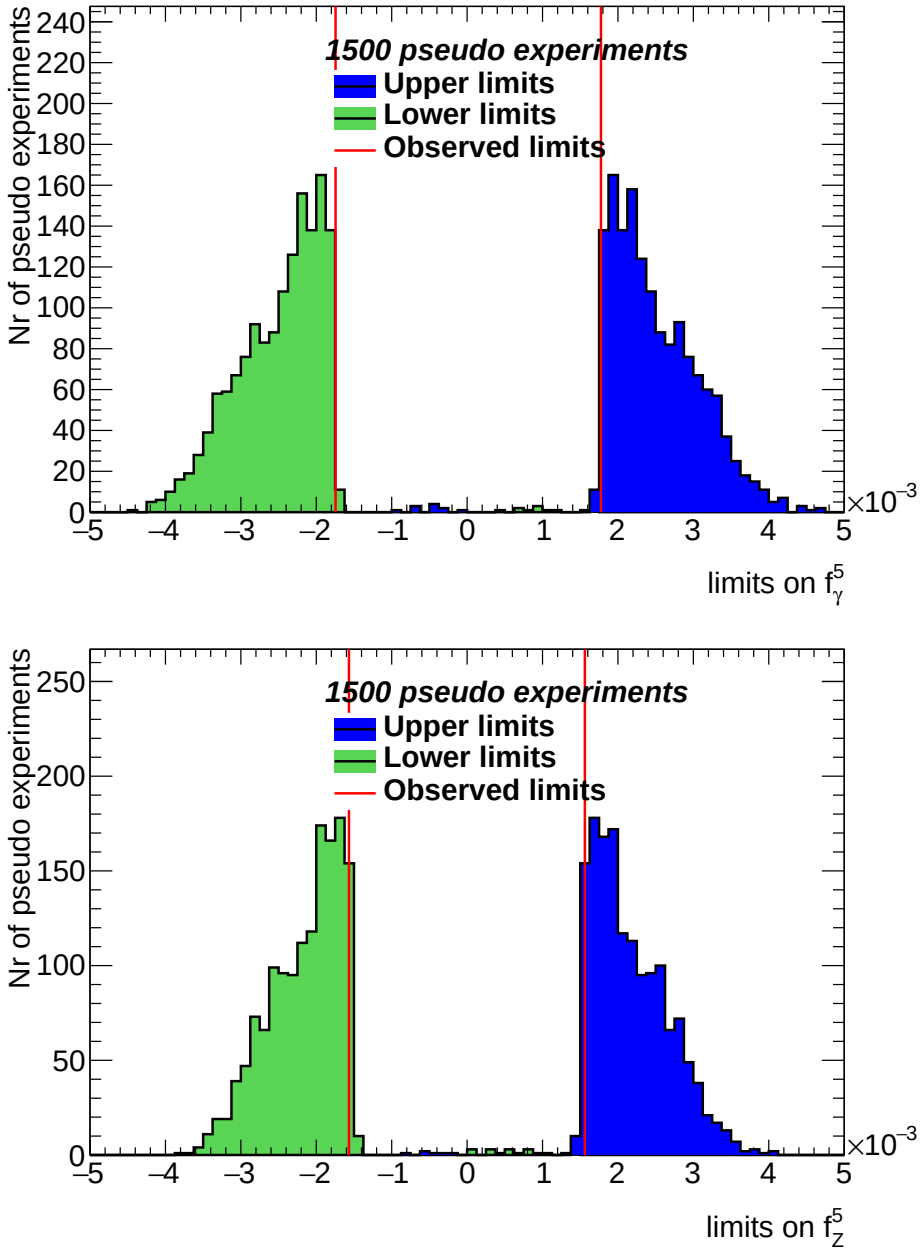

Figure 8.5: The asymptotic limits (upwards and downwards) for pseudo experiments generated with all coupling strengths set to zero, as a function of the couplings f_5^γ and f_5^Z. The measured limits are also shown.

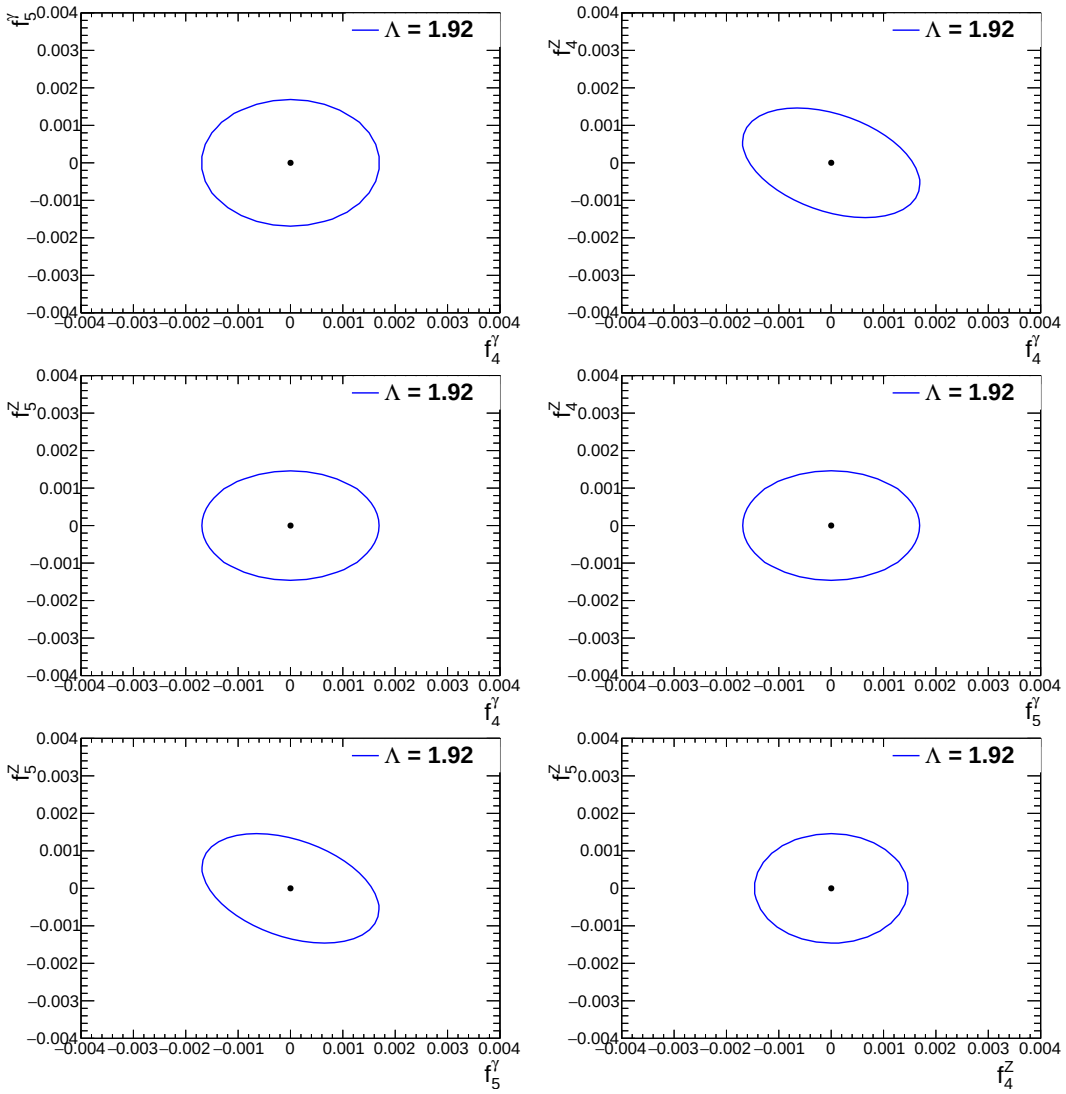

Figure 8.6: The 2D contours of $2 * PLL = 1.92$ as a function of every combination of two f_i^V variables, which is the limit of those variables in the asymptotic limit. The f_4^γ and f_4^Z variables are correlated, as are f_5^γ and f_5^Z. This is due to the shape of eq. (2.15).

As an estimate of the statistical contribution to the limits, the same procedure was carried out without adding systematic uncertainties to the likelihood model. The results can be seen in figs. 8.7 and 8.8. The limits found can be seen in table 8.3 and show that the limits are statistically dominated. Some limits are found, counterintuitively, to be looser than the limits with all uncertainties included. This is due to the excess in the lowest bin. Without systematic uncertainties, the model concludes that the excess may be due to a non-zero aTGC. When uncertainties are introduced, the model concludes that some of the excess is due to the uncertainties, which means the model can relax the likelihood of non-zero aTGCs.

coupling	95 % confidence interval
f_4^γ	$-0.0018 < f_4^\gamma < 0.0018$
f_5^γ	$-0.0018 < f_5^\gamma < 0.0018$
f_4^Z	$-0.0016 < f_4^Z < 0.0016$
f_5^Z	$-0.0016 < f_5^Z < 0.0016$

Table 8.3: Measured 95 % confidence intervals of anomalous triple gauge couplings, using a model with no systematic uncertainties.

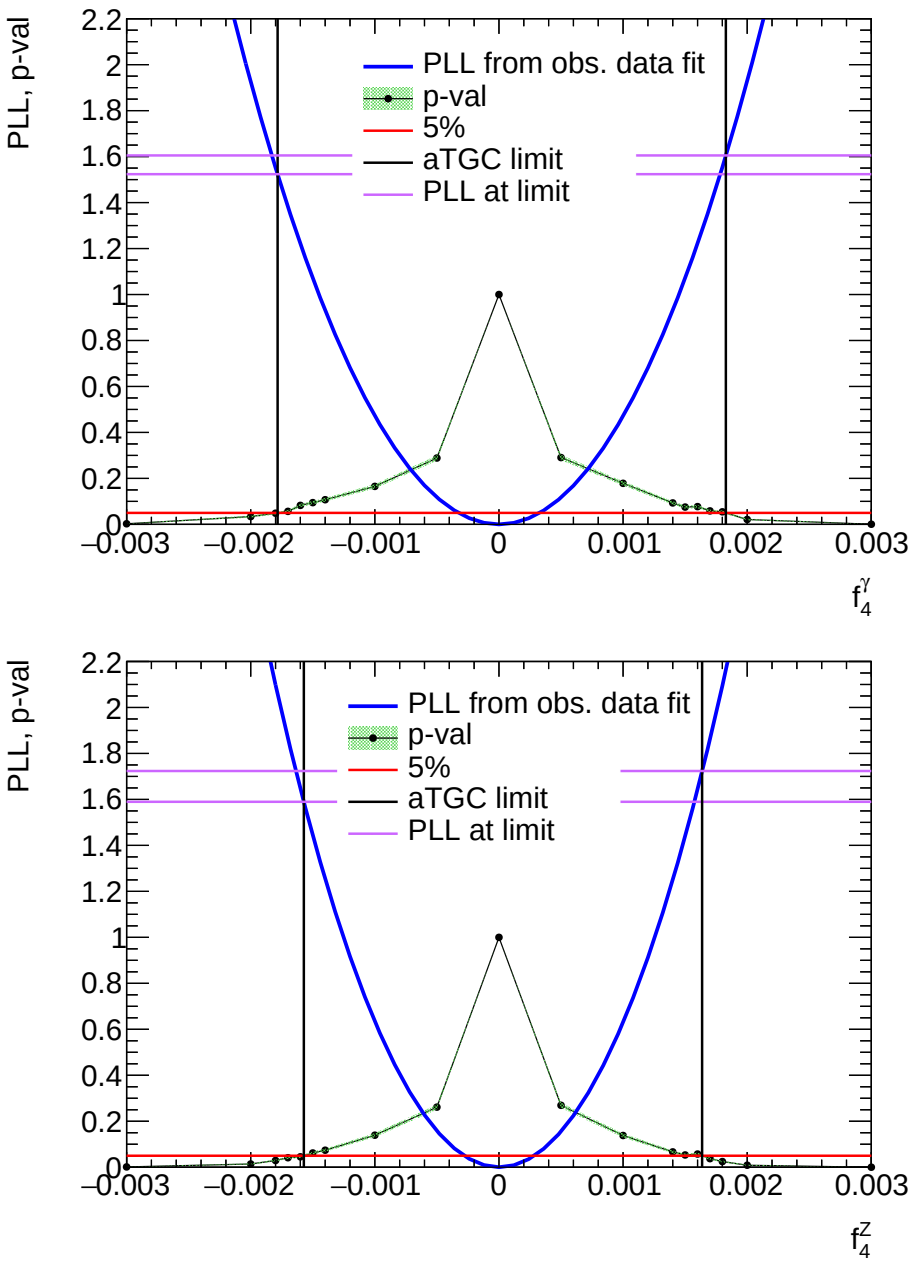

Figure 8.7: The negative profile log likelihood (PLL) as a function of f_4^γ and f_4^Z in a model with no systematic uncertainties. The p-value is also seen, estimated in pseudo experiments, as a function of the value of f_4^V at which the pseudo experiments were generated (statistical uncertainty in error bands). The figure also shows the 5 % CL_s cut off, as well as the value of the PLL at the limit (two horizontal lines, one for the positive limit and one for the negative limit).

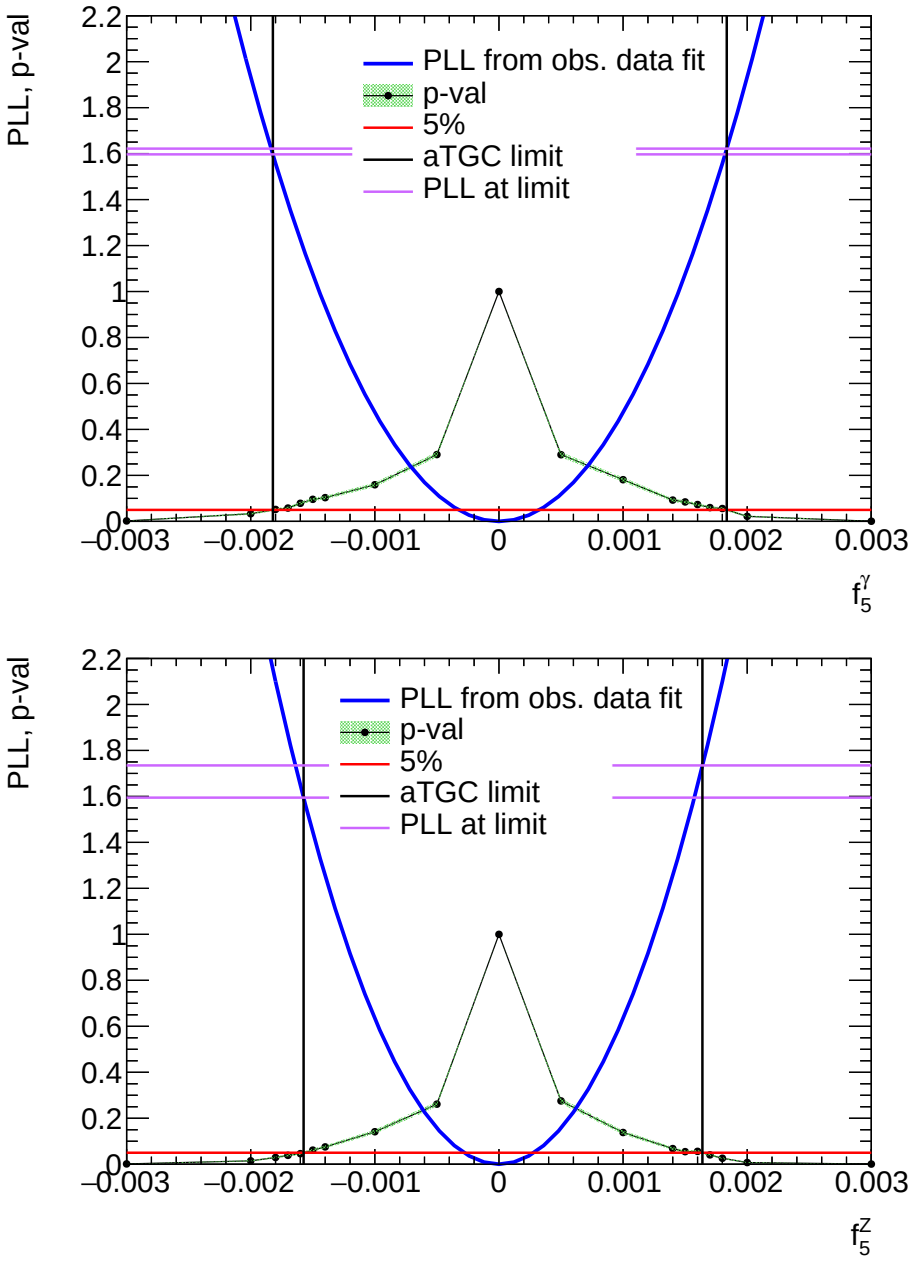

Figure 8.8: The negative profile log likelihood (PLL) as a function of f_5^γ and f_5^Z in a model with no systematic uncertainties. The p-value is also seen, estimated in pseudo experiments, as a function of the value of f_5^V at which the pseudo experiments were generated (statistical uncertainty in error bands). The figure also shows the 5 % CL_s cut off, as well as the value of the PLL at the limit (two horizontal lines, one for the positive limit and one for the negative limit).

Chapter 9

Conclusions

In 2015 and 2016, the ATLAS detector recorded 36.1 fb^{-1} of data useful for physics at a centre-of-mass energy of $\sqrt{s} = 13\,\text{TeV}$. The ATLAS collaboration has analysed the resulting data to make precision measurements of processes in the Standard Model of particle physics (SM), as well as to search for physics beyond the SM. In this thesis is presented the analysis of the $pp \to ZZ \to 4\ell$ process ($66\,\text{GeV} < m_Z < 116\,\text{GeV}$). This process is used to test the Standard Model, both by comparing Standard Model cross section predictions to observed values of the cross sections and by searching for non-zero neutral triple gauge couplings, which are zero in the SM.

In the 36.1 fb^{-1} of $\sqrt{s} = 13\,\text{TeV}$ data, 1017 events were selected, using a selection designed to identify $ZZ \to 4\ell$ events (two opposite charge, same flavour lepton pairs). Background events were predicted to contribute approximately 2 % of the selected sample.

Four fiducial cross sections (in a fiducial region closely matching the detector acceptance) were measured: one for each channel ($4e$, $2e2\mu$, 4μ) and one in the union of these regions. The cross section was also extracted to a total cross section, ($66\,\text{GeV} < m_Z < 116\,\text{GeV}$, regardless of decay channel) and was found to be

$$\sigma^{total} = 16.5^{+0.5}_{-0.5}(\text{stat.})^{+0.4}_{-0.4}(\text{syst.})^{+0.5}_{-0.5}(\text{lumi.})\ \text{pb}, \tag{9.1}$$

which is consistent with an NNLO SM prediction of $16.9^{+0.6}_{-0.5}$ pb. It is also consistent with previous measurements of the cross section at 13 TeV from ATLAS ($16.7\ ^{+2.6}_{-2.2}$ pb) and CMS ($17.8\ ^{+1.1}_{-1.1}$ pb).

An excess is observed in the $4e$ channel. No definite explanation was found for this excess, it could be due to new physics (lepton universality violation) but further study

would be required to confirm this.

Anomalous triple gauge couplings (aTGCs), which are zero in the SM, are introduced by an effective vertex factor, parameterised by four coupling strengths f_i^V ($V = \gamma, Z$, $i = 4, 5$). The couplings were analysed by comparing a distribution of events over the transverse momentum of the Z boson candidate with the highest transverse momentum to Monte Carlo predictions with and without non-zero aTGCs present. The resulting coupling measurements were consistent with the SM values of zero and the measured 95 % $\mathrm{CL_s}$ confidence limits are shown in table 9.1.

coupling	95 % confidence interval
f_4^γ	$-0.0017 < f_4^\gamma < 0.0018$
f_5^γ	$-0.0017 < f_5^\gamma < 0.0018$
f_4^Z	$-0.0016 < f_4^Z < 0.0016$
f_5^Z	$-0.0016 < f_5^Z < 0.0016$

Table 9.1: Measured limits on aTGCs.

These limits are an improvement on a previous ATLAS measurement by approximately a factor of two and are comparable to previous measurements from CMS.

The leading uncertainty on the cross sections as well as the aTGC limits are statistical, suggesting that future analyses with larger luminosity (or acceptance) will improve the measurements further. Improvement of the luminosity uncertainty would also have a significant impact on the results. The LHC will continue to take data through 2018 and will be upgraded to receive much larger integrated luminosities (up to 3000 fb^{-1}, reducing the statistical uncertainty to approximately a tenth of its current size, making it no longer the dominant uncertainty). There is also the possibility of future colliders, such as CLIC and future circular colliders, which will be able to probe different energies with more data. Future data taking, at the LHC and elsewhere, will improve the measurements presented in this thesis.

Appendices

Appendix A

Meta analysis

This appendix shows the progress of this thesis as a function of time. It is automatically generated when the author uploads the progress to the version control software `svn`.

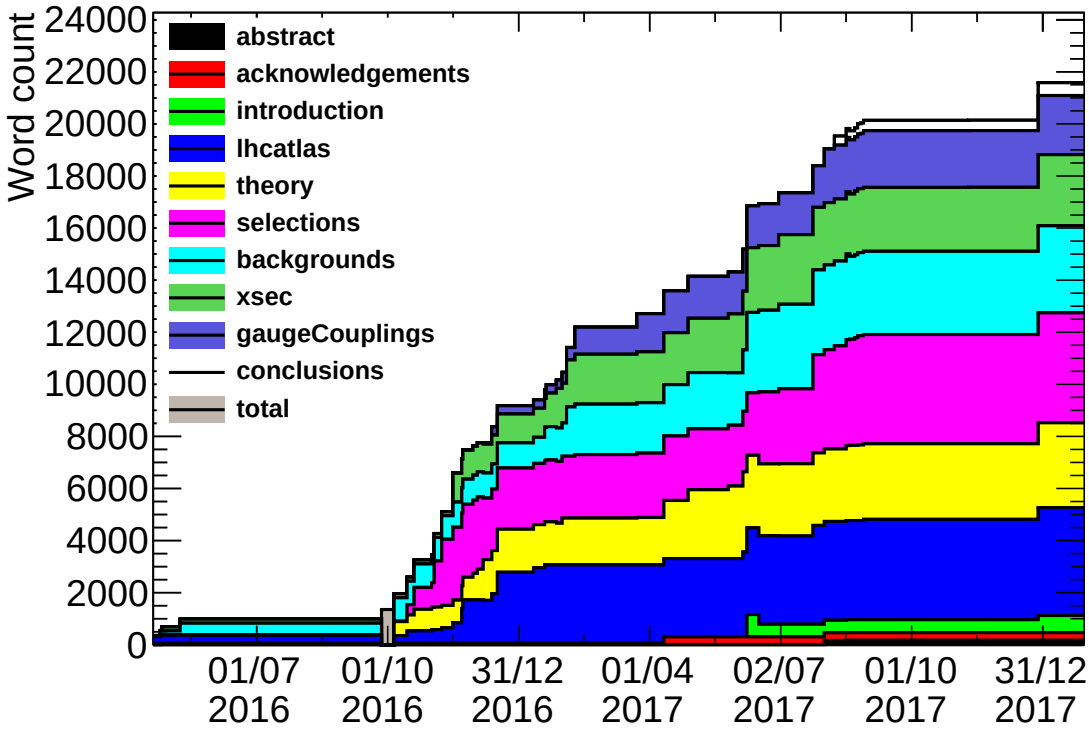

Figure A.1: Plot of the word count progress of this thesis as a fuction of time, with a breakdown into chapters. The gray area represents a time from which the chapter breakdown has been lost.

Bibliography

[1] ATLAS Collaboration, G. Aad et al., *The ATLAS Experiment at the CERN Large Hadron Collider*, Journal of Instrumentation **3** (2008) S08003.

[2] L. Evans and P. Bryant, *LHC Machine*, Journal of Instrumentation **3** (2008) S08001.

[3] M. E. Peskin and D. V. Schroeder, *An introduction to quantum field theory*. Westview Press Reading (Mass.), 1995.

[4] D. J. Griffiths, *Introduction to elementary particles; 2nd rev. version*. Wiley, New York, NY, 2008. `https://cds.cern.ch/record/111880`.

[5] ATLAS Collaboration, G. Aad et al., *Observation of a new particle in the search for the Standard Model Higgs boson with the ATLAS detector at the LHC*, Physics Letters **B716** (2012) 1, `arXiv:1207.7214`.

[6] CMS Collaboration, S. Chatrchyan et al., *Observation of a new boson at a mass of 125 GeV with the CMS experiment at the LHC*, Physics Letters **B716** (2012) 30, `arXiv:1207.7235`.

[7] J. Schechter and J. W. F. Valle, *Neutrino Masses in SU(2) $\bigotimes$ U(1) Theories*, Physical Review **D22** (1980) 2227.

[8] J. C. Kapteyn, *First Attempt at a Theory of the Arrangement and Motion of the Sidereal System*, Astrophysical Journal **55** (1922) 302.

[9] K. A. Olive (Particle Data Group), *Review of Particle Physics*, Chinese Physics **C40** (2016) no. 10, 1.

[10] G. 't Hooft, *Naturalness, chiral symmetry, and spontaneous chiral symmetry breaking*, NATO Sci. Ser. B **59** (1980) 135.

[11] N. Arkani-Hamed, S. Dimopoulos, and G. R. Dvali, *The Hierarchy problem and new dimensions at a millimeter*, Physics Letters **B429** (1998) 263, arXiv:hep-ph/9803315.

[12] C. Rovelli, *Notes for a brief history of quantum gravity*, in *Recent developments in theoretical and experimental general relativity, gravitation and relativistic field theories. Proceedings, 9th Marcel Grossmann Meeting, MG'9, Rome, Italy, July 2-8, Pts. A-C*, p. 742. 2000. arXiv:gr-qc/0006061.

[13] S. P. Martin, *A Supersymmetry primer*, Advanced Series on Directions in High Energy Physics **18** (1997) 1, arXiv:hep-ph/9709356.

[14] ATLAS Collaboration, G. Aad et al., *Measurement of the ZZ Production Cross Section in pp Collisions at $\sqrt{s}$ = 13 TeV with the ATLAS Detector*, Physical Review Letters **116** (2016) no. 10, 101801, arXiv:1512.05314.

[15] S. Richter, M. Becker, W. Buttinger, C. Geng, K. Kordas, A. Leisos, E. Nurse, O. Penc, J. Rosten, E. Skorda, and B. Zhou, *Differential fiducial ZZ cross section measurement in 13 TeV pp collisions with the ATLAS detector — paper draft: Paper draft for iterating with conveners and EB*, Tech. Rep. ATL-COM-PHYS-2017-241, CERN, Geneva, 2017. https://cds.cern.ch/record/2255322.

[16] ATLAS Collaboration, G. Aad et al., *Measurement of $W^{\pm}$ and Z-boson production cross sections in pp collisions at $\sqrt{s} = 13$ TeV with the ATLAS detector*, Physics Letters **B759** (2016) 601, arXiv:1603.09222.

[17] U. Baur and D. Rainwater, *Probing neutral gauge boson self-interactions in* ZZ *production at hadron colliders*, Physical Review D **62** (2000) 113011, arXiv:hep-ph/0008063.

[18] ATLAS Collaboration, M. Aaboud et al., *Measurement of the ZZ production cross section in proton-proton collisions at $\sqrt{s}$ = 8 TeV using the $ZZ \to \ell^-\ell^+\ell'^-\ell'^+$ and $ZZ \to \ell^-\ell^+\nu\bar{\nu}$ channels with the ATLAS detector*, Journal of High Energy Physics **01** (2017) 99, arXiv:1610.07585.

[19] CMS Collaboration, V. Khachatryan et al., *Measurement of the $pp \to ZZ$ production cross section and constraints on anomalous triple gauge couplings in*

four-lepton final states at $\sqrt{s}$ *=8 TeV*, Phys. Lett. **B740** (2015) 250, arXiv:1406.0113.

[20] G. Dissertori, A. Gehrmann-DeRidder, T. Gehrmann, E. W. N. Glover, G. Heinrich, and H. Stenzel, *Precise Determination of the Strong Coupling Constant at NNLO in QCD from the Three-Jet Rate in Electron-Positron Annihilation at LEP*, Physical Review Letters **104** (2010) 72002, arXiv:0910.4283.

[21] T. Gleisberg, S. Hoche, F. Krauss, M. Schonherr, S. Schumann, et al., *Event generation with SHERPA 1.1*, Journal of High Energy Physics **02** (2009) 7, arXiv:0811.4622.

[22] F. Cascioli, S. Höche, F. Krauss, P. Maierhöfer, S. Pozzorini, and F. Siegert, *Precise Higgs-background predictions: merging NLO QCD and squared quark-loop corrections to four-lepton + 0,1 jet production*, Journal of High Energy Physics **01** (2014) 46, arXiv:1309.0500.

[23] F. Caola, K. Melnikov, R. Röntsch, and L. Tancredi, *QCD corrections to ZZ production in gluon fusion at the LHC*, Physical Review D **92** (2015) 94028, arXiv:1509.06734.

[24] M. Grazzini, S. Kallweit, and D. Rathlev, *ZZ production at the LHC: Fiducial cross sections and distributions in NNLO QCD*, Physics Letters B **750** (2015) 407, arXiv:1507.06257.

[25] NNPDF Collaboration, R. D. Ball et al., *Parton distributions for the LHC Run II*, Journal of High Energy Physics **04** (2015) 40, arXiv:1410.8849.

[26] B. Biedermann, A. Denner, S. Dittmaier, L. Hofer, and B. Jager, *Next-to-leading-order electroweak corrections to the production of four charged leptons at the LHC*, Journal of High Energy Physics **01** (2017) 33, arXiv:1611.05338.

[27] B. Biedermann, A. Denner, S. Dittmaier, L. Hofer, and B. Jäger, *Electroweak corrections to* $pp \to \mu^+\mu^- e^+ e^- + X$ *at the LHC: a Higgs background study*, Physical Review Letters **116** (2016) no. 16, 161803, arXiv:1601.07787.

[28] CMS Collaboration, S. Chatrchyan et al., *The CMS Experiment at the CERN LHC*, Journal of Instrumentation **3** (2008) S08004.

[29] CMS Collaboration, A. M. Sirunyan et al., *Measurements of the pp→ZZ production cross section and the Z→ 4ℓ branching fraction, and constraints on anomalous triple gauge couplings at* $\sqrt{s} = 13\ TeV$, `arXiv:1709.08601`.

[30] CMS Collaboration, V. Khachatryan et al., *Measurement of the ZZ production cross section and* $Z \to \ell^+\ell^-\ell'^+\ell'^-$ *branching fraction in pp collisions at* $\sqrt{s} = 13\ TeV$, Phys. Lett. **B763** (2016) 280, `arXiv:1607.08834`.

[31] ATLAS Collaboration, *Measurement of ZZ production in pp collisions at* $\sqrt{s}$*=7 TeV and limits on anomalous ZZZ and ZZ*γ *couplings with the ATLAS detector*, Journal of High Energy Physics **03** (2012) 128, `arXiv:1211.6096`.

[32] CMS Collaboration, S. Chatrchyan et al., *Measurement of the ZZ production cross section and search for anomalous couplings in* $2\ell 2\ell'$ *final states in pp collisions at* $\sqrt{s} = 7\ TeV$, Journal of High Energy Physics **01** (2013) 63, `arXiv:1211.4890`.

[33] ALEPH Collaboration, DELPHI Collaboration, L3 Collaboration, OPAL Collaboration, LEP Electroweak Working Group, *A combination of preliminary LEP electroweak measurements and constraints on the standard model*, Tech. Rep. CERN-PPE-95-172. CERN-L3-088, CERN, Geneva, Nov, 1995. `https://cds.cern.ch/record/293395`. Preprint not submitted to publication.

[34] CERN, *The accelerator complex*, Online, 2015. `http://home.web.cern.ch/about/accelerators`. [accessed 18-March-2015].

[35] C. Lefèvre, *The CERN accelerator complex. Complexe des accelerateurs du CERN*, Online, 2008. `http://cds.cern.ch/record/1260465`. [accessed 19-March-2015].

[36] ALICE Collaboration, K. Aamodt et al., *The ALICE experiment at the CERN LHC*, Journal of Instrumentation **3** (2008) S08002.

[37] LHCb Collaboration, A. A. Alves, Jr. et al., *The LHCb Detector at the LHC*, Journal of Instrumentation **3** (2008) S08005.

[38] ATLAS Collaboration, *Luminosity Public Results Run2*, Online, 2016. `https://twiki.cern.ch/twiki/bin/view/AtlasPublic/LuminosityPublicResultsRun2`. [Online; accessed 27-Nov-2017].

[39] ATLAS Collaboration, M. Aaboud et al., *Luminosity determination in pp collisions at $\sqrt{s}$ = 8 TeV using the ATLAS detector at the LHC*, European Physical Journal **C76** (2016) no. 12, 653, `arXiv:1608.03953`.

[40] G. Apollinari, O. Brüning, T. Nakamoto, and L. Rossi, *High Luminosity Large Hadron Collider HL-LHC*, CERN Yellow Report (2015) no. 5, 1, `arXiv:1705.08830`.

[41] ATLAS Collaboration, *ATLAS inner detector: Technical Design Report, 1*. Technical Design Report ATLAS. CERN, Geneva, 1997. `https://cds.cern.ch/record/331063`.

[42] M. Capeans, G. Darbo, K. Einsweiller, M. Elsing, T. Flick, M. Garcia-Sciveres, C. Gemme, H. Pernegger, O. Rohne, and R. Vuillermet, *ATLAS Insertable B-Layer Technical Design Report*, Tech. Rep. CERN-LHCC-2010-013. ATLAS-TDR-19, 2010. `https://cds.cern.ch/record/1291633`.

[43] ATLAS Collaboration, Y. Takubo, *The Pixel Detector of the ATLAS experiment for the Run2 at the Large Hadron Collider*, Journal of Instrumentation **10** (2015) no. 02, 1, `arXiv:1411.5338`.

[44] ATLAS Collaboration, *Operation and performance of the ATLAS semiconductor tracker*, Journal of Instrumentation **9** (2014) 8009, `arXiv:1404.7473`.

[45] ATLAS Collaboration, A. S. Boldyrev et al., *The ATLAS transition radiation tracker*, Instruments and Experimental Techniques **55** (2012) 323.

[46] ATLAS Collaboration, *ATLAS liquid-argon calorimeter: Technical Design Report*. Technical Design Report ATLAS. CERN, Geneva, 1996. `https://cds.cern.ch/record/331061`.

[47] ATLAS Collaboration, *ATLAS tile calorimeter: Technical Design Report*. Technical Design Report ATLAS. CERN, Geneva, 1996. `http://cds.cern.ch/record/331062`.

[48] ATLAS Collaboration, N. Nikiforou, *Performance of the ATLAS Liquid Argon Calorimeter after three years of LHC operation and plans for a future upgrade*, in *Proceedings, 3rd International Conference on Advancements in Nuclear Instrumentation Measurement Methods and their Applications (ANIMMA 2013): Marseille, France, June 23-27, 2013*. 2013. arXiv:1306.6756.

[49] ATLAS Collaboration, J. Benitez, *Performance of the ATLAS Liquid Argon Calorimeters in LHC Run-1 and Run-2*, 2016. https://cds.cern.ch/record/2153383.

[50] M. Mlynarikova, *Performance of the ATLAS hadronic Tile calorimeter*, in *5th Large Hadron Collider Physics Conference (LHCP 2017) Shanghai, China*. 2017. arXiv:1709.00100.

[51] ATLAS Collaboration, G. Aad et al., *Muon reconstruction performance of the ATLAS detector in proton–proton collision data at $\sqrt{s}$ =13 TeV*, vol. C76, p. 292. 2016. arXiv:1603.05598.

[52] ATLAS Collaboration, M. Aaboud et al., *Luminosity determination in pp collisions at $\sqrt{s}$ = 8 TeV using the ATLAS detector at the LHC*, Eur. Phys. J. **C76** (2016) no. 12, 653, arXiv:1608.03953.

[53] ATLAS Collaboration, *ATLAS Twiki: Luminosity for physics*, https://twiki.cern.ch/twiki/bin/viewauth/Atlas/LuminosityForPhysics. accessed: 2017-02-24.

[54] ATLAS Collaboration, M. Aaboud et al., *Performance of the ATLAS Trigger System in 2015*, Eur. Phys. J. **C77** (2017) no. 5, 317, arXiv:1611.09661.

[55] Ruiz-Martinez, Aranzazu and ATLAS Collaboration, *The Run-2 ATLAS Trigger System*, Tech. Rep. ATL-DAQ-PROC-2016-003, CERN, Geneva, 2016. https://cds.cern.ch/record/2133909.

[56] ATLAS Collaboration, *Performance of the ATLAS Inner Detector Track and Vertex Reconstruction in the High Pile-Up LHC Environment*, Tech. Rep. ATLAS-CONF-2012-042, CERN, Geneva, 2012. https://cds.cern.ch/record/1435196.

[57] G. Piacquadio, K. Prokofiev, and A. Wildauer, *Primary vertex reconstruction in the ATLAS experiment at LHC*, Journal of Physics: Conference Series **119** (2008) no. 3, 032033. http://stacks.iop.org/1742-6596/119/i=3/a=032033.

[58] M. R. Devesa, D. Boerner, et al., *Supporting note for the Minimum Bias publication: Charged particle multiplicities in pp interactions in the 100 MeV phase-space measured with the ATLAS detector*, Tech. Rep. ATL-COM-PHYS-2015-1379, CERN, Geneva, 2015. https://cds.cern.ch/record/2102358.

[59] ATLAS Collaboration, *Electron efficiency measurements with the ATLAS detector using the 2015 LHC proton-proton collision data*, Tech. Rep. ATLAS-CONF-2016-024, CERN, Geneva, Jun, 2016. https://cds.cern.ch/record/2157687.

[60] ATLAS Collaboration, *Electron and photon energy calibration with the ATLAS detector using data collected in 2015 at* $\sqrt{s} = 13$ TeV, Tech. Rep. ATL-PHYS-PUB-2016-015, CERN, Geneva, 2016. https://cds.cern.ch/record/2203514.

[61] ATLAS Collaboration, G. Aad et al., *Muon reconstruction performance of the ATLAS detector in proton-proton collision data at* $\sqrt{s} = 13$ *TeV*, European Physical Journal **C76** (2016) no. 5, 292, arXiv:1603.05598.

[62] ATLAS Collaboration, *Study of alignment-related systematic effects on the ATLAS Inner Detector tracking*, Tech. Rep. ATLAS-CONF-2012-141, CERN, Geneva, Oct, 2012. https://cds.cern.ch/record/1483518.

[63] GEANT4 Collaboration, S. Agostinelli et al., *GEANT4: A simulation toolkit*, Nuclear Instruments and Methods in Physics Research A **506** (2003) 250.

[64] T. Sjöstrand, S. Ask, J. R. Christiansen, R. Corke, N. Desai, P. Ilten, S. Mrenna, S. Prestel, C. O. Rasmussen, and P. Z. Skands, *An Introduction to PYTHIA 8.2*, Computer Physics Communications **191** (2015) 159, arXiv:1410.3012.

[65] *Electron efficiency measurements with the ATLAS detector using the 2012 LHC proton-proton collision data*, Tech. Rep. ATLAS-CONF-2014-032, CERN, Geneva, 2014. https://cds.cern.ch/record/1706245.

[66] *Expected performance of missing transverse momentum reconstruction for the ATLAS detector at $\sqrt{s} = 13$ TeV*, Tech. Rep. ATL-PHYS-PUB-2015-023, CERN, Geneva, 2015. https://cds.cern.ch/record/2037700.

[67] M. Cacciari, G. P. Salam, and G. Soyez, *The Anti-k(t) jet clustering algorithm*, Journal of High Energy Physics **04** (2008) 63, arXiv:0802.1189.

[68] W. Buttinger, *Using Event Weights to account for differences in Instantaneous Luminosity and Trigger Prescale in Monte Carlo and Data*, Tech. Rep. ATL-COM-SOFT-2015-119, CERN, Geneva, 2015. https://cds.cern.ch/record/2014726.

[69] J. Alwall, R. Frederix, S. Frixione, et al., *The automated computation of tree-level and next-to-leading order differential cross sections, and their matching to parton shower simulations*, Journal of High Energy Physics **07** (2014) 79, arXiv:1405.0301.

[70] ATLAS, *TTplusV*, Online, 2017. https://twiki.cern.ch/twiki/bin/viewauth/AtlasProtected/TTplusV#Uncertainties. [accessed 26-June-2017].

[71] C. Oleari, *The POWHEG-BOX*, Nuclear Physics - Proceedings Supplements **205-206** (2010) 36, arXiv:1007.3893.

[72] H.-L. Lai, J. Huston, Z. Li, P. Nadolsky, J. Pumplin, D. Stump, and C. P. Yuan, *Uncertainty induced by QCD coupling in the CTEQ global analysis of parton distributions*, Physics Review **D82** (2010) 54021, arXiv:1004.4624.

[73] G. Ciezarek, M. Franco Sevilla, B. Hamilton, R. Kowalewski, T. Kuhr, V. Lüth, and Y. Sato, *A Challenge to Lepton Universality in B Meson Decays*, Nature **546** (2017) 227–233, arXiv:1703.01766.

[74] ATLAS Collaboration Collaboration, *$ZZ \to \ell^+\ell^-\ell'^+\ell'^-$ cross-section measurements and aTGC search in 13 TeV pp collisions with the ATLAS detector*, Tech. Rep. ATLAS-CONF-2017-031, CERN, Geneva, 2017. https://cds.cern.ch/record/2263045.

[75] W. Verkerke and D. Kirkby, *RooFit User's Manual, v 2.91*, tech. rep., 2008. https://root.cern.ch/download/doc/RooFit_Users_Manual_2.91-33.pdf.

[76] *ROOT Mathematical Libraries: Minuit2 Minimization Package*, Online. `http://seal.web.cern.ch/seal/MathLibs/Minuit2/html/index.html`.

[77] B. A. Murtagh and M. A. Saunders, *Minos 5.5 User's Guide*, Tech. Rep. SOL 83-20R, Stanford Univ., CA, USA, 1983. `http://web.stanford.edu/group/SOL/guides/minos55.pdf`.

[78] d0 Collaboration, *Measurement of the WZ and ZZ production cross sections using leptonic final states in* 8.6 fb^{-1} *of $p\bar{p}$ collisions*, Physical Review D **85** (2012) 112005.

[79] CDF Collaboration, *Measurement of the ZZ production cross section using the full CDF II data set*, Physical Review D **89** (2014) 112001, `arXiv:1403.2300`.

[80] L. Linssen, A. Miyamoto, M. Stanitzki, and H. Weerts, *Physics and Detectors at CLIC: CLIC Conceptual Design Report*, ArXiv e-prints (2012) , `arXiv:1202.5940`.

[81] J. Ellis and T. You, *Sensitivities of Prospective Future e+e- Colliders to Decoupled New Physics*, JHEP **03** (2016) 089, `arXiv:1510.04561`.

[82] M. Mangano, *Physics at the FCC-hh, a 100 TeV pp collider*, `arXiv:1710.06353 [hep-ph]`.

[83] G. Cowan, K. Cranmer, E. Gross, and O. Vitells, *Asymptotic formulae for likelihood-based tests of new physics*, European Physical Journal **C71** (2011) 1554, `arXiv:1007.1727`.

[84] W. Buttinger, *Asymptotic Formula for a General Double-Bounded Custom-Sided Likelihood Based Test Statistic*, `arXiv:1302.2799`.

[85] J. D. Kalbfleisch and R. L. Prentice, *The Statistical Analysis of Failure Time Data (2nd Ed.)*, Journal of the American Statistical Association **98** (2003) 1084.